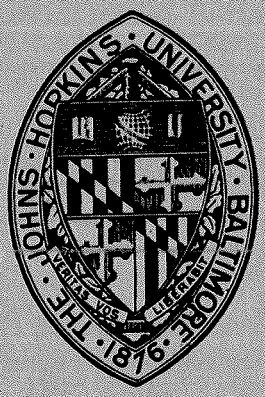

A Test of QED in Electron-Positron Annihilation at Energies around the Z Mass

Constantinos Evaggelos Spartiotis

Thesis submitted for the degree of Doctor of Philosophy
at The Johns Hopkins University

October 1992
Baltimore, Maryland

Abstract

A study of the reaction $e^+e^- \rightarrow \gamma\gamma(\gamma)$ at center-of-mass energies around the mass of the Z^0 boson(91.2GeV) has been performed. The total and differential cross sections have been measured corresponding to an integrated luminosity of $14.42pb^{-1}$. The results are in good agreement with QED predictions. Lower limits were set , at 95% confidence level, on the QED cutoff parameters of Λ_+ >130 GeV, Λ_- >112 GeV and on the mass of an excited electron of m_{e^*} >120 GeV. Z^0 rare decays with photonic signatures in the final state were also searched for. Upper limits, at 95% confidence level, for the branching ratio of Z^0 decaying into $\pi^0\gamma/\gamma\gamma$, $\eta\gamma$ and $\gamma\gamma\gamma$ are 1.2×10^{-4}, 1.7×10^{-4}, 3.3×10^{-5} respectively.

Thesis Advisor: Dr. Peter Fisher

Αφιερωμένο σε εσάς
που στηρίξατε το σώμα και την ψυχή μου
Με πολύ Αγάπη και Ευγνωμοσύνη
στην Μητέρα μου Ελισάβετ και τον Πατέρα μου Ευάγγελο

Also dedicated to Macedonia,
the glorious Northern province of Greece
which bears much of our national heritage and pride.

Preface

Working for five years towards a Ph.D was, more than anything else, an immense experience of life. I lived and worked in three different countries, I had the chance to meet and interact with people from three different continents and I have felt the excitement and pressure of doing research in the front line of physics. Maybe the most important value I learned these years is that progress and development is achieved best through cooperation and trust. I would like to thank Dr. Aihud Pevsner and Dr. Peter Fisher who made this 'intellectual trip' possible for me. Their leadership and guidance helped me throughout the three years of my research. Dr. S.C.C.Ting the spokesman of the $L3$ collaboration made this experiment a reality.

How can I thank Dr. Yannis Karyotakis with whom I worked closely on all aspects of the analysis for this thesis? For more than a year Yannis worked with me side by side day and night. More important than that he supported me and helped me out in difficult moments when everything just seemed impossible. He managed to build confidence inside me and he showed me what cooperation is really all about.

I had many interesting and enlightening discussions on parts of the physics analysis with Drs. R.T.Van de Walle, J.Ulbricht, A.Böhm, V.Andreev, M.Kienzle and J.Qian. Many thanks to Drs. C.Y.Chien, B.Blumenfeld, B.Barnett, L.Madansky. With all I had at different times interesting discussions which stimulated my work.

Within the TEC group I owe a lot to Drs. G.Viertel, J.Mnich, B.Betev, M.Pohl, G.Rahal-Callot. The first one year of my research I worked on the PSF system from which I acquired a lot of experience on both hardware and software. This project was the result of many people's effort which I would like to thank; J.Spangler, J.Orndorff, D.Newman and Drs. H.Akbari, A.Gougas, J.Bao, M.MacDermott, M.Glaubman, G.Alverson, I.Leedom, L.Taylor. I worked for about a year with L.Taylor on the PSF project; I appreciate his work, I learned a lot from him and

shared many good moments even though we disagree fundamentally on a small number of items. Among fellow students I would like to express my thanks to R.Rosmalen who worked with me on many occasions to resolve subtle problems, S.Rosier and A.Rubbia who really impressed me with his deep understanding of physics and willingness to find an answer to all of my questions.

Dr. Panos Razis is a special person to me. While he was at CERN he would always find time to help me with physics questions and problems. He gave me a lot of input when I was developing the alignment method for the PSF system. Together we spent many hours and he was one person I always felt I can count on and trust. He has been a true friend in happiness and sadness.

I must say that *L3* is a huge collaboration and every single person has contributed to this work one way or another. Many thanks to J.Swain and H.Lubbers for their support whenever there would be a problem in the computing system. I could not possibly forget the many administrative persons who with patience helped me in many cases. I would like to express my deep thanks to G.Kogler, L.Barrin, R.Decreuse, D.Labrousse,Y.Bernard, B.Staicer, N.Anderson and E.Hankin.

Finally I would like to point out here that every person has a different driving force in his life that keeps him going up the steep slope. You my dear parents, my dear sister, my dearest Rita, Aggelikh, Stelio, Louli, Erika, grand mother, Andronike, Eleutheria, Apostoli, Haralabe, Vaggeli have been my driving force. All the friends and relatives have been a lighthouse that showed me the way, kept my heart beating and my feelings alive.

Contents

List of Tables

List of Figures

Chapter 1

Theory

1.1 Introduction

Quantum ElectroDynamics is the theory of electromagnetic interactions and is the best theory in high energy physics. No deviation has been found in the predictions from QED even at small distances or equivalently at high energies. The Standard Model is the theory incorporating the electromagnetic and weak interactions. The first part of this chapter gives a brief introduction to QED and the Standard Model along the path of Lagrangian formalism. In the second half of this chapter we focus on the reaction $e^+e^- \to \gamma\gamma(\gamma)$, that was studied for this thesis using data from the Large Electron Positron collider at CERN, which to lowest order is a QED reaction. The predictions from QED are discussed as well as models that if verified would indicate a structure for the electron and the Z^0 boson. Finally we discuss the possibility of Z^0 decaying to $\pi^0\gamma$, $\eta\gamma$ and $\gamma\gamma$ with the above photonic signature in the final state.

1.2 QED and the Standard Model

1.2.1 Lagrangians and Classical Mechanics

In classical mechanics [1] the Lagrangian is defined to be the kinetic minus the potential energy: $L = T - V$. The Lagrangian is a function of the generalized coordinates q_i and its time derivatives $\dot{q}_i$. Action is defined as $I = \int_{t_1}^{t_2} L\,dt$ and Hamilton's variational principle states that a system develops from time t_1 to t_2 in

such a way so that the action is minimized. The Euler-Lagrange equations yield from this principle and they read for a classical system: $\frac{d}{dt}\left(\frac{\partial L}{\partial \dot{q}_i}\right) - \frac{\partial L}{\partial q_i} = 0$. The Euler-Lagrange equations along with initial and boundary conditions contain all the dynamics of a system in a simple and intuitive way. We can use Lagrangians to describe a discrete system(e.g. point masses connected together with springs), or for continuous systems(e.g. fluid motion). The Lagrangian formalism can incorporate fields $\phi(\chi^\mu)$ $(\mu = 1, 2, 3, 4)$ which vary continuously in space and time. The Lagrangian density(from now on referred to as Lagrangian) is a function of the field, its space-time derivatives and χ^μ; $\mathcal{L} = \mathcal{L}(\phi, \partial\phi/\partial\chi^\mu, \chi^\mu)$. Of importance is that the equations of motion should be invariant under a Lorentz transformation. This means that physics does not change when observation is made from different frames of reference that move at constant velocity with respect to each other. The Lorentz invariant form of the Euler-Lagrange equations is: $\frac{\partial}{\partial\chi^\mu}\left(\frac{\partial\mathcal{L}}{\partial(\partial\phi/\partial\chi_\mu)}\right) - \frac{\partial\mathcal{L}}{\partial\phi} = 0$. The generalized coordinates are substituted by the field ϕ. As an example consider a Lorentz scalar field ϕ with the following Lagrangian : $\mathcal{L} = \frac{1}{2}(\partial_\mu\phi)(\partial^\mu\phi) - \frac{1}{2}m^2\phi^2$. Substituting this Lagrangian into the Euler-Lagrange equation we arrive at the Klein-Gordon equation $(\partial_\mu\partial^\mu + m^2)\phi = 0$ which describes a free spinless particle of mass m.

1.2.2 Quantum ElectroDynamics

The Lagrangian which describes classical electromagnetism is:
$\mathcal{L}_{EM} = -\frac{1}{4}F_{\mu\nu}F^{\mu\nu} + j_\mu A^\mu/c$; A^μ is the electromagnetic potential with space component the vector magnetic potential $\vec{A}$ and time-like component the electrostatic potential V, $j_\mu = (\vec{j}, \rho)$ is the current density and $F_{\mu\nu} = \partial_\mu A_\nu - \partial_\nu A_\mu$ the electromagnetic field tensor. The Euler-Lagrange equations of motion yield $\partial^\nu F_{\mu\nu} = j_\mu$ and $\partial^\nu F_{\lambda\mu} + \partial^\lambda F_{\mu\nu} + \partial^\mu F_{\nu\lambda} = 0$ which is Maxwell's equations describing all of classical electromagnetism [3–5].

In classical electromagnetism gauge transformation we call a change in the potential scale. We distinguish between global and local gauge transformations. In a global transformation the potential changes by a constant amount everywhere. It is not the absolute value but the differences between potentials that matter and yield the electromagnetic reactions. Therefore there is a freedom in choosing the global potential scale and this we call global gauge invariance. A consequence of global gauge invariance is that charge is conserved [6](page 77). Electromagnetism has however the property of local gauge invariance as well: If we apply a gauge transformation on the magnetic vector potential such that $\vec{A} \xrightarrow{transforms} \vec{A}' =$

$\vec{A} + \vec{\nabla}\phi(\vec{x},t)$ and at the same time the electrostatic potential $V \xrightarrow{transforms} V' = V - \frac{\partial\phi(\vec{x},t)}{\partial t}$ then $\mathcal{L}_{EM} \xrightarrow{transforms} \mathcal{L}'_{EM}$. However substituting the new Lagrangian into the Euler-Lagrange equation leads to the same Maxwell equations as before. In other words the measurable physical quantities are the electric and magnetic fields and these remain unchanged from the above local gauge transformation. The local gauge transformation on the vector magnetic field is compensated by a similar local transformation on the static potential; there is a freedom in choosing one gauge or another for A_μ. The observation we make in this case is that we need both the vector magnetic and static electric fields to achieve local gauge freedom. Reversely local gauge freedom seems to suggest that magnetic and electric fields are interrelated and defines the dynamics of electromagnetism. To conclude on classical electromagnetism the global gauge invariance is intimately related to some conserved quantity, the electric charge and local gauge invariance introduces a single electromagnetic interaction.

Passing from classical electromagnetism to QED the Lagrangian of a fermion is $\mathcal{L}_{Dirac} = i\bar{\psi}\gamma^\mu\partial_\mu\psi - m\bar{\psi}\psi$ where ψ is the fermion's four component wave function and γ^μ the four Dirac matrices. This Lagrangian leads to the Dirac equation $(i\gamma^\mu\partial_\mu - m)\psi = 0$ describing a free spin 1/2 fermion. It is natural to wonder whether the physics results should depend on a phase transformation of the wave function $\psi \xrightarrow{transforms} \psi' = e^{iq(x^\mu)}\psi$. In an experiment we measure the amplitude, $|\psi|^2$, of the wave function or the phase difference between this and other wave functions(as for example in diffraction). Therefore one would expect that changing the phase in a wavefunction should not matter. Obviously a global phase transformation leaves the Dirac Lagrangian unchanged. The analog in classical electromagnetism is changing the global potential scale. To test the behaviour of the Dirac Lagrangian under a local phase transformation we substitute ψ' for ψ into the Dirac Lagrangian:

$$\begin{aligned}
\mathcal{L}_{Dirac} \xrightarrow{transforms} \mathcal{L}'_{Dirac} &= ie^{-iq}\bar{\psi}\gamma^\mu(e^{iq}\partial_\mu\psi + ie^{iq}\psi\partial_\mu q) - me^{-iq}\bar{\psi}e^{iq}\psi \\
&= i\bar{\psi}\gamma^\mu\partial_\mu\psi - i\bar{\psi}\gamma^\mu\psi\partial_\mu q - m\bar{\psi}\psi \\
&\neq \mathcal{L}_{Dirac}
\end{aligned}$$

Thus the Dirac Lagrangian is not gauge(phase) invariant. In an attempt to force local gauge invariance we transform the derivative ∂_μ into $D_\mu = \partial_\mu - ieA_\mu$, where we have introduced a new vector field A_μ. The choice of the new covariant derivative seems unjustifiable apriori but will become apparent if we redefine the Lagrangian

and then perform a gauge transformation:

$$\begin{aligned}\mathcal{L} &= i\bar{\psi}\gamma^\mu D_\mu\psi - m\bar{\psi}\psi \\ &= i\bar{\psi}\gamma^\mu(\partial_\mu - ieA_\mu)\psi - m\bar{\psi}\psi \\ &= i\bar{\psi}\gamma^\mu\partial_\mu\psi + e\bar{\psi}\gamma^\mu\psi A_\mu - m\bar{\psi}\psi\end{aligned}$$

We can see now that the resulting Lagrangian is gauge invariant by substituting $\psi' = e^{iq(x^\mu)}\psi$ for ψ and $A_\mu + \frac{1}{e}\partial_\mu q$ for A_μ.

$$\begin{aligned}\mathcal{L} \xrightarrow{transforms} \mathcal{L}' &= ie^{-iq}\bar{\psi}\gamma^\mu\partial_\mu(e^{iq}\psi) + e\bar{\psi}\gamma^\mu\psi(A_\mu + \frac{1}{e}\partial_\mu q) - me^{-iq}\bar{\psi}e^{iq}\psi \\ &= -\bar{\psi}\gamma^\mu\psi\partial_\mu q + i\bar{\psi}\gamma^\mu\partial_\mu\psi + e\bar{\psi}\gamma^\mu\psi A_\mu + \bar{\psi}\gamma^\mu\psi\partial_\mu q - m\bar{\psi}\psi \\ &= i\bar{\psi}\gamma^\mu\partial_\mu\psi + e\bar{\psi}\gamma^\mu\psi A_\mu - m\bar{\psi}\psi \\ &= \mathcal{L}\end{aligned}$$

The phase change on the particle's wavefunction is compensated by a gauge change on the vector field A_μ. It is an analog of the classical electromagnetic case were a gauge change on the the electrostatic potential is compensated by a gauge change on the vector potential.

The new Lagrangian is different from the Dirac one in that it includes a new vector field A_μ which is the photon field. In classical electromagnetism we saw how the gauge freedom suggested a unified electromagnetic theory and now the demand of locally gauge(phase) invariant Lagrangian lead us to reveal the interaction of charged fermions with the photon field. To complete the new Lagrangian we add an extra term corresponding to the photonic kinetic energy $-\frac{1}{4}F_{\mu\nu}F^{\mu\nu}$ which is also gauge invariant. A photon mass term like $m^2A_\mu A^\mu$ cannot be considered because it is not gauge invariant; the photon is massless. The final Lagrangian which describes QED is:

$$\boxed{\mathcal{L}_{QED} = \bar{\psi}(i\gamma^\mu\partial_\mu - m)\psi + e\bar{\psi}\gamma^\mu A_\mu\psi - \frac{1}{4}F_{\mu\nu}F^{\mu\nu}} \tag{1.1}$$

Local gauge invariance has determined the form of the final Lagrangian and the dynamics of QED. The group of all such gauge transformations is the $U(1)$ group.

The significance of gauge invariance goes even deeper. In principle once the Lagrangian is known one can derive the Euler-Lagrange equations and solve them, but in practice even the simplest QED cases cannot be solved exactly and perturbation theory is used to approach the exact solution. It is of course desired that higher orders in the perturbation expansion should converge to a finite result. It

has been shown that QED is such a theory. The divergencies that appear when higher orders are included can be absorbed in a redefinition of physical quantities such as the charge and the mass of the electron, keeping the expansion finite at any order. Such a theory is said to be renormalizable and t'Hooft showed in 1971 that any theory that does not respect local gauge invariance cannot be renormalizable. Finally the perturbative expansion in QED is done in orders of $\alpha = \frac{e^2}{4\pi} \approx \frac{1}{137}$ which defines the coupling strength. Since $\alpha \ll 1$ higher order corrections are monotonically decreasing and the whole expansion is at any order finite and converges to a steady unique solution.

1.2.3 The Standard Model

Starting from the observation that leptons couple to each other in pairs (e.g. $\nu_e \longleftrightarrow e$, $\nu_\mu \longleftrightarrow \mu$ etc) the weak isospin group $SU(2)$ is defined. In this group all left handed doublets have a principal quantum number $t = \frac{1}{2}$ with third component $t_3 = \frac{1}{2}$ for ν_e, ν_μ, ν_τ,...u, c,... and $t_3 = -\frac{1}{2}$ for e^-, μ^-, τ^-,...d, s,.... All right handed massive fermions have $t = t_3 = 0$. In quantum mechanics a group of transformations that leave invariant the Hamiltonian results in multiplets of quantum states degenerate in energy with different quantum numbers of the conserved quantity. For example a rotationally invariant Hamiltonian has energy eigenstates with the same energy eigenvalue for every angular momentum value regardless of the third component of the angular momentum. In the case of the weak isospin group, the doublets are not composed from mass degenerate particles, indicating a hidden rather than an explicit symmetry. In an effort to create a group theory that could describe all QED and weak phenomena Glashow proposed an enlargement of the weak isospin group to $SU(2)_L \times U(1)_Y$. The new $U(1)_Y$ group defines a "hypercharge" of all leptons that belong to the same weak isospin group. The charges of the leptons and the quarks(in units of electron charge) are given from the relation: $Q = t_3 + \frac{y}{2}$. Associated to to the $SU(2)_L$ group of weak isospin transformations are three vector boson fields $\vec{W}^\mu$. Two of them are charged and one is neutral. Similarly associated to the $U(1)_Y$ hypercharge group is a neutral vector boson field B^μ. In QED, described by the $U(1)$ group of space-time phase transformations, local gauge invariance is accomplished with the transformation of ∂^μ to $\partial^\mu - ieA^\mu$ when ψ goes through a phase transformation(section 1.2.2). To be precise a phase transformation of the wave function in the $U(1)_{em}$ group is defined as $\psi \longrightarrow e^{iq(\chi^\mu)Q}\psi$, where Q is the charge operator necessary to keep track of the particle's charge. For the electron $Q = -1$ and this was omitted. In

the electroweak model, described by the $SU(2)_L \times U(1)_Y$ group, we can imagine a phase transformation in the isospin×hypercharge space. For example:

$$\begin{pmatrix} \nu_e \\ e^- \end{pmatrix}_L \xrightarrow{transforms} \begin{pmatrix} \nu_e \\ e^- \end{pmatrix}_L' = e^{\left(i\vec{\alpha}(\chi^\mu)\vec{\tau} + i\beta(\chi^\mu)Y\right)} \begin{pmatrix} \nu_e \\ e^- \end{pmatrix}_L$$

were $\vec{\tau}$, Y are the operators of weak isospin and hypercharge. A phase transformation of a right handed fermion($t = t_3 = 0$) would only involve the hypercharge of that fermion: $\psi_r \longrightarrow e^{\left(i\beta(\chi^\mu)Y\right)}\psi_r$. The recipe to recover gauge invariance is the same as in QED, that is to transform the derivative ∂^μ accordingly:

When

$$\begin{pmatrix} \nu_e \\ e^- \end{pmatrix}_L \xrightarrow{transforms} \begin{pmatrix} \nu_e \\ e^- \end{pmatrix}_L' = e^{\left(i\vec{\alpha}(\chi^\mu)\vec{\tau} + i\beta(\chi^\mu)Y\right)} \begin{pmatrix} \nu_e \\ e^- \end{pmatrix}_L$$

then

$$\partial^\mu \xrightarrow{transforms} D^\mu = \partial^\mu + ig\,\vec{t}\cdot\vec{W}^\mu + i(g'/2)yB^\mu$$

The constants g and g' are fundamental and they correspond to "weak charges" in analogy with the electron charge e in QED. The electroweak Lagrangian that yields is gauge invariant, but apart from describing massless vector bosons has also the problem that fermions as well are forbidden to have mass. This is because in the new $SU(2)_L \times U(1)_Y$ gauge a term like $m_e\bar{\psi}_e\psi_e$ would not be gauge invariant as can be seen if ψ_e, $\bar{\psi}_e$ are decomposed to their left and right hand components. For example $\bar{\psi}_e^R\psi_e^L \xrightarrow{transforms} e^{\left(i\vec{\alpha}(\chi^\mu)\vec{\tau}+i\beta(\chi^\mu)(Y^L-Y^R)\right)}\bar{\psi}_e^R\psi_e^L$. Through the Higgs mechanism vector bosons as well as fermions 'acquire' mass spontaneously breaking the gauge symmetry but without destroying renormalizability.

The vector fields $\vec{W}^\mu \equiv (W_1^\mu, W_2^\mu, W_3^\mu)$ and B^μ are not directly physical but a combination of those yields the four physical vector fields of the electroweak theory. In particular if we introduce the Glashow-Weinberg angle $\theta_w = \frac{g'}{g}$ then the physical fields A^μ(massless electromagnetic) and $Z^0, W^\pm$(massive weak) are given from the following relations.

$$\begin{aligned} A^\mu &= \sin\theta_w W_3^\mu + \cos\theta_w B^\mu \\ Z^0 &= \cos\theta_w W_3^\mu - \sin\theta_w B^\mu \\ W^+ &= \sqrt{\tfrac{1}{2}}\,(W_1^\mu - iW_2^\mu) \\ W^- &= \sqrt{\tfrac{1}{2}}\,(W_1^\mu + iW_2^\mu) \end{aligned}$$

The above group theory of electroweak interactions was developed by Glashow, Weinberg and Salam and is the Standard Model [2–4]. The Z^0 and $W^{\pm}$ vector bosons were first seen from the $UA1$ collaboration at CERN. So far all predictions from the Standard model have been verified by experiment and this group theory is the best we have so far that unifies QED and weak interactions.

1.3 The QED reaction $e^+e^- \to \gamma\gamma(\gamma)$

The first section overviewed QED and the Standard Model along the path of Lagrangian formalism and group theory. In this and the next section I discuss more specifically the physics that my research focused on. In particular the production in the final state of photons coming from $e^+e^- \to \gamma\gamma(\gamma)$.

The reaction $e^+e^- \to \gamma\gamma$ is a pure QED one to lowest order. There are two

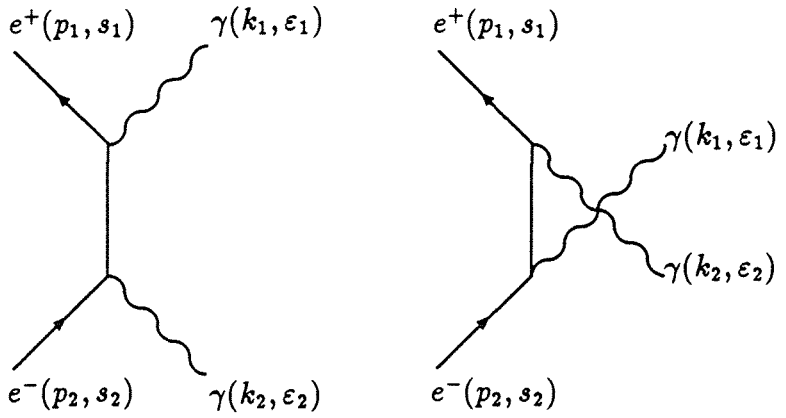

Figure 1.1: The lowest order diagrams for the reaction $e^+e^- \to \gamma\gamma$

lowest order Feynman diagrams which are shown in Figure 1.1 The first diagram is the t channel and the second is the u channel that must be included because we cannot distinguish between the photons in the final state. The reaction goes through the exchange of a virtual electron; thus there are no weak interference effects. The lowest order differential cross section is:

$$\boxed{\frac{d\sigma}{d\Omega} = \frac{\alpha^2}{s}\frac{1+\cos^2\theta}{\sin^2\theta}} \tag{1.2}$$

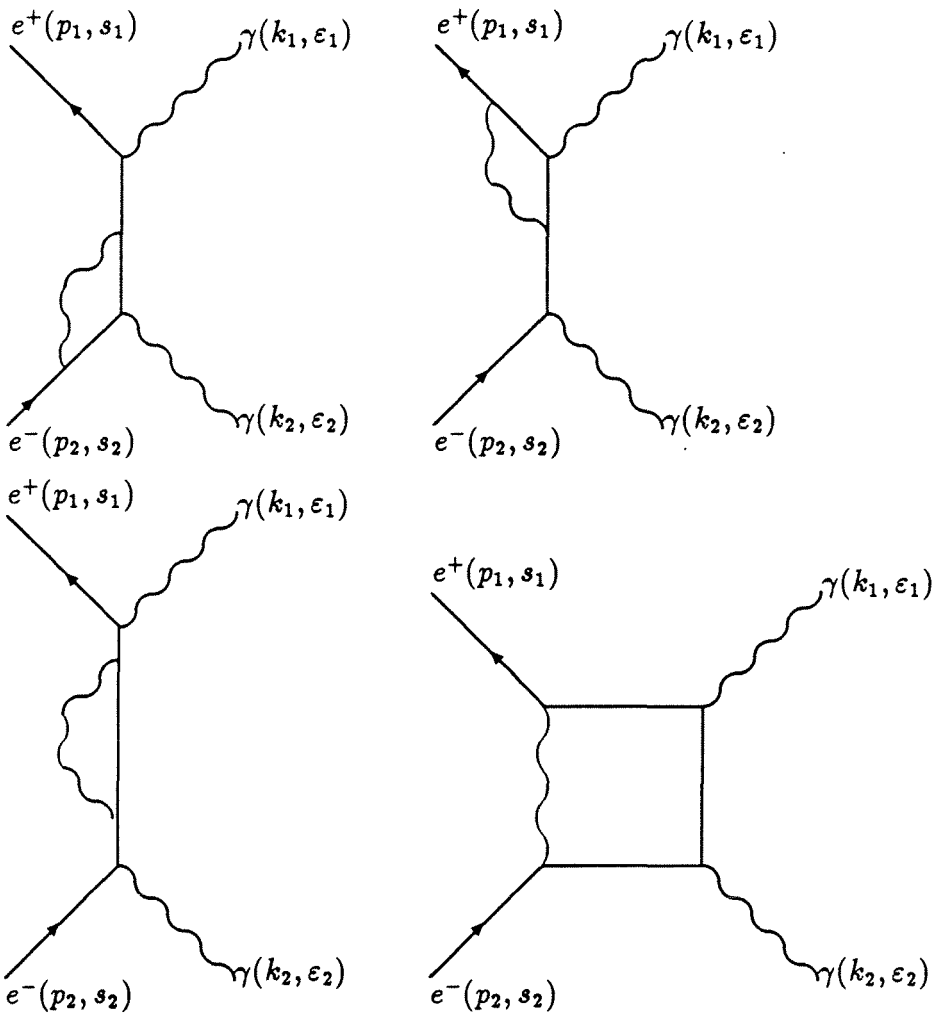

Figure 1.2: Half of the diagrams for the virtual corrections contributing to $O(\alpha^3)$ in the cross-section of the reaction $e^+e^- \to \gamma\gamma$. The other half are obtained by interchanging $\gamma(k_1, \varepsilon_1)$ with $\gamma(k_2, \varepsilon_2)$.

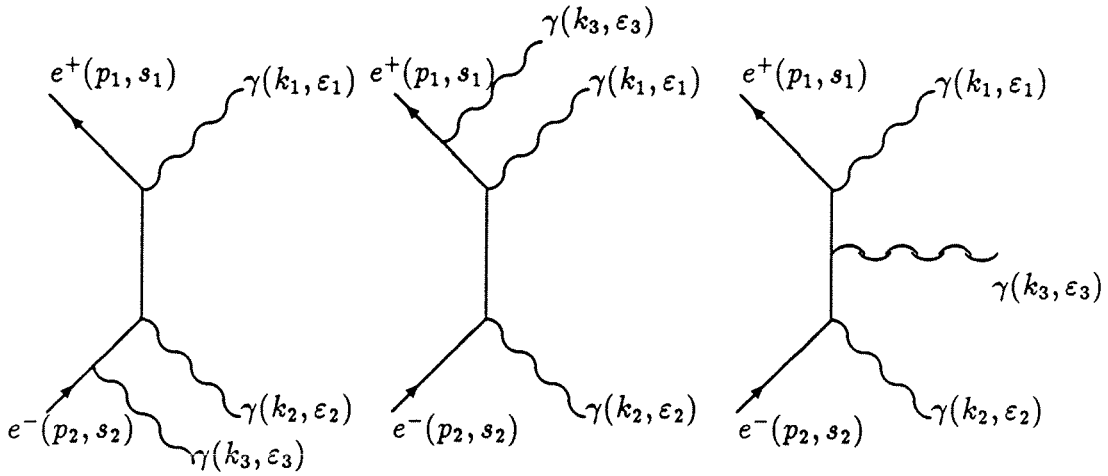

Figure 1.3: Half of the diagrams contributing to $O(\alpha^3)$ in the cross-section of the reaction $e^+e^- \to \gamma\gamma\gamma$. The other half are obtained by interchanging $\gamma(k_1,\varepsilon_1)$ with $\gamma(k_2,\varepsilon_2)$.

were $\alpha = e^2/4\pi$, s is the beam energy and θ is the angle of one of the photons with the beam direction. We see that the cross-section is symmetric in θ around $|\cos\theta| = 0$ and is peaked forward-backward(it actually diverges at $|\cos\theta| = 1$). In appendix A the calculation of the lowest order matrix element is done in detail. The next higher order diagrams leading to $O(\alpha^3)$ include virtual corrections as well as soft and hard bremsstrahlung radiation [7]. By virtual we mean the vertex corrections, electron propagator corrections and the box diagram correction. The bremsstrahlung corrections are responsible for a third photon that comes from one of the external electron lines or from the virtual electron. The third photon may have arbitrarily small energy and the distinction between a two and a three photon event is based on the detector's energy and spatial resolution. In fact unless a low energy cut is applied on the bremsstrahlung radiation then the cross section is lead to infrared divergencies [7,8]. For this thesis the low energy cut was taken to be 1% of the beam energy. This will be discussed again in Chapter 3 where the simulation program for QED is described. Virtual and bremsstrahlung corrections(from now on called radiative corrections) become important at energies around the Z^0 pole. Figure 1.2 shows the higher order diagrams up to $O(\alpha^3)$ that contribute to the reaction $e^+e^- \to \gamma\gamma$. These are the virtual corrections. Figure 1.3 shows the diagrams to $O(\alpha^3)$ that are responsible for the reaction $e^+e^- \to \gamma\gamma\gamma$. Topologically all three diagrams in Figure 1.3 are the same but the distinction is made because the third photon is usually soft and may be initial state radiation coming from the

electron or the positron or may be coming from the virtual electron. Figure 3.2 shows the energy and angular distribution of the third photon.

1.4 Beyond the Standard Model

Search for underlying structure has always been at the frontier of physics. Different ways to reveal compositeness and underlying structure include the search of excited states, non pointlike structure or observation of the decay products of the composite object. All of the above are different views of the same aspect. If one would imagine that quarks, leptons and gauge bosons are composite objects many questions could be answered, such as the family problem, the unnaturalness of the Higgs mechanism, and why there are arbitrary parameters that have to be determined by experiment like the QED coupling constant, or the Weinberg angle. New physics would also be signalled if rare or forbidden decay modes of Z^0 would be observed. Some theories predict enhanced decay rate of the Z^0 boson to the η or π meson.

1.4.1 Excited Electron

In section 1.3 the $O(\alpha^3)$ diagrams for the reaction $e^+e^- \rightarrow \gamma\gamma$ and $e^+e^- \rightarrow \gamma\gamma\gamma$ were given. If an excited electron exists we must add to these diagrams those where the virtual electron is replaced by a virtual excited electron [9]. The standard QED Lagrangian was given in section 1.2.2. An extra term must be added to describe the coupling of the excited electron(e^*) to an electron and a photon. In the standard QED Lagrangian the interaction of an electron with a photon is described by the term $e\bar{\psi}\gamma^\mu A_\mu \psi$. This term on its own is not gauge invariant but the electron's kinetic energy term $\bar{\psi}(i\gamma^\mu\partial_\mu - m)\psi$ restores gauge invariance. This Lagrangian must be completed to take into account the interaction of a virtual excited electron with an electron and the photon field. Litke in his thesis [9] introduced a magnetic interaction term $\frac{e\lambda}{2m_{e^*}}\bar{\psi}_{e^*}\sigma_{\mu\nu}\psi_e F^{\mu\nu}$. This interaction is gauge invariant since the electromagnetic field tensor $F^{\mu\nu}$ is by itself gauge invariant and $\bar{\psi}'_{e^*}\sigma_{\mu\nu}\psi'_e = \bar{\psi}_{e^*}\sigma_{\mu\nu}\psi_e$ $(\psi'_e = e^{ieq(x)}\psi_e)$. The dimensionless constant λ gives the relative strength of the coupling with respect to the QED magnetic coupling(which is proportional to $e/2m_e$). If this reaction exists it would be a clear indication of a QED breakdown, since in our present understanding the electron is a point-like object with no structure and therefore it cannot exist in an excited state [9–11].

One may wonder why a new interaction is introduced by hand and we cannot simply consider a coupling of the virtual excited electron with the electron and the photon field as in the standard QED case, i.e a term like $e\bar{\psi}_{e^*}\gamma^\mu A_\mu \psi_e$. The reason why such a term is not allowed is because it is not gauge invariant and since we are coupling an excited electron to an electron a kinetic energy term like $\bar{\psi}_{e^*}(i\gamma^\mu\partial_\mu - m)\psi_e$, which would restore gauge invariance, does not exist. Therefore a new coupling had to be introduced by hand and was added to the QED Lagrangian given in equation 1.1.

The effect of such a breakdown caused by an excited electron has been parameterized in the differential cross section at lowest(Born) order (i.e. including the $O(\alpha)$ QED and non QED diagrams) [9–11]. $(d\sigma/d\Omega)^0_T$, can be written as:

$$(1.3) \qquad (d\sigma/d\Omega)^0_T \equiv \sigma(\theta)^0_T = \sigma(\theta)^0_{QED}\ (1 \pm \delta_{new})$$

where $\delta_{new} = s^2/2\ \left(1/\Lambda^4_\pm\right)\ (1-\cos^2\theta)$, θ is the angle of the emitted photons with respect to the beam axis, $\sqrt{s}$ the center-of-mass energy and $\Lambda_\pm$ are the QED cut-off parameters. The Λ_+ parameter does not represent the excited electron's mass, but rather a mass divided by the coupling strength, λ. That is $\Lambda^2_+ = m^2_{e^*}/\lambda$. The differential cross-section would only increase if an excited electron exists, but a negative contribution Λ_- has been added for symmetry purposes. This parameter is therefore introduced by the experimentalist to account for something that could decrease the cross-section.

In terms of the mass of the excited electron the differential cross-section becomes [9]:

$$(1.4) \quad (d\sigma/d\Omega)^0_T \equiv \sigma(\theta)^0_T = \sigma(\theta)^0_{QED}\left(1 + \frac{s^2}{2}\left(\frac{\lambda^2}{m^4_{e^*}}\right)\left(1-\cos^2\theta\right)F(\cos\theta)\right)$$

with :

$$F(\cos\theta) = \left(1 + \frac{s}{2m^2_{e^*}}\frac{1-\cos^2\theta}{1+\cos^2\theta}\right)\left(\left(1+\frac{s}{2m^2_{e^*}}\right)^2 - \left(\frac{s}{2m^2_{e^*}}\right)^2\cos^2\theta\right)^{-1}$$

The nice feature of equations 1.3 and 1.4 is that the QED contribution at lowest order has been factored out. Certainly though at energies around the Z^0 mass we cannot neglect corrections to the QED lowest order cross-section arising from diagrams 1.2 and 1.3. On the other hand radiative corrections on the diagrams involving the excited electron have not yet been calculated. We should examine therefore what happens to equations 1.3 and 1.4 if higher order QED diagrams are included. To $O(\alpha^3)$ the QED diagrams responsible for the interaction $e^+e^- \to \gamma\gamma$

are shown in Figures 1.1 and 1.2. To the same order we must add the diagrams in Figure 1.3 responsible for the interaction $e^+e^- \to \gamma\gamma\gamma$ where the third photon is usually soft and very close to one of the primary photons. The complication now arises from the fact that equations 1.3 and 1.4 were derived only taking into account the lowest order diagrams for both the QED and the excited electron part. But if we combine the standard QED diagrams with radiative corrections and the non-radiatively corrected excited electron diagrams we are lead to an infrared divergent cross-section. This can be shown considering the different amplitudes that contribute to the cross-section [12]. We define the amplitude corresponding to diagrams 1.1 as $T_e^{(1)}$. The subscript indicates that a pointlike electron is the propagator and the superscript shows that this amplitude is $O(\alpha)$. For all $O(\alpha^2)$ diagrams(Figure 1.2) the corresponding amplitude is $T_e^{(2)}$. Diagrams 1.3 responsible for bremsstrahlung radiation are $O(\alpha^{3/2})$ and the corresponding amplitude is $T_e^{(\gamma)}$. In this case the superscript indicates that a real third photon is emitted. In deriving the cross-section the first two amplitudes must be added together and then squared and separately the amplitude $T_e^{(\gamma)}$ is squared and added. This is because when a third photon is emitted we have different phase space and the process is distinguishable from the two photon case. The cross-section will then be:

$$\begin{aligned} \left(\frac{d\sigma}{d\Omega}\right)_{QED} &\sim \overbrace{\left|T_e^{(1)} + T_e^{(2)}\right|^2}^{e^+e^- \to \gamma\gamma} + \overbrace{\left|T_e^{(\gamma)}\right|^2}^{e^+e^- \to \gamma\gamma\gamma} \\ &= \underbrace{\left|T_e^{(1)}\right|^2}_{O(\alpha^2)} + \underbrace{\left|T_e^{(2)}\right|^2}_{O(\alpha^4)} + \underbrace{\left|T_e^{(\gamma)}\right|^2}_{O(\alpha^3)} + \underbrace{2\ Re\left(T_e^{(1)*} T_e^{(2)}\right)}_{O(\alpha^3)} \end{aligned} \tag{1.5}$$

The $O(\alpha^3)$ differential cross-section is derived if we drop from the above expression the term $\left|T_e^{(2)}\right|^2$ which is $O(\alpha^4)$. The terms $\left|T_e^{(\gamma)}\right|^2$ and $2\ Re\left(T_e^{(1)*} T_e^{(2)}\right)$ are individually infrared divergent but their sum is finite, keeping the differential cross-section finite as well. If now the $O\left(\alpha(\lambda/m_{e^*})^2\right)$ amplitude,$T_{e^*}^{(1)}$, involving a virtual excited

electron is included then the cross-section becomes:

$$\left(\frac{d\sigma}{d\Omega}\right)_{Total} \sim \overbrace{\left|T_e^{(1)} + T_e^{(2)} + T_{e^*}^{(1)}\right|^2}^{e^+e^-\to\gamma\gamma} + \overbrace{\left|T_e^{(\gamma)}\right|^2}^{e^+e^-\to\gamma\gamma\gamma}$$

$$= \underbrace{\left|T_e^{(1)}\right|^2}_{O(\alpha^2)} + \underbrace{\left|T_e^{(\gamma)}\right|^2}_{O(\alpha^3)} + \underbrace{2\ Re\left(T_e^{(1)*}T_e^{(2)}\right)}_{O(\alpha^3)} + \tag{1.6}$$

$$\underbrace{\left|T_{e^*}^{(1)}\right|^2}_{O(\alpha^2(\lambda/m_{e^*})^4)} + \underbrace{2\ Re\left(T_e^{(1)*}T_{e^*}^{(1)}\right)}_{O(\alpha^2(\lambda/m_{e^*})^2)} + \tag{1.7}$$

$$\underbrace{2\ Re\left(T_e^{(2)*}T_{e^*}^{(1)}\right)}_{O(\alpha^3(\lambda/m_{e^*})^2)} + \tag{1.8}$$

$$\underbrace{\left|T_e^{(2)}\right|^2}_{O(\alpha^4)} \tag{1.9}$$

We find the following groups of terms above: In 1.6 terms up to $O(\alpha^3)$ have been included determining the QED differential cross-section. The terms in 1.7 are the $O\left(\alpha^2(\lambda/m_{e^*})^2\right)$ and $O\left(\alpha^2(\lambda/m_{e^*})^4\right)$ contributions from the excited electron and are finite. Finally to $O\left(\alpha^3(\lambda/m_{e^*})^2\right)$ there is the term 1.8 which however is infrared divergent. To this order there is no other term,like in the QED case, to make the cross-section finite. This is a consequence of the fact that radiative corrections for the excited electron have not been included. If such corrections are calculated the final result may be finite but this remains to be seen in the future.

With the above arguments it is shown what is the cause for the divergence of the cross-section. In practise if we wish to proceed with the search of a virtual excited electron we must make an approximation as to what the total $O(\alpha^3)$ cross-section would be if the radiative corrections for the excited electron were carried out. Moreover we wish to maintain the functional form of equations 1.3 and 1.4. There are two approaches to approximate the infrared divergent differential cross section with a finite measurable one. In both approaches the end result is a cross-section that includes contributions from: $e^+e^- \to \gamma\gamma$(QED to $O(\alpha^3)$), $e^+e^- \to \gamma\gamma\gamma$(QED to $O(\alpha^3)$) and $e^+e^- \to \gamma\gamma$(excited electron to lowest order). The measured cross section compared to the theoretical one calculated to $O(\alpha^3)$ is:

$$\sigma(\theta)_{Measured} = \sigma(\theta)_{QED}^{O(\alpha^3)}\ (1 + \rho)$$

where ρ is the excess coming from non-QED effects.

$$\rho = \left(\sigma(\theta)_T^{O(\alpha^3)} - \sigma(\theta)_{QED}^{O(\alpha^3)}\right) \Big/ \sigma(\theta)_{QED}^{O(\alpha^3)}$$

In the first approach we approximate ρ by the following expression:

$$\rho \approx \left(\sigma(\theta)^0_T - \sigma(\theta)^0_{QED}\right) / \sigma(\theta)^{O(\alpha^3)}_{QED}$$

Then the measured cross section becomes:

$$\sigma(\theta)_{Measured} = \sigma(\theta)_{QED\ Corr\ O(\alpha^3)} + \sigma(\theta)^0_{QED}\,(1 + \delta_{new})$$

The term δ_{new} is the Born level contribution from the coupling of an excited electron to the electron and photon as given in equation 1.3. Next the QED corrections $O(\alpha^3)$ are subtracted from the data at the left hand side of the equation. In this first approach the data are modified to be compared with the zeroth order total differential cross section. This approximation was used in recent publications [13], [14], [15].

In a second approach the infrared divergent differential cross section is approximated by a finite measurable one, replacing ρ by its Born level expression:

$$\rho \approx \left(\sigma(\theta)^0_T - \sigma(\theta)^0_{QED}\right) / \sigma(\theta)^0_{QED} = \delta_{new}$$

Then the measured cross section is compared to:

$$(1.10)\quad \sigma(\theta)_{Measured} = \sigma(\theta)^{O(\alpha^3)}_{QED}\left(1 + \frac{\sigma(\theta)_{New\ Born}}{\sigma(\theta)^0_{QED}}\right) = \sigma(\theta)^{O(\alpha^3)}_{QED}(1 + \delta_{new})$$

where $\sigma(\theta)_{New\ Born} = \sigma(\theta)^0_{QED} \times \delta_{new}$ with δ_{new} as defined in equation 1.3. In this approach the data are directly compared to the theory. For this analysis the second approach was chosen because it appealed to us philosophically the fact that no information is being subtracted from the data. We compare what comes out from the detector with some model. Nevertheless it should be pointed out that both approaches are approximations whose validity is to be seen in the future when radiative corrections for the excited electron have been calculated.

The excited electron can be searched also directly when it is pair produced. In this case the signature is two pairs of electrons and photons with electron-photon invariant mass spectrum peaked at the mass of the excited electron. A standard coupling can be used for the $e^*e^*Z^0$ or $e^*e^*\gamma$ vertex because the excited electrons are doubly produced now. This method is limited on the mass range by kinematics so we would not see the excited electrons if their mass is more than the beam energy. On the other hand the signature of a pair of electrons with associated photons and a peaked invariant mass spectrum is more spectacular [16–18]. The background would be from doubly radiative Bhabha events.

1.4.2 Z^0 Compositeness and Rare Decays

In the Standard Model Z^0 could decay into three photons only via a one loop diagram involving fermions, quarks or the $W^{\pm}$ gauge bosons [19]. The branching ratio of this decay is about 7×10^{-10} [19]. If however the Z^0 is a composite object then it could couple to photons through its charged constituent parts with a branching ratio as high as 10^{-4} [20, 21]. The most significant background is the QED reaction $e^+e^- \rightarrow \gamma\gamma\gamma$ with the third photon radiated from one of the external electron lines or the virtual electron as discussed in section 1.3 and shown in Figure 1.3. However the signature is significantly different because the QED events are strongly peaked forward-backwards, the third photon is colinear to one of the primary photons and it has low energy(typically less than 1 GeV). Figure 3.2 shows the distribution of the energy and polar angle of the least energetic photon for QED Monte Carlo three photon events. On the other hand the photons coming from a Z^0 decay are expected to have the following average energies [21]: $< E_3 >= 20\text{GeV}$, $< E_2 >= 31\text{GeV}$, $< E_1 >= 40\text{GeV}$. The angles between them are expected to be: $< \theta_{23} >= 80°$, $< \theta_{13} >= 130°$ and $< \theta_{12} >= 150°$. The biggest difference appears in the energy of the least energetic photon. The QED cross-section drops as the center of mass energy increases and is independent from the mass of Z^0 boson. As explained in reference [21] the anomalous coupling is by far largest on the Z^0 peak and this is where we expect to see a number of isolated and 'hard' three photon events in excess of the QED background. In fact its effect above and below the Z^0 peak is completely negligible which means that there is almost no interference between QED and the new coupling. At exactly the Z^0 pole the QED amplitude is real and the Z^0-exchange is imaginary.

Another interesting process is a possible decay of Z^0 to two photons. Yang showed that a vector particle cannot decay into two photons on grounds of angular momentum and parity conservation [22]. In particular for the Z^0 vector boson we can decompose its possible eigenstates as an orthonormal combination of the photon final states using the Glebsh-Gordon coefficients:

$$
\begin{array}{cccccccc}
S_{Z^0} & S^3_{Z^0} & & & S^3_{\gamma 1} & S^3_{\gamma 2} & & S^3_{\gamma 1} \; S^3_{\gamma 2} \\
|1, & 0> & = \sqrt{\tfrac{1}{2}} & |1, & -1> & - & \sqrt{\tfrac{1}{2}}| & -1, \; 1> \\
|1, & 1> & = \sqrt{\tfrac{1}{2}} & |1, & 0> & - & \sqrt{\tfrac{1}{2}}| & 0, \; 1> \\
|1, & -1> & = \sqrt{\tfrac{1}{2}} & |0, & -1> & - & \sqrt{\tfrac{1}{2}}| & -1, \; 0>
\end{array}
$$

We note now that the Z^0 coming from e^+e^- collision cannot have $S^3_{Z^0} = 0$. This is because at high energies vertices with the electron and positron having antiparallel spins are suppressed by a factor of m_e/E_{beam}. In other words the cross-section

from such a configuration is suppressed by $(m_e/E_{beam})^2 \approx 10^{-10}$. This is proved in reference [3](page 126). As a consequence the first Z^0 state listed above is not possible. The remaining two Z^0 states are possible but real photons cannot have spin zero and the decomposition to two photons is therefore not allowed. Such a forbidden decay of Z^0 would be difficult to separate from the $e^+e^- \rightarrow \gamma\gamma$ background. A production though of highly colinear two photon events in excess of the QED prediction would signal new physics. Finally rare decays(but not forbidden) of Z^0 with photonic signature in the final state can also be looked for to test the predictions of various models for the coupling of Z^0 to $\pi^0\gamma$ and $\eta\gamma$ [23–25]. The $\pi^0\gamma$ and $\eta\gamma$ angular distribution is $1 + \cos^2\theta$. The π^0 meson decays to 2γ with 98.8% branching ratio. These photons coming from the π^0 are boosted and in the lab frame are extremely colinear. The η meson decays into 2γ, $3\pi^0$ with 38.9% and 31.9% branching ratio respectively. Again the final state neutral particles coming from η are highly boosted and appear extremely colinear in the lab frame. Its charged decay modes to $\pi^+\pi\_\pi^0$ and $\pi^+\pi\_\gamma$ account for 28.4% of the total decays.

Chapter 2

The Detector.

2.1 The LEP Collider

The Large Electron Positron(LEP) collider is currently the world's biggest colliding beam machine. LEP is 27km in circumference and at 1988 prices the cost of LEP was about 1130 million Swiss francs. The tunnel is 3.8m wide situated at between 50m and 170m below the surface. It passes two thirds in French and one third in Swiss territory. Access shafts at eight points on the ring link the tunnel to surface installations. Four large underground halls, 23m in diameter and 70m long, house the huge detectors. The LEP ring consists of eight 2800m long curved sections linked by eight straight sections. In the curved sections the particles are kept in course by 3392 bending magnets, while particle focusing is achieved by 816 quadrupole and 504 hexapole magnets. Radiofrequency cavities accelerate the beams of electrons and positrons. In total there are four bunches of electrons and four bunches of positrons circulating in opposite directions which collide at the four predefined points were the detectors are located. Figure 2.1 shows schematically the location of the LEP ring.

2.2 The L3 Detector

2.2.1 The Magnet

The various detectors composing L3 [26] are mounted inside a conventional magnet comprising an Aluminum solenoid coil and an iron yoke which surrounds the coil.

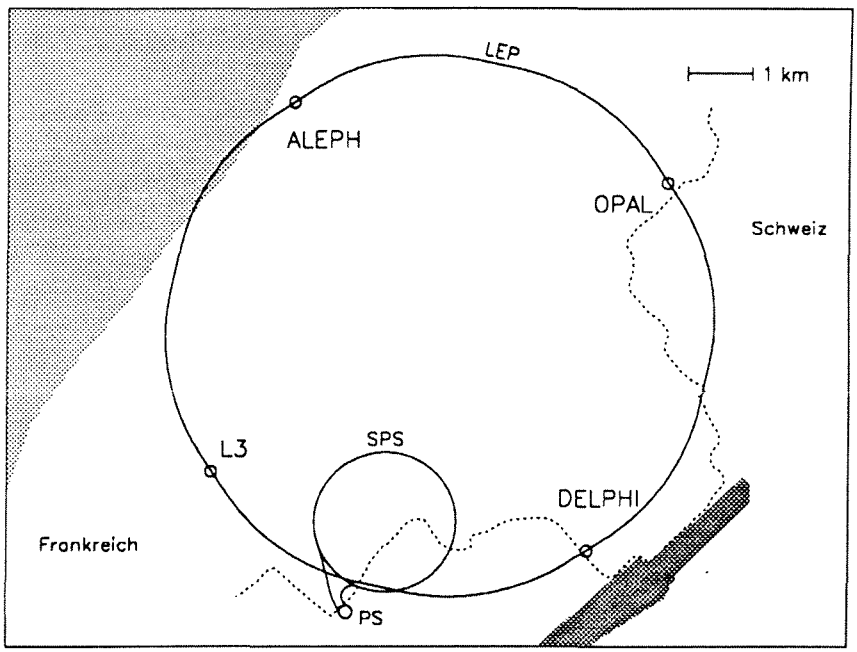

Figure 2.1: The LEP ring.

The inside radius of the 1100t coil is 5.93m, the outside radius of the 6700t yoke is 7.9m and the total length of the magnet is 11.9m. In nominal operation the rated current is 30kA and inside the magnet the uniform field value is 0.5T The magnet with various subdetectors mounted is shown schematically in Figure 2.2. A photo of the Aluminum solenoid coil is shown in Figure 2.3

2.2.2 The Muon Detector

The muon detector is modular to fill a $1000m^3$ volume and consists of two ferris wheels each having eight independent octants. Figure 2.4 shows the $r-\phi$ schematic view of the muon chambers. The other $L3$ subdetectors mounted inside the muon chambers are shown as well. The polar range covered is $44° < \theta < 136°$. Each octant consists of five precision (P) chambers, two in the outer layer (MO), two in the middle layer (MM), and one in the inner layer (MI) as shown in Figure 2.5. The gas that fills the drift chambers consists of 61.5% Argon and 38.5% Ethane. In a 0.5T magnetic field the drift velocity is $51\mu m/nsec$ and the Lorentz angle is 18.8°. An outgoing muon will cross 16 sense wires in an inner chamber, 24

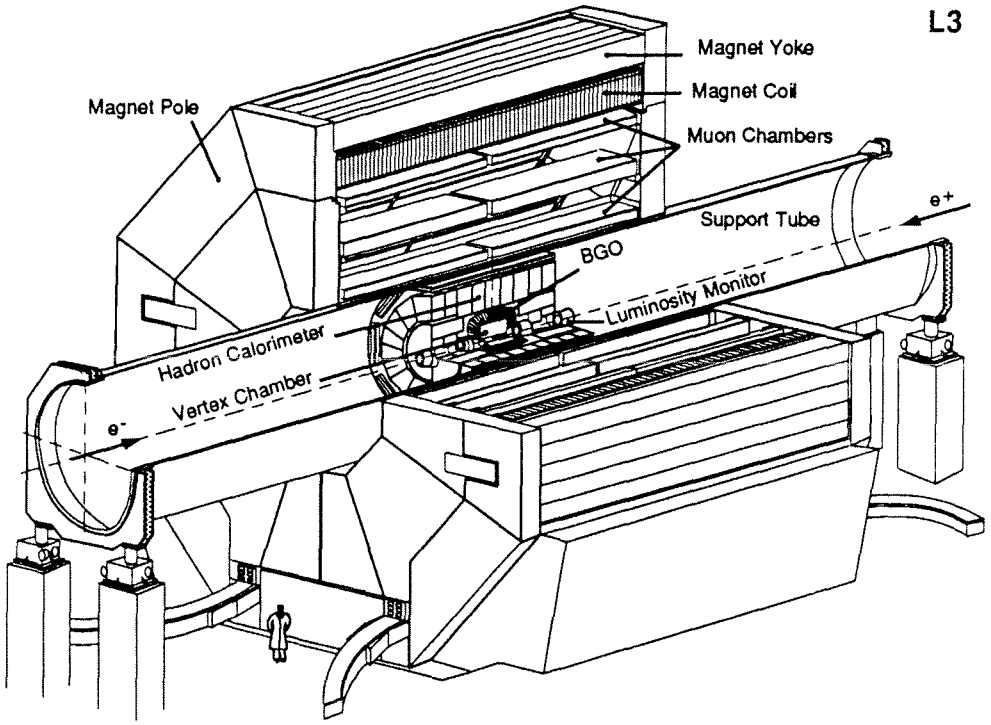

Figure 2.2: Perspective of the $L3$ detector.

in a middle chamber and 16 in an outer chamber. The L3 muon detector was designed to achieve a dimuon mass resolution of 1.4% at 100GeV. This translates into measuring the momentum of a 50GeV muon to an accuracy of $\Delta p/p = 2\%$. The sagitta of a 50GeV muon in a 0.5T magnetic field over a distance of 2.9m is 3.4mm. In order to achieve a 2% momentum resolution the accuracy required in the measurement of the sagitta is $\Delta s = 2\% \times 340\mu m \approx 70\mu m$. There are three different sources of systematic error when determining the sagitta:

- The intrinsic drift chamber resolution which depends on the single wire resolution ($200\mu m$) and the number of wires used to reconstruct each track. The intrinsic resolution contribution to the sagitta is about $54\mu m$.
- The multiple scattering inside the chambers which contributes about $31\mu m$ to the resolution.

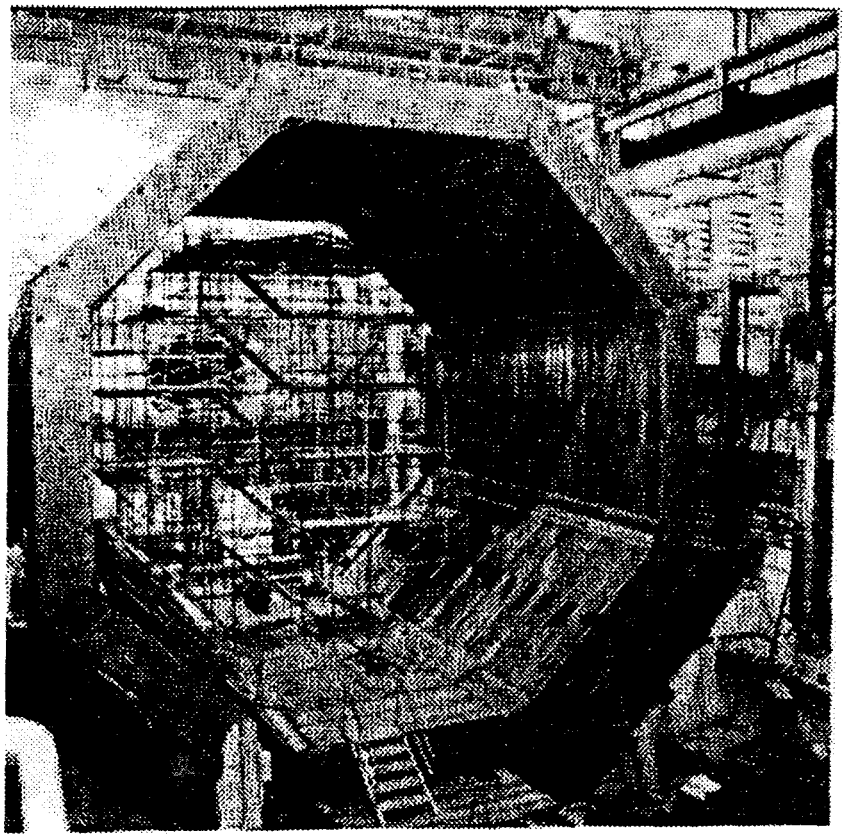

Figure 2.3: The Aluminum solenoid coil of the $L3$ detector.

- The accuracy of the alignment of the three different layers and the knowledge of the wires position which contributes about $33\mu m$ to the resolution.

The total error adding in quadrature the above contributions is $69.8\mu m$ meeting the requirement for a 2% momentum resolution. The P-chambers measure the $r-\phi$ projection of the muon momentum.

The polar angle θ of the muon is measured with z-chambers installed at the top and bottom of the MI and MO layers. The gas composition of the z-chambers is 91.5% Argon and 8.5% Methane with a mean drift velocity $30\mu m/nsec$. The typical resolution of z-chambers measured using a prototype in a testbeam is $500\mu m$.

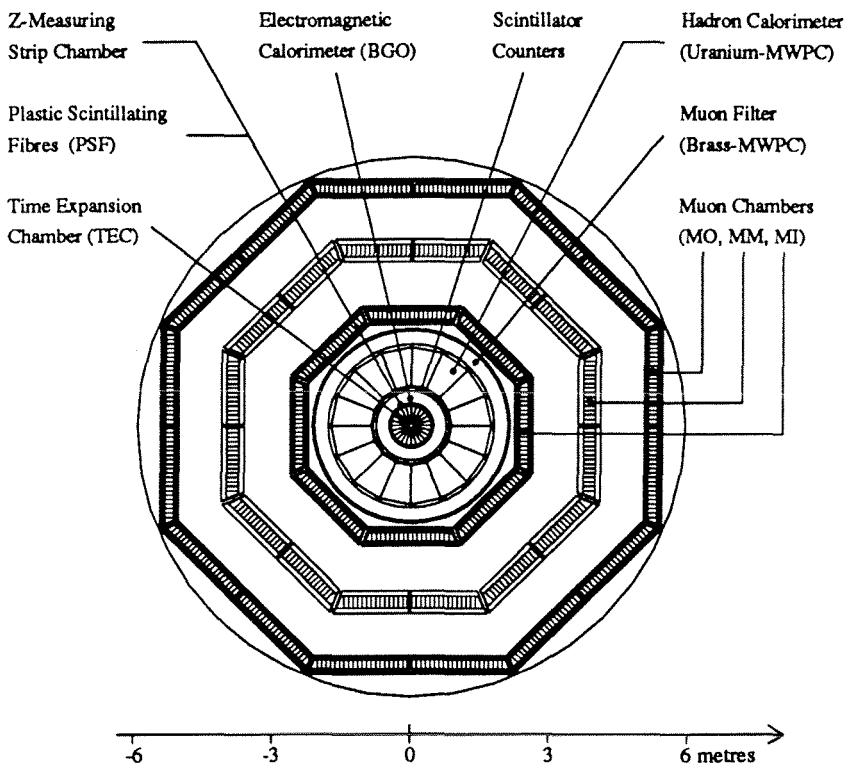

Figure 2.4: The $r - \phi$ view of the $L3$ detector.

2.2.3 The Hadron Calorimeter

The energy of hadrons emerging from e^+e^- collisions is measured with the absorption technique with the BGO crystals and the uranium hadron calorimeter. The barrel part of the hadron calorimeter covers the central region $35° < \theta < 145°$ and the forward-backward system covers the region $5.5° < \theta < 35°$ and $145° < \theta < 174.5°$. The calorimeter is made of depleted uranium absorber plates interspersed with proportional wire chambers with an 80% Argon, 20% CO_2 gas mixture. The chambers yield a signal proportional to the number of incoming charged particles which in turn is proportional to the energy of the showering particle that goes through the calorimeter. The energy resolution versus energy was obtained with a

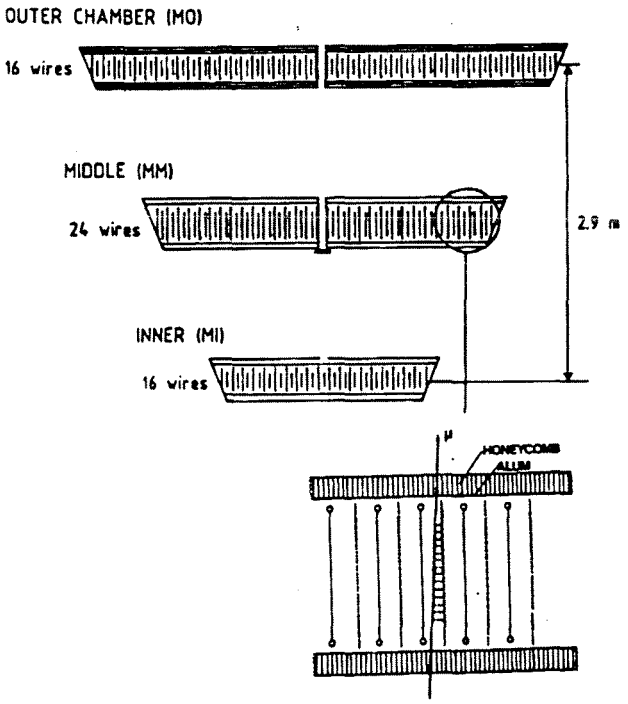

Figure 2.5: A muon chamber octant.

prototype using test beam as well as with Z^0 events and has the form:

$$\frac{\sigma}{E} = \frac{0.55}{\sqrt{E}} + 0.05 \tag{2.1}$$

The barrel hadron calorimeter has a modular structure consisting of 9 rings of 16 modules each; the three central rings consist of long modules(60 wire chambers and 58 uranium plates) and the rest of rings consist of short modules(53 wire chambers and 51 uranium plates). The barrel calorimeter is 4.725m long, has an outer radius of 1.795m, an inner radius of 0.885m for the three inner rings and 979mm for the outer rings and weighs 261t. The calorimeter is schematically shown in Figure 2.6. Each wire chamber is made of a plane of brass tubes of equal length. The $50\mu m$ in diameter gold-plated tungsten anode wires are oriented in alternate

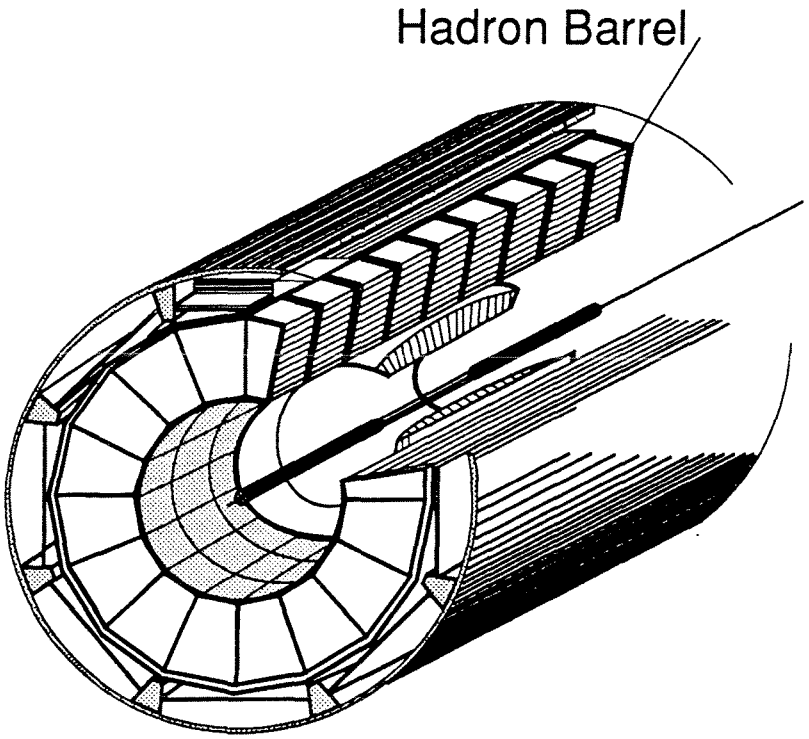

Figure 2.6: The barrel hadron calorimeter.

chamber planes at right angles to each other, thus better determining the particle trajectories. In total there are 7968 chambers and 371764 wires. In order to avoid separate readout channels the wires are, without substantial loss of granularity, organised in so-called towers. There are 9 towers in ϕ and z direction for both kinds of modules and 10(8) in the radial direction for the long(short) modules(Figure 2.7) The forward-backward detector comprises three rings on each end, one outer and two inner. Each ring is split vertically in halves and in total there are 12 separate modules. This segmentation allows for easy mounting and dismounting of the endcaps. Each module consists of stainless steel containers filled with alternating layers of proportional chambers and absorber plates of depleted uranium. Each chamber layer consists of four chambers covering an interval $\Delta\phi = 45°$.

The muon filter is located in the inside of the support tube which contains and supports all subdetectors except the magnet and the muon chambers(see Figure 2.2). The muon filter adds to the absorbtion capacity of the hadron calorimeter

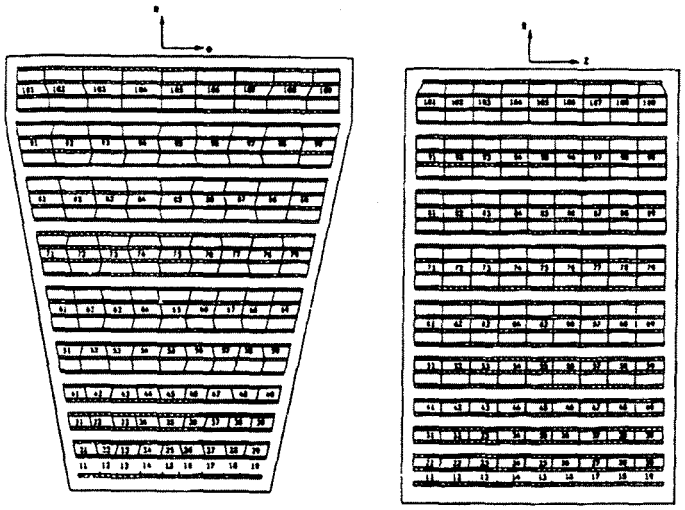

Figure 2.7: $r-\phi$ and $r-z$ view of a hadron calorimeter module. Indicated with separate numbers are the readout towers.

1.03 nuclear radiation lengths. It consists of 8 identical octants each containing 6 brass ($65\%\ Cu + 35\%\ Zn$) absorber plates interleaved with 5 layers of proportional chambers and followed by five 1.5cm thick absorber plates matching the circular shape of the support tube. An octant of the muon filter is shown schematically in Figure 2.8

2.2.4 The Scintillation Counters

The purpose of the scintillation counters is to reject cosmic muon events and keep only the genuine dimuon events from Z^0 decays. The scintillation barrel counters are mounted between the electromagnetic and hadron calorimeter. BICRON BC-412 plastic scintillators of 1cm thickness were used, each being 167mm wide in the middle and 182mm at the ends. In total there are 30 barrel counters, covering a

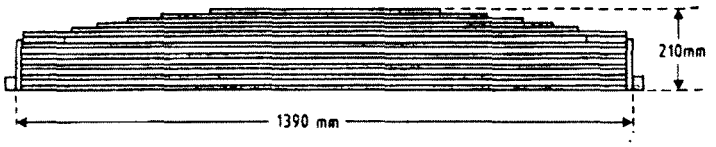

Figure 2.8: A muon filter octant.

polar region $30° < \theta < 150°$. The distance of the barrel counters from the vertex is 875mm. Consequently a cosmic ray that enters and leaves the detector causes two signals from the upper and lower counter that differ 5.8nsec and can therefore be rejected since a real dimuon-muon event will cause signals with no time difference.

The endcap scintillating counters are located in front of the endcap hadron calorimeter. There are 16 counters on either side extending the polar coverage to $25° < \theta < 155°$. The endcap counters are used to reject beam gas events that are mostly observed in the forward-backward direction.

2.2.5 The Electromagnetic Calorimeter

The electromagnetic calorimeter is inside the hadron calorimeter(barrel and endcaps) surrounding the central tracking detector and the forward-backward tracking chambers. It consists of about 11000 BGO crystals (Bismuth Germanium Oxide, $Bi_4Ge_3O_{12}$) pointing to the interaction region as shown in Figure 2.9. These crystals serve both as the showering and active medium. The BGO crystals were chosen because of their short radiation length and large nuclear interaction length. Each crystal is 24cm long and is a truncated pyramid about $2 \times 2cm^2$ at the inner end and $3 \times 3cm^2$ at the outer end. Two silicon photodiodes and associated electronics

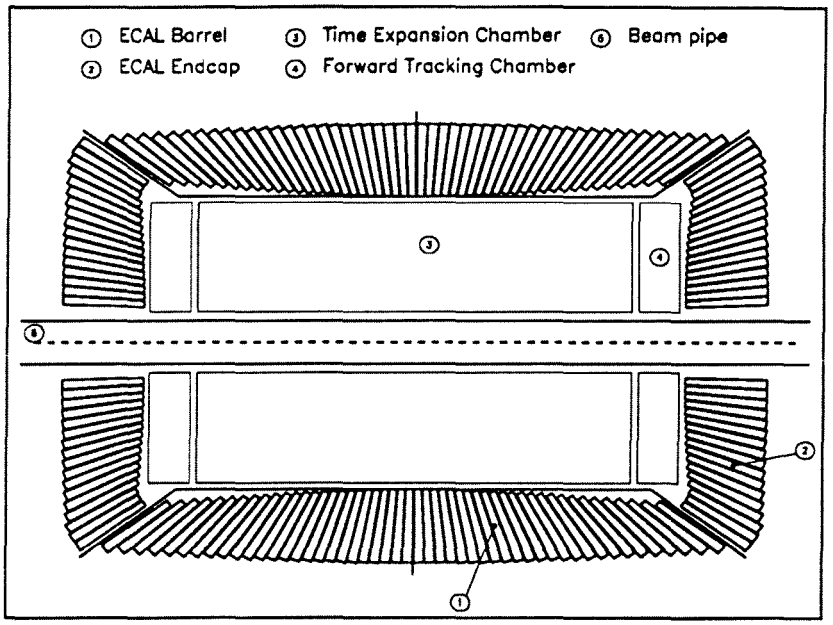

Figure 2.9: The BGO calorimeter.

are attached to the outer end to detect the light. The energy resolution is about 5% at 100MeV and 1% at energies above 2GeV. The position resolution is 2mm, better than the crystal size because a center of gravity method is used to determine the shower peak. The hadron/electron rejection ratio is of the order of 1000 for electrons above 1GeV.

The calorimeter comprises two half barrel parts with 7680 BGO crystals in total and two endcaps with 1536 crystals each. The barrel part is arranged in 48 rings of 160 crystals each, covering the polar region $42° < \theta < 138°$. Each endcap consists of 16 ϕ sectors of 96 crystals. With the endcaps the polar region covered is $12° < \theta < 168°$. Of importance in obtaining a good energy resolution is a steady temperature environment, since the light yield of BGO crystals depends on temperature with a gradient of $-1.55\%/C$. The temperature must stay above the dew point in the experimental area but as low as possible and is monitored in the front and back end of every 12th crystal. Later on during reconstruction a correction is applied for the light yield. The light collection efficiency of each crystal and the gain of the corresponding readout chain are monitored with Xenon light pulses distributed by optical fibers. There are two kinds of light pulses used;

one is to test the response of the crystal and the readout chain at high energies(light pulse equivalent to 35GeV) and the other is for low energies(light pulse equivalent to 1.5GeV) With a test beam the energy resolution obtained was 4% at 180MeV, 1.5% at 2GeV and 0.6% at 50GeV.

2.2.6 The Luminosity Monitor

The luminosity monitor is designed to measure the luminosity to 1% systematic accuracy. This is done by counting low angle Bhabha events and dividing with the theoretical prediction for the Bhabha cross-section in the limited region that the monitor covers. The monitor consists of two mirror symmetric halves with respect to the beam axis. Each half comprises a cylindrical array of BGO crystals mounted parallel to the beam axis and a tracking chamber positioned in front of the BGO crystals. The angular range covered by the luminosity monitor is from 30mrad to 62mrad which corresponds to an effective Bhabha cross-section of 100nb.

2.2.7 The Central Tracking Chamber

The *L3* central track detector is designed to achieve the following goals:

- To detect charged particles and precisely determine their direction and location.
- To determine the transverse momentum and the sign of charged particles of up to 45GeV at 95% confidence level.
- To provide the track multiplicity at the trigger level.
- To reconstruct the interaction point and secondary vertices for particles with lifetimes greater than 10^{-13}sec.

These goals must be achieved within the limited space that is available inside the electromagnetic calorimeter. The central tracking detector comprises two concentric cylindrical drift chambers on common plates that operate in time expansion mode(TEC), surrounded by two cylindrical proportional chambers with cathode strip readout, the Z-detector and a plastic scintillating fiber system(PSF).

In particular the TEC consists of an inner cylinder (1.5 mm thick Be), an outer cylinder (4 mm thick Al) and two endplates (4.5 cm thick Al). The wires run parallel to the axis of the cylinder (beam direction) from one endplate to the

other. In the rΦ plane TEC is divided in 24 outer sectors with 54 wires each and 12 inner sectors with 8 wires each. Every sector is separated from the other by a cathode plane. In the middle of every sector the signal wires define the anode plane. Figure 2.10 shows a photo of the actual TEC endplate where we can see the sector structure of the chamber. On either side of the anode plane there is a grid

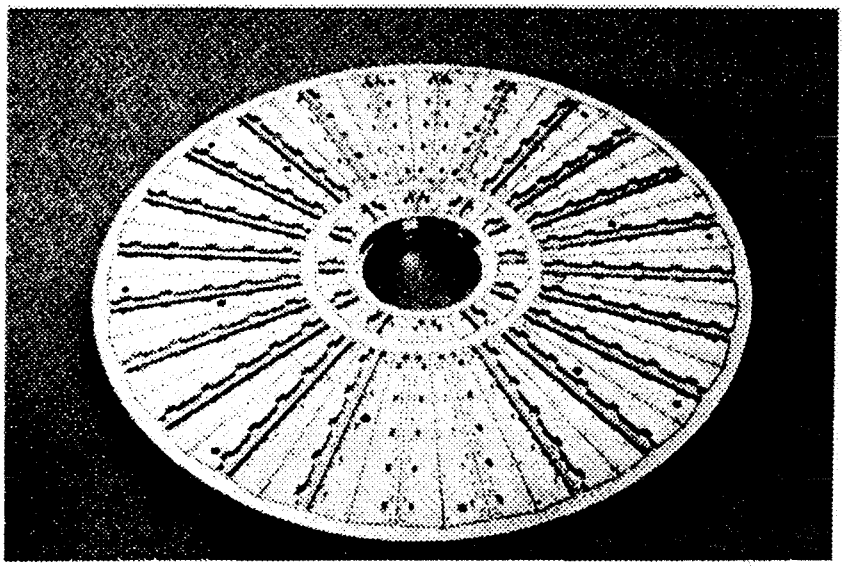

Figure 2.10: One of the TEC 4cm thick Aluminum endplates.

plane with grounded wires that separate the drift volume, from the detection gap. There are three types of signal wires, all with sensitive length of 982mm. The sense wires measure the $r-\Phi$ coordinates. The charge division(CD) wires determine the Z coordinate of the track by measuring the charge at both ends of the wire. The LR wires are groups of five grid wires on each side of an anode and are read-out to help resolve the left-right ambiguities. Figures 2.11 shows the $r-\phi$ view of an inner and two outer TEC sectors and illustrates the above. At interaction, particles travel across the volume of TEC and ionize the gas ($80\%CO_2-20\%C_4H_{10}$). Inside the drift volume the electric field is homogeneous and it has a small amplitude. A pulse of electrons drifts at a constant rate of about $6\mu m/nsec$. Upon crossing the grid plane the initial pulse is amplified through an avalanche process. This detectable electric pulse is then picked-up by the sense wires(Figure 2.12). Flash Analog to Digital Converters (FADC's) integrate the pulses and using a center of gravity method the total drift time for every pulse is obtained with an accuracy

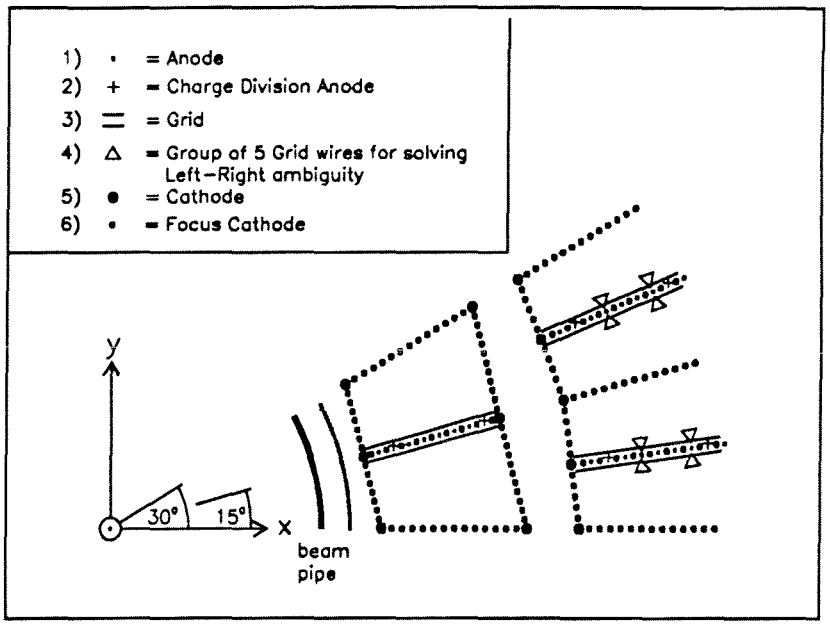

Figure 2.11: $r - \phi$ schematic view of an inner and two outer TEC sectors.

of 1ns. If the drift velocity is known then the drift distance for every pulse can be calculated. For every sense wire (62 in total) one point is reconstructed and then with a special algorithm a circle is fitted to get the track. The Z-chamber has a gas mixture of $80\% Argon$ and $20\% CO_2$. When information from the CD-wires and the Z-chamber is combined the resolution in the Z direction is better than 2mm.

The PSF surrounds the central tracking chamber with fibers running along the whole 1m TEC length(Figure 2.13). They are 1 mm thick and 0.7 mm wide (factory values). The 0.7 mm fiber width includes 0.570 mm of active area while the rest is cladding. Only outer TEC sectors are covered by fibers. Every outer sector is covered by 143 fibers, glued together to a ribbon. At one end they are divided in two halves one for either side of the anode plane. The first half has 72 fibers and the second 71 fibers. Every half is coupled to a microchannel plate multianode photomultiplier tube having 100 readout anodes and a yield of about 10^6 per initial electron. The 100 analog signals from every tube are multiplexed serially in a MX4 chip. Then a 40 m cable brings the serial analog output into an ADC discriminator with a preset threshold. Once per fill pedestals were stored and then subtracted from the analog signal before discrimination and digitization.

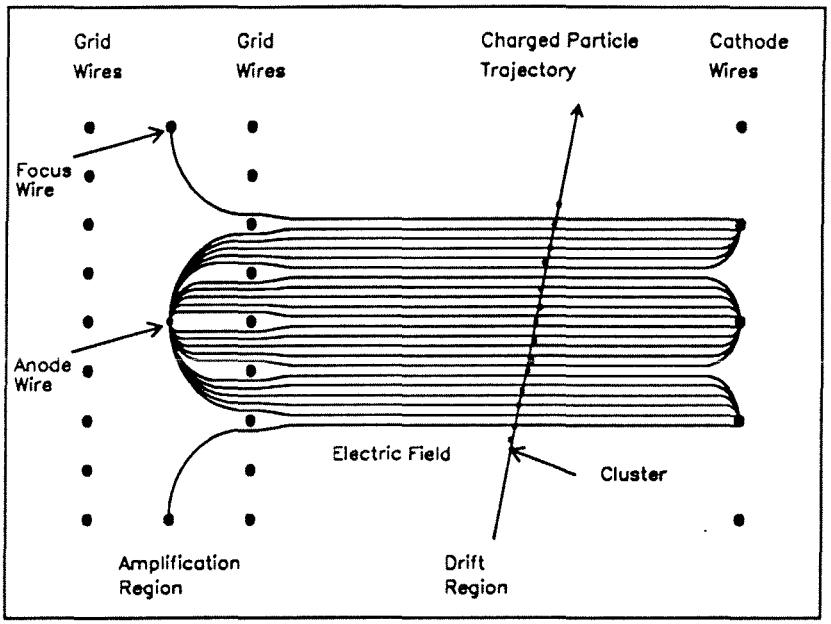

Figure 2.12: The field lines inside TEC.

So in normal operation a fiber would just give the information

whether a minimum ionizing particle went through or not. The detailed attributes of the plastic scintillating fibers and the readout system is described in detail in [27]. In order to distinguish the charge of a 45GeV particle at the 95% CL the drift velocity must be known to 0.1% accuracy. The scintillating fibers offer an external independent point which is used to calibrate TEC in an unbiased fashion to the desired level of accuracy. The principle for performing the drift velocity calibration is the following: When a minimum ionizing particle goes through a fiber we get a signal. To zero order approximation we can assume that tracks are straight. Then a line may be thought that connects the fiber and the interaction point and the drift distance for each wire can be calculated. The drift time is known from the TEC readout and the drift velocity is just the ratio of these two. To this simplified scheme correction must be applied to account for the fact that tracks are not straight, pulses do not drift perpendicular to the anode plane etc. In appendix B the offline analysis and early results are described with data collected during the 1990 physics run.

2.2.8 The Forward-Backward Tracking Chambers

The forward-backward tracking chambers are located between the TEC endflange and the BGO endcaps and cover the angular range $12° < \theta < 32°$ and $148° < \theta < 168°$. They were designed with the following goals:

- To improve the tracking in the forward-backward region.
- To provide the impact point of charged particles when they enter the BGO endcaps.
- To veto charge particles when looking for low angle photons.

Each chamber on either end of TEC consists of two perpendicular layers of 20 drift tubes. The layer closer to the interaction point measures the y-coordinate and the other layer measures the x-coordinate(in the$L3$ global coordinate system). Every drift tube has 4 sense wires that run along the tube axis and are displaced from each other in the z-direction; therefore for a charged particle that crosses an FTC chamber there are four coordinates in the y-dimension and four coordinates in the x-dimension. The single wire resolution is $200\mu m$. The gas composition of the drift tubes is 61.5% Argon and 38.5% Ethane. Figure 2.14 shows a transverse view of the $L3$ detector with all its components that have been described.

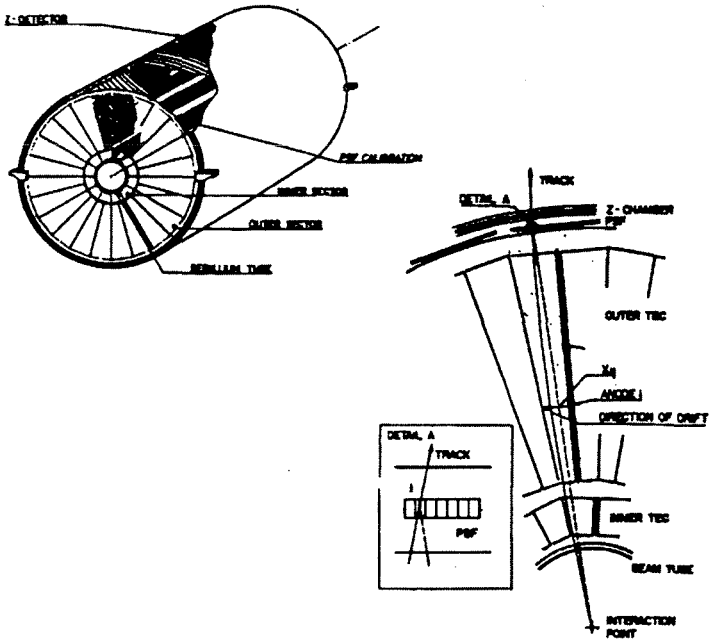

Figure 2.13: Perspective of the TEC with the PSF mounted on it. Also shown a TEC sector with a PSF ribbon.

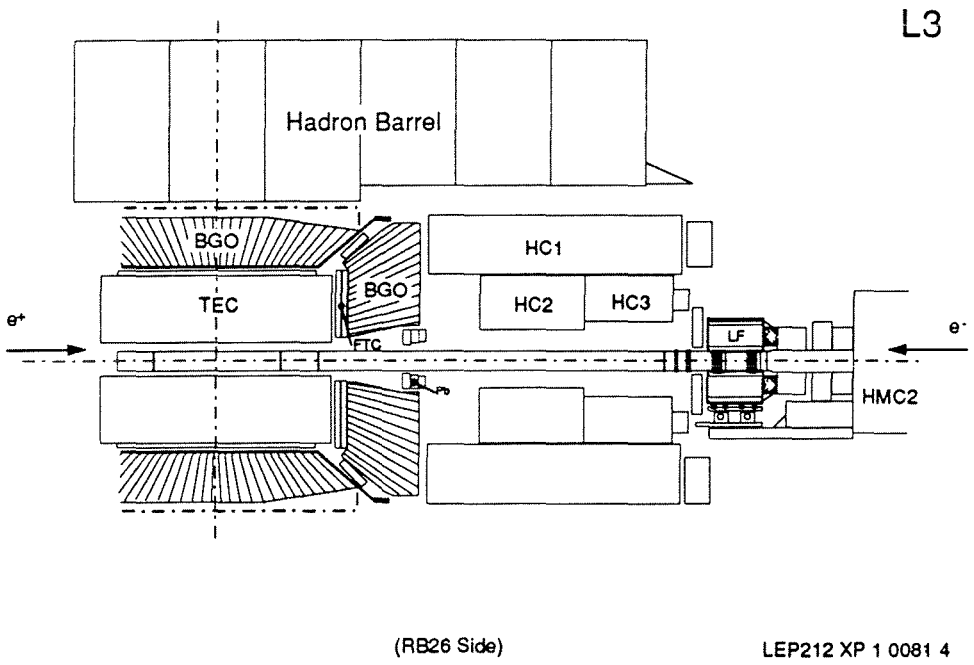

Figure 2.14: Transverse view of the $L3$ detector.

Chapter 3

Simulation.

The simulation program used for the reaction $e^+e^- \rightarrow \gamma\gamma(\gamma)$ was written by Berends and Kleiss [8]. In 1.3 all the diagrams contributing to this reaction to $O(\alpha^3)$ were given. There are two groups of corrections applied to the lowest order graphs. The first group includes all virtual corrections(Figure 1.2) and soft bremsstrahlung. The second group includes the hard bremsstrahlung corrections(Figure 1.3). We call hard the bremsstrahlung radiation when the energy of the third photon is above some cutoff value. We define the parameter $k = \frac{E_{cut\,off}}{E_{beam}}$, were $E_{cut\,off}$ refers to the minimum accepted energy for the least energetic photon. The cutoff energy depends on the detector resolution and in this analysis was taken to be $E_{cut\,off} = 0.45\text{GeV}$. The distinction between soft and hard bremsstrahlung is crucial for the theoretical cross-section calculation. If the first group of radiative corrections is applied, the lowest order differential cross-section becomes: $\frac{d\sigma}{d\Omega} = \frac{d\sigma_0}{d\Omega}(1+\delta A)$. The analytical correction δA is negative, depends on the polar angle θ and more dramatically on the cutoff parameter k through a $\log k$ term [8]. Of course a cross-section that depends on an arbitrary parameter is not physical and we would hope that including all corrections $O(\alpha^3)$ will give a result not depending on k. Indeed the hard bremsstrahlung corrections are positive and exactly cancel out this $\log k$ term. The introduction therefore of the cutoff parameter k is needed to make finite the cross-section which otherwise is infrared divergent.

The integrated differential cross-section over the full solid angle with virtual and soft bremsstrahlung corrections yields the total 2γ cross-section($\sigma_{2\gamma}$) and the integrated differential cross-section with hard bremsstrahlung yields the total 3γ cross-section($\sigma_{3\gamma}$).

Two and three photon events are generated with a ratio $\frac{\sigma_{2\gamma}}{\sigma_{3\gamma}}$. In a two photon

event each photon has half the center of mass energy, they are back to back and the polar angle θ is determined from the differential cross section. In a three photon event the differential cross section yields distributions from which we generate the energy of the third photon, its polar angle θ_3 and the polar angle of the first or most energetic photon θ_1.

The program calculates the total cross section for user defined angular cuts and center of mass energy. This is done in two steps; first for the requested center of mass energy the total $\sigma_{2\gamma} + \sigma_{3\gamma}$ cross section in the full solid angle is calculated. Consequently every event that is generated is checked if it satisfies the angular requirements. All events within the angular range are added up and then divided by the total number of generated events. This ratio is multiplied by the total cross-section to yield the cross-section in the desired region. From the number of events and the generated cross-section the luminosity is also known. The generated events are subsequently processed through detector simulation(GEANT) and reconstruction to fake the signal of real photons in the detector. Figure 3.1 shows distributions of the energies and acolinearity of the two most energetic electromagnetic clusters after detector simulation and reconstruction. Figure 3.2 shows the energy of the least energetic photon as a function of its polar angle for three photon events. From this figure is seen that the least energetic photon is mostly emitted in the forward-backward region with low energy. The region $0.72 < |\cos\theta| < 0.82$ with no data is the gap between the barrel and the endcap region of BGO.

In order to study the possible decay of Z^0 to a meson and a photon a simple Monte Carlo was done to simulate the decay of a massive spin 1 particle to $\pi^0\gamma$ or $\eta\gamma$. The particles in the final state have a $1 + \cos^2\theta$ distribution as expected for the decay of a spin 1 particle [23–25]. As mentioned in 1.4.2 the π^0 meson decays to 2γ with 98.8% branching ratio and the η meson decays into 2γ, $3\pi^0$ with 38.9% and 31.9% branching ratio respectively. The charged decays of η to $\pi^+\pi^-\pi^0$ and $\pi^+\pi^-\gamma$ have a branching ratio of 23.6% and 4.88% respectively. After detector simulation and reconstruction we saw that the decay products of both the π^0 and the η are extremely colinear and within our detector resolution the photons from the mesons in the final state appear as a single photon. Finally we also used a program by Baillargeon and Boudjema [21] that calculates matrix elements for the decay of a composite Z^0 to $\gamma\gamma\gamma$. From the ratio of the matrix elements at different angular ranges we were able to calculate the acceptance for detecting these type of events.

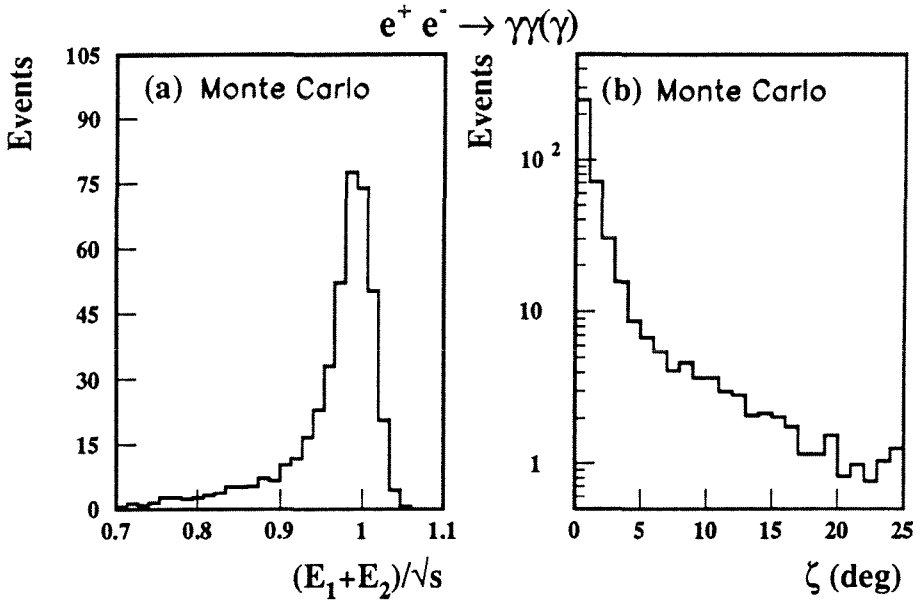

Figure 3.1: a) The sum of energies of the two most energetic electromagnetic clusters divided by the center of mass energy. b) The acolinearity angle ζ between the two most energetic electromagnetic clusters.

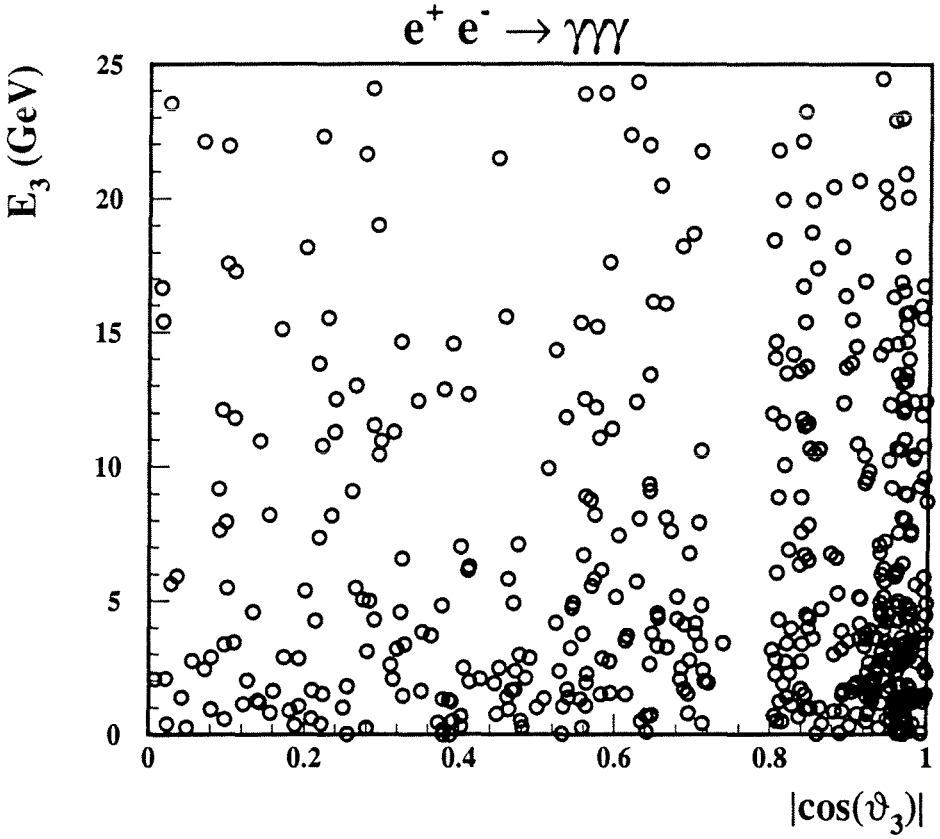

Figure 3.2: The energy of the least energetic photon versus the absolute value of its polar angle.

Chapter 4

Event Selection.

4.1 Goals and General procedure

The event selection was designed to select candidates of the following reactions:

(1) $e^+e^- \to \gamma\gamma$. This is a QED process and an excess of two photon events would indicate a breakdown of QED. This final state is also used to search for Z^0 rare decays, $Z^0 \to X$ were X is $\eta\gamma$, $\pi^0\gamma$, $\gamma\gamma$. As mentioned in 1.4.2 and in chapter 3 the π^0 meson is highly boosted and decays to 2γ which in the laboratory frame are extremely colinear. The same is true for the η meson which decays into 2γ or $3\pi^0$. Therefore the experimental signature is the same for these Z^0 rare decays as for two photons in the final state.

(2) $e^+e^- \to \gamma\gamma\gamma$. Within QED the third photon may be initial or final state radiation or may come from the virtual electron. An excess of three photon events would signal new physics. Z^0 may couple and decay to three photons if it is composite.

(3) $e^+e^- \to e^+e^-\gamma$. Within the Standard Model this is the Bhabha scattering process with initial or final state radiation. This reaction was used to understand the efficiency to detect low angle photons using the FTC, TEC and BGO endcaps.

The event selection proceeds in three steps: First the raw data written on tape during data taking are read and processed through the L3 reconstruction program. After reconstruction a preliminary selection splits the data into different general

physics streams and outputs them to tape. In parallel, the integrated luminosity for every run is calculated and the results are available in a luminosity list. In a second step the tapes with the physics stream of interest are read back and the data are further reduced by writing out ntuples with only the necessary information for the analysis to be performed. The ntuples are data structures where for every event an array of fixed length is reserved. Every element of this array corresponds to some variable of the event. The ntuples have a small enough size so they can be kept on disk. In a last third step the ntuples are read and specific selections are made one for every physics process listed above. The description of the event selection follows the above natural sequence.

4.2 Trigger, Reconstruction, First Selection, Luminosity

During Data AQuisition(DAQ) the various subdetectors send signals which are written on tape if they pass a three level trigger system. Level one trigger is based on the TEC detector, the calorimeters, the scintillators, the muon chambers and the luminosity monitor. For this analysis the TEC, calorimetric and luminosity trigger is essential. The TEC trigger requires at least two tracks inside the TEC with an opening angle greater than 120° in the $R-\phi$ plane. The calorimetric trigger is designed to select events if the energy deposited in the BGO or the hadron calorimeter exceeds some threshold. At least one of the following conditions must be satisfied:

(1) The energy deposited in the BGO must be more than 20GeV.

(2) The energy deposited in the barrel BGO must be more than 10GeV.

(3) The total energy deposited in the barrel BGO and hadron calorimeter must be more than 15GeV.

(4) The total calorimetric energy must be more than 20GeV.

The luminosity trigger is based on a logical 'or' of one of the following three criteria:

(1) Two back to back depositions of energy with more than 15 GeV

(2) The total energy on one side greater than 25 GeV and on the other side more than 5 GeV

(3) The total energy in either end greater than 30 GeV

The total rate of level one trigger is about 8 Hz with a 5% dead time.

Level two and three triggers decrease the above rate and reject events selected by level one trigger. This is done by combining information and spending more time per event reducing the overall data taking rate to $2-3$ Hz. The trigger efficiency for any of the reactions listed in 4.1 is better than 99.9%. During DAQ the $L3$ database is updated in regular intervals or whenever there is a change in the configuration of a subdetector.

The $L3$ reconstruction program is run offline and receives as input the raw data(drift times, pulse heights etc.) written on tape during DAQ. The reconstruction program processes the raw data and creates data structures that can be used thereafter from the different physics analysis groups to study the events. For this analysis the information from the TEC, the FTC, the BGO and the Luminosity monitor was mainly used.

During reconstruction the drift times in the TEC are translated to drift distances in the $r\phi$ plane(the plane that intersects vertically the beam axis) using the drift velocity in the chamber. The PSF system described in 2.2.7 and in Appendix B was used along with an internal calibration method to define the drift velocity. A drift distance is always measured relative to a wire and from the x, y coordinates of the wire a point is defined on the $r\phi$ plane. A wire may be associated to more than one points depending on how many charged particles went through that particular TEC sector. Few points also have a z coordinate if they belong to charge division wires. Since the drift time does not contain the information on which side of the anode plane the charged particle went through, every point has a mirror image with respect to the anode plane. To resolve these ambiguities we rely on the left-right pickup wires but most importantly on the asymmetry between the anode planes of inner and outer TEC(see Figure 2.11). Points are combined to pairs and pairs are grouped to circle segments. If the wrong ambiguities have been chosen then segments from the inner TEC will not match segments from the outer TEC. Circle segments of the correct ambiguity will yield the final reconstructed track. For every track we know its curvature, charge, number of wires used in the fit, the outermost and innermost wire used, the distance of closest approach of the track to the vertex(DCA) etc. With the drift velocity known to 0.1% the single wire resolution is about $50\mu m$ and the charge of a 45GeV particle can be determined at 95% CL. Later on in the analysis the user has access to either the track data structures or if he wishes to the individual hits detected inside TEC. Figure 4.1 shows a reconstructed event which is classified as a radiative Bhabha.

There are two TEC tracks associated with two depositions of energy in the BGO and one deposition of energy with no track. Points not used in the track fit are indicated with crosses. It is clear that a few of these unused points correspond to the mirror image of the track with respect to the anode plane(the anode plane is not shown in this figure).

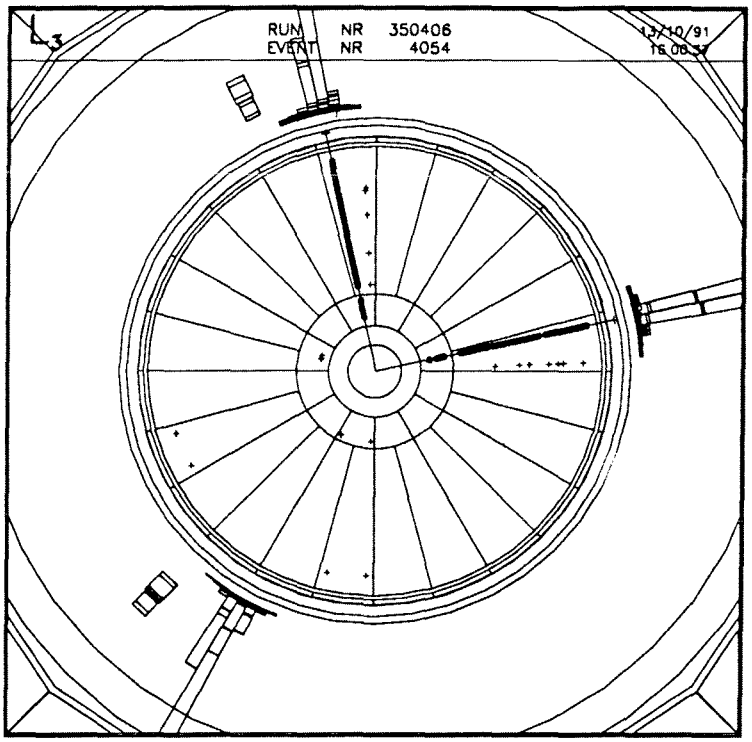

Figure 4.1: The $r - \phi$ view of a radiative Bhabha event. The TEC tracks can be seen. The used points in the fit are indicated with circles and the unused points with crosses.

The input to the BGO reconstruction are the pulse heights of the crystals. First the pedestals are subtracted from the pulse heights which are then multiplied with the calibration constants to yield energies. The crystals are calibrated with Xenon light pulses distributed by optical fibers(section 2.2.5). Because the photon yield of the BGO crystals depends on the temperature we apply temperature corrections to the energy of every crystal. All adjacent crystals with energy more than a 100 Mev are grouped to clusters. Within a cluster we define bumps which are local maxima of energy deposition. The θ and ϕ coordinates of a bump are derived from the

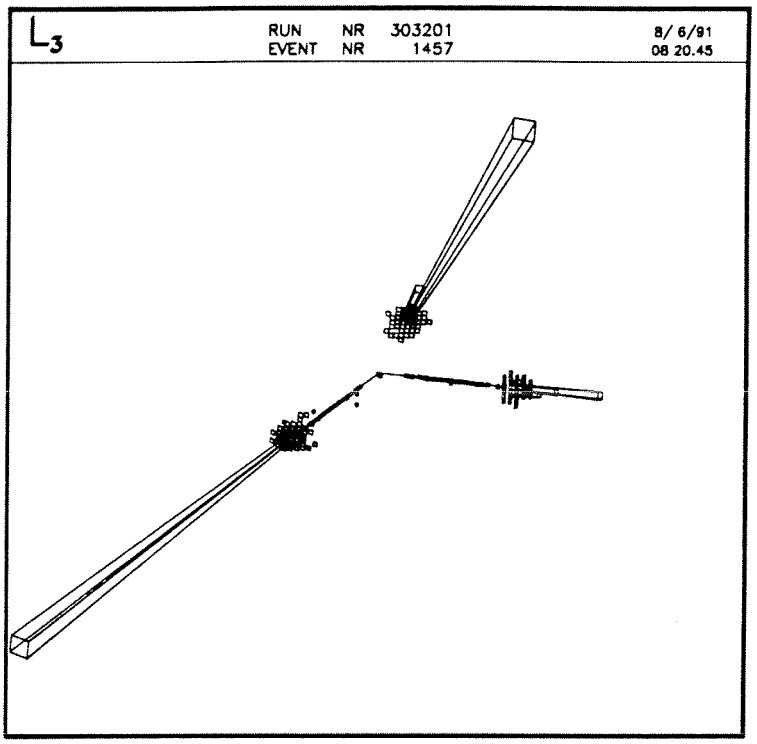

Figure 4.2: A radiative Bhabha event. The sharing of energy between crystals within a bump is demonstrated.

energy sharing between crystals. This is done using a fitting function derived from the average shape of electromagnetic showers. The energy of the incident particle must be corrected for lateral and rear leakage. These corrections depend on the nature of the particle(electron/photon,hadron). After corrections are applied the sum of energies of the eight closest crystals plus the energy of the central one gives our best estimate of the energy of the particle. The energy resolution is better than 1% for particles with energy more than 2GeV and the spatial resolution achieved is better than 2mm. Figure 4.2 shows a view of a radiative Bhabha event where the BGO crystals participating in a bump are drawn as square towers. The height of every tower is equivalent to the energy deposited in the crystal. The central crystal of every bump carries most of the energy.

The reconstruction of data in the hadronic calorimeter provides clusters with the hadronic energy deposited in the event. Muon chamber data are fit to yield the muon tracks with momentum and charge information. Figure 4.3 shows a recon-

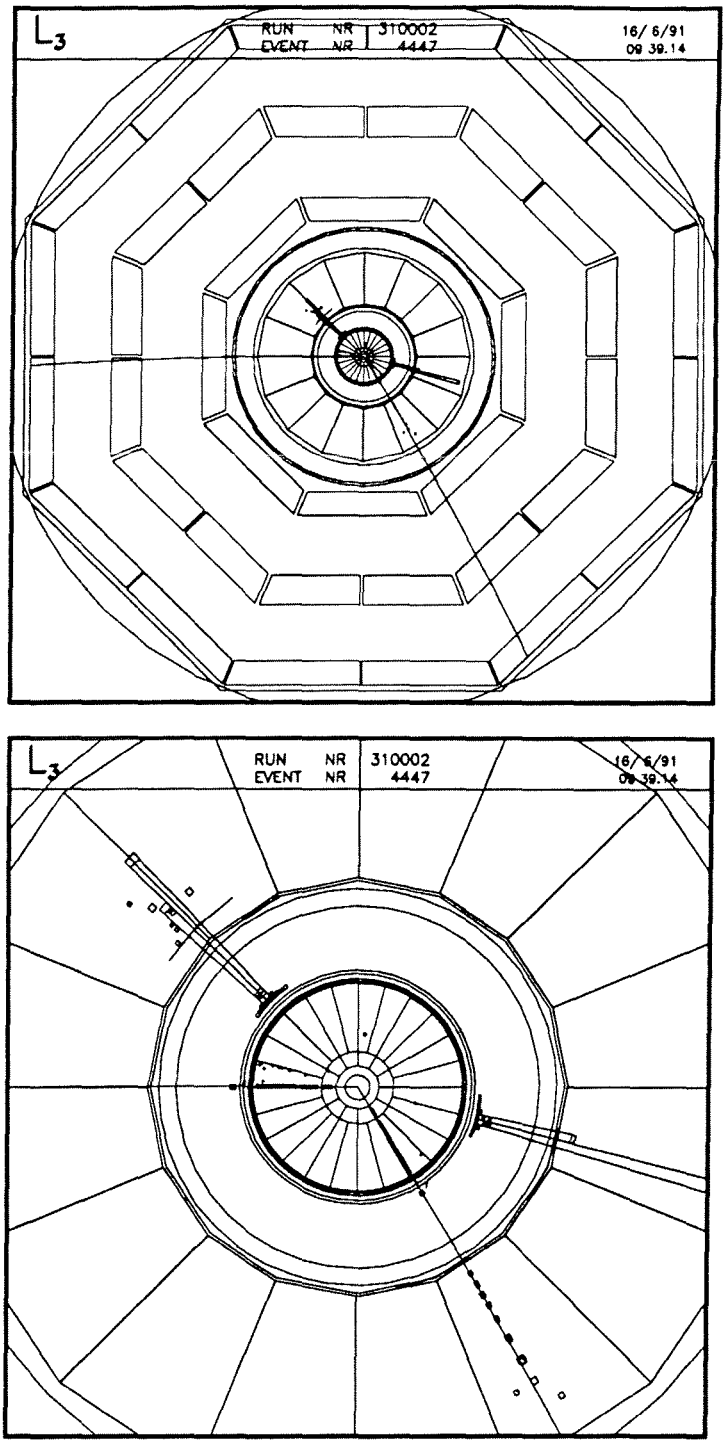

Figure 4.3: A doubly radiative dimuon event. The top picture shows the $r - \phi$ view of the whole detector. The bottom picture focuses on the TEC and the BGO. The TEC and muon chamber tracks match.

structed doubly radiative dimuon event. At the top picture the reconstructed muon tracks can be seen and the bottom picture has focused on the TEC and BGO. The two tracks reconstructed using the TEC match exactly the tracks reconstructed from the muon chamber data.

After reconstruction different analysis groups apply selections to create physics 'streams'. These 'streams' are pass-one selections focusing on particular physics processes and are usually optimized to give a very high efficiency. For our analysis we created the Bhabha stream. All events that have most of the energy in the BGO are selected. The cut applied requires at least 65% of the minimum center of mass energy(which is 88 GeV) to be deposited inside BGO. Figure 4.4(a), (b),(c),(d) shows Monte Carlo distributions for the energy deposited in the BGO for various Z^0 decays. The above cut eliminates 93% of hadron events, practically all of $e^+e^- \rightarrow \mu^+\mu^-$ events and 96.3% of $e^+e^- \rightarrow \tau^+\tau^-$ events. The efficiency of the above cut for selecting $e^+e^- \rightarrow \gamma\gamma(\gamma)$ or $e^+e^- \rightarrow e^+e^-\gamma(n\gamma)$ is 84.5% in all solid angle and 95.9% for $14° < \theta < 166°$.

Source of Systematic error	$\Delta\mathcal{L}$ (%)
Luminosity Trigger	0.1
Geometry of the Calorimeters	0.4
Bhabha Event Selection	0.5
Background Subtraction	0.1
Monte Carlo Statistics	0.3
Theoretical Cross-Section Error	0.5
Total Systematic Error	0.9

Table 4.1: Contributions to the Luminosity error calculation

The luminosity is measured using low angle Bhabha events detected by the luminosity monitor and the theoretical Bhabha cross-section; $N = \mathcal{L} \times \sigma$ where N is the number of detected events, corrected for acceptance and background, and σ the theoretical Bhabha cross-section. Since events are expected to be highly energetic the pedestals are set to high enough values and the noise level is not significant. The final selection of events that will be used for the luminosity calculation requires:

(1) The reconstructed θ, ϕ impact coordinates of the clusters must be at least one crystal away from the edges of the calorimeter

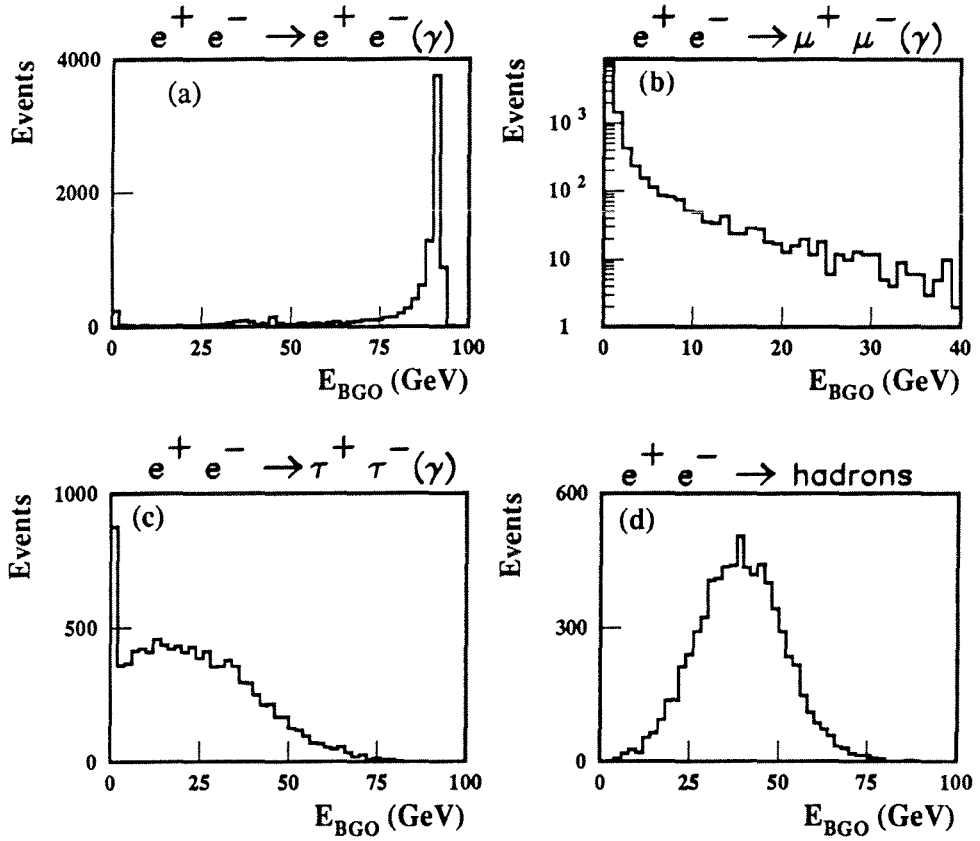

Figure 4.4: Total energy deposited in the BGO for center of mass energy 91.2 GeV. (a) In bhabha events most of the energy is deposited in the BGO, since electrons and photons interact electromagnetically. (b) In dimuon events almost no energy is deposited in the BGO unless there is initial or final state radiation. Muons are minimum ionizing particles. (c), (d) In tau and hadronic events a fraction of the energy is deposited in the BGO.

(2) At least $0.8E_{beam}$ of energy on one side and $0.4E_{beam}$ on the other

(3) the acoplanarity $\Delta\phi$ of the clusters to be less than 10°

The asymmetric energy cut ensures that the selection will not be biased from a few dead crystals on one side and in addition to that it keeps most of radiative Bhabhas. For the theoretical cross-section the BABAMC Monte Carlo is used which is order $O(\alpha)$. The effect of higher order contributions leading to $O(\alpha^2)$ have been included with an analytic calculation. Different sources of uncertainties lead to a total systematic error of 0.9%. These sources and their contribution are listed in Table 4.1

4.3 Data Reduction

The Bhabha stream was reprocessed and ntuples were filled with only the necessary information for every event. In particular for this analysis for every event we looked at the four most energetic electromagnetic bumps and recorded their energy, their polar and azimuthal angles θ, ϕ and also checked whether there was a charged particle associated to these bumps. For the whole event we also recorded the fill number, run and event number, the time it happened, the beam energy and the total energy in the BGO.

The energy of every bump is the sum of energies after corrections are applied of the nine crystals participating in the bump. The θ, ϕ of every bump are derived with a center of gravity method as described in the previous section.

At this stage the only additional cuts applied before creating the ntuples were meant to eliminate noisy crystals and events with high bump multiplicity, mainly hadronic events left over from pass-one selection. To eliminate noise we kept only bumps with: a) $\frac{E_{central\ crystal}}{E_{bump}} < 0.9$ and b) $E_{bump} > 0.01$ GeV. An event with more than 15 bumps was excluded. Figure 4.5 shows the distribution for the number of bumps for Bhabha/two photon and for hadronic Monte Carlo events.

Two additional parameters are also recorded that identify whether the showering particle was an electron/photon or a hadron. For a particle that showers inside BGO all the energy is contained within some radius from the impact point which is much smaller for electrons and photons than for hadrons. The quantity:

$$\frac{S_9}{S_{25}} \equiv \frac{\text{Energy Sum of the 8 closest crystals plus the central one}}{\text{Energy Sum of the 24 closest crystals plus the central one}}$$

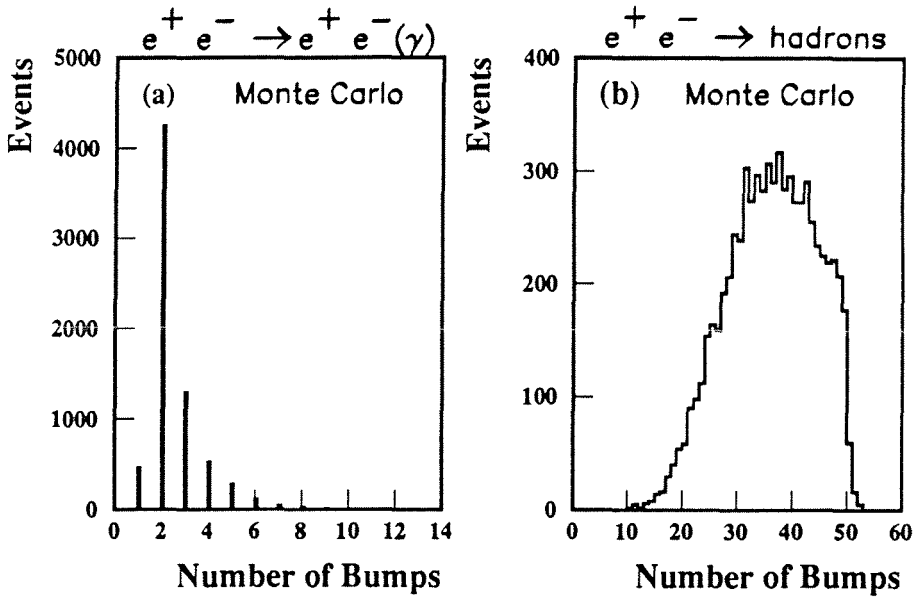

Figure 4.5: (a) Number of bumps for Bhabha or two(three) photon events. (b) Number of bumps for hadronic events.

determines the nature of the showering particle. For an electron or photon $S_9/S_{25} > 0.95$. This can be seen in Figure 4.6 where S_9/S_{25} is plotted for electron and pion test beam data. The second parameter is:

$$\chi^2 \equiv \sum_{i=1}^{9}((E_{i\ seen} - E_{i\ expected})/\sigma_{i\ expected})^2$$

where $E_{i\ seen}$ is the energy deposited in the crystal, $E_{i\ expected}$ is the energy expected to be contained within this crystal and $\sigma_{i\ expected}$ is the energy resolution of the crystal. Both $E_{i\ expected}$ and $\sigma_{i\ expected}$ have been determined once for every crystal using an electron test beam by injecting electrons of known energy at specific positions on the surface of the crystals and then measuring the response and resolution of the crystals. The sum defining the χ^2 is over the energies of the eight closest crystals plus the central one. The above χ^2 parameter describes how probable it is for the particle observed to be an electron or a photon(since photons leave the same signature in the BGO as electrons). Table 4.2 shows the variables stored for every bump and for the whole event.

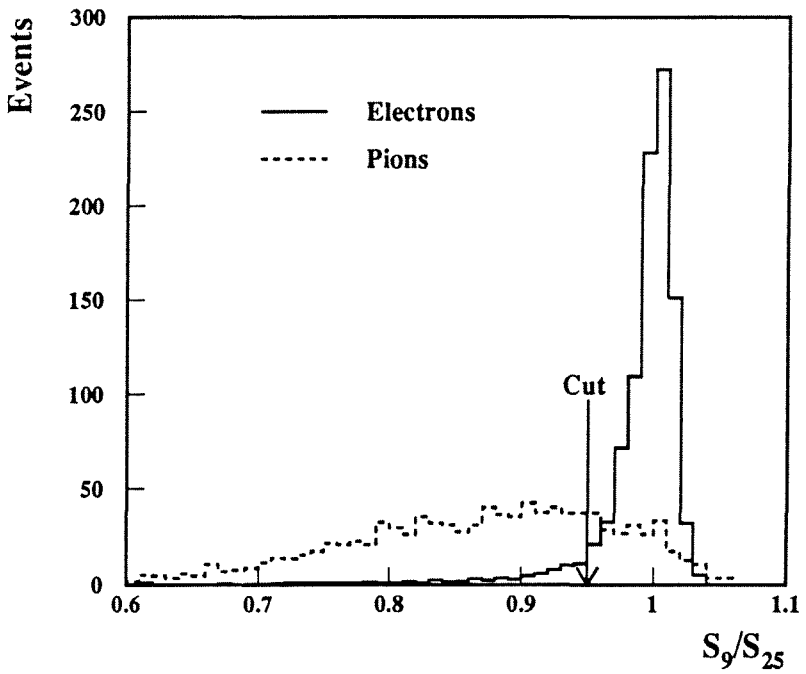

Figure 4.6: The sum of energies of the nine crystals divided by the sum of energies of the twenty five crystals for electron and pion test beam data.

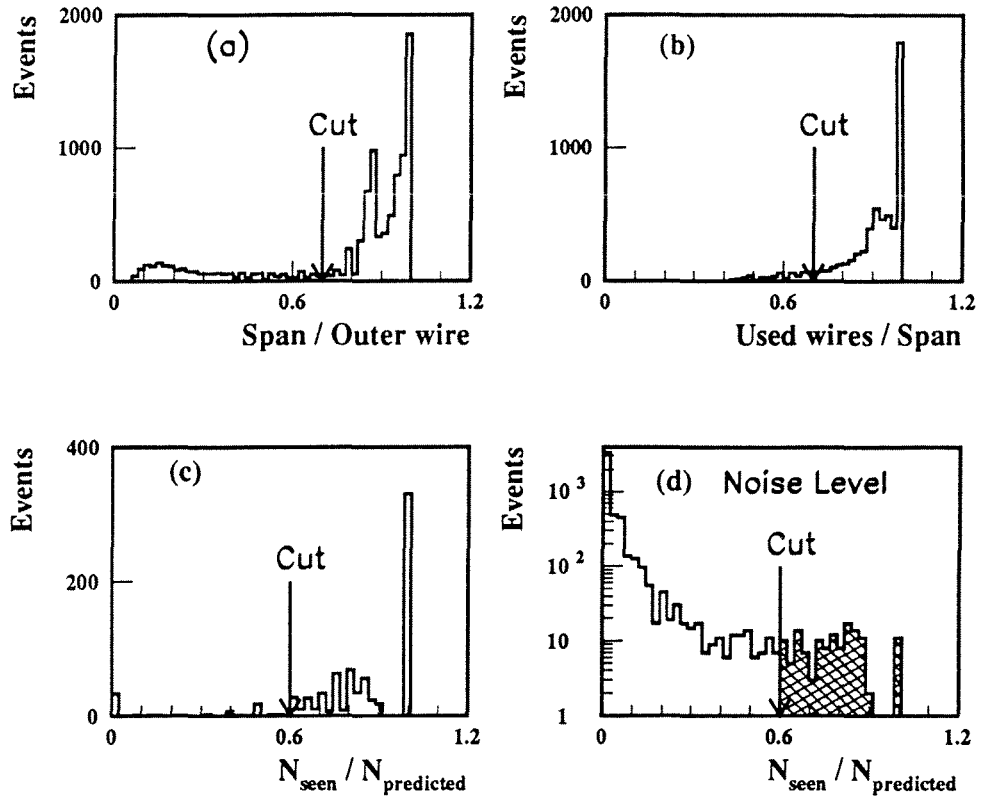

Figure 4.7: When a track is reconstructed:(a) The span divided by the outermost wire. The second peak is when the inner TEC sector is not operational. (b) Number of used wires divided by the span. Plots (c) and (d) refer to the case when a track is not reconstructed: (c) Number of wires that gave a hit divided by the predicted number of wires that the outgoing particle crossed. The search for wires that gave a hit was done behind the bump in a 3° opening angle in the $r\phi$ plane. (d) Same as case (c) but away from the bump. Only the hatched area is noise that faked a charged particle. Data was used for all four plots.

For every bump	For the whole event
Energy	Fill Number
θ	Run Number
ϕ	Event Number
Matched Track(1 or 0)	Time
S_9/S_{25}	Total BGO Energy
χ^2	Number of bumps
	Beam Energy

Table 4.2: The ntuple variables stored for every event.

The selection of tracks was based on criteria that ensure a high quality track(not electronic or beam gas noise, cosmic rays) and also took into account the need of detecting low angle tracks. Span of a track is defined as the outermost minus the innermost wire and effectively describes the track length. This can be different from the number of wires used in the track fit because wires in between the outermost and innermost may have been excluded from the fit. We accepted tracks that satisfied the following criteria:

(1) $DCA < 10$ mm

(2) $\frac{Span}{Outermost\ wire} > 0.7$

(3) $\frac{Used\ wires}{Span} > 0.7$

The first cut is applied to eliminate most of cosmic rays since they do not point to the vertex. For the second and third cut we note that when a particle leaves the TEC endflange it does not cross all 62 TEC wires. In fact at very low angles we would loose many of the tracks if a fixed cut on the span or the number of used wires was applied. The variable cuts (2) and (3) listed above select a track even at low angles since the span required is a percentage of the last wire that was used. The same is true for the number of used wires. Figure 4.7(a),(b) shows these distributions for the data and the cut that was applied for selecting good tracks.

If there are tracks in the event then every bump will be assigned the closest track. For this analysis the events have low charge multiplicity and the association of a track with a bump is done only on the $r\phi$ plane using the azimuthal angle

ϕ_{bump} of the bump and the extrapolated to the BGO cylinder azimuthal angle ϕ_{track} of the track. The resolution for matching in this way TEC tacks with BGO bumps, after an offline correction is applied for the alignment between TEC and BGO , in Bhabha events is about 2 mrad and is shown in Figure 4.8. A gaussian is superimposed.

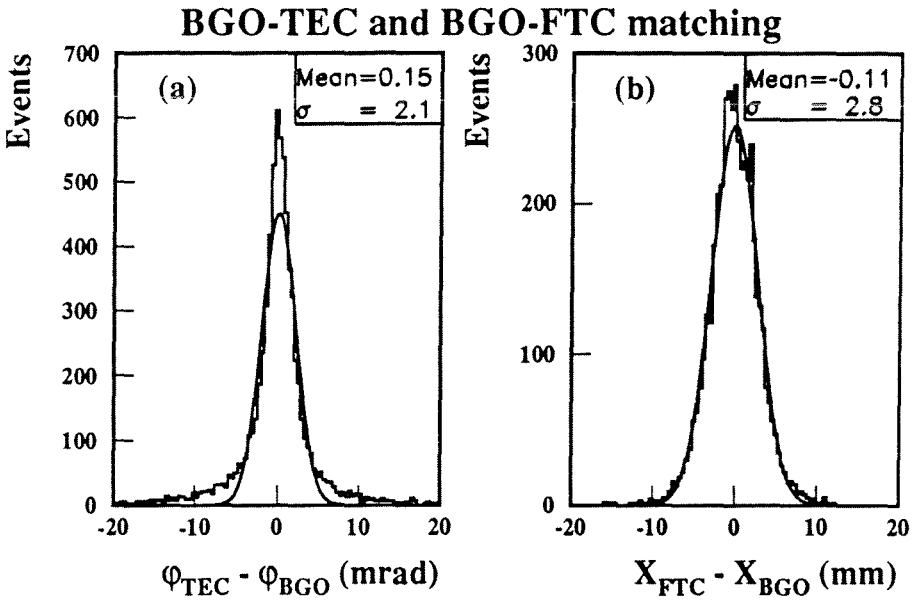

Figure 4.8: Matching between TEC-BGO and FTC-BGO for Bhabha events.

There are cases when a track is not reconstructed even though a charged particle went through the TEC. This happens particularly at low polar angles $|\cos\theta| > 0.82$ where the reconstruction efficiency is lower. However the hits of individual wires exist and are used to give a complementary answer on whether or not a bump in the BGO corresponds to a charged particle. A simple track finding algorithm was used to recover lost tracks. From the position of the bump and the vertex, we know how many wires the particle crossed before leaving through the TEC endflange. This number of wires is defined as $N_{expected}$. Then in the $r\phi$ plane a 3° opening angle around the bump was defined, centered on the vertex. All TEC wires that give a hit inside this angle are counted up. If there are no hits in this angle but there are in its mirror image with respect to the anode plane we still count them

up. This is because unless there are left-right ambiguity resolving wires used we cannot say which side of the anode plane the particle went through. If we define the total number of seen wires as N_{seen} then the ratio $N_{seen}/N_{expected}$ exhibits a sharp peak at one. This distribution is shown in Figure 4.7(c) with data. We made a cut at $N_{seen}/N_{expected} = 0.6$ and any bump with a number of associated hits more than that was considered to be coming from a charged particle. The noise level of TEC within the 3° small opening angle is very small. In order to determine the noise level, α, the opening angle was arbitrarily rotated around the vertex and the same ratio $N_{seen}/N_{expected}$ was plotted again (Figure 4.7(d)). The noise level is very low and in only 3% of the cases noise would fake a charged particle.

At very low polar angles($0.8829 < |\cos\theta| < 0.97$) the FTC provides additional information about the particle that went through and the FTC hits were recorded for this bump. When this analysis was done a complete algorithm that would combine FTC and TEC hits to a single track was not available. As a consequence FTC hits were used to identify a charged particle when neither TEC tracks nor even TEC hits were found. For every bump we interpolated between the bump and the vertex through the FTC and looked for FTC hits. The closest hits were every time assigned to the bump if they were separated from the interpolated bump position less than 30 mm. To every bump in the angular range $0.8829 < |\cos\theta| < 0.97$ we assigned two numbers; the average separation between FTC hits and the interpolated bump position to the FTC X plane(Figure 4.8) and the same average separation with the bump position interpolated to the FTC Y plane. In general we assumed that if at least two FTC hits were behind the BGO bump on either the X or the Y plane then a charged particle went through. The reason for not requiring both the X and Y planes to give hits is that there are regions that both planes may not be active, because of cabling etc. In about 5% of the cases a charged particle could go through inactive regions. If there is a BGO bump with at most one FTC hit behind it on either the X or the Y plane then the decision is that a photon went through.

4.4 Final Selection, Luminosity Correction

During the third step of the event selection the ntuples are read back and three individual selections are performed one for every of the following three reactions.

(A) $e^+e^- \rightarrow \gamma\gamma(\gamma)$

Events candidates of the above reaction were selected with the following cuts:

(1) At least 70% of the center-of-mass energy must be in the BGO.

(2) The number of bumps in the BGO must be less than 9.

(3) The acolinearity angle between the two most energetic bumps must be less than 25°.

(4) No tracks reconstructed inside TEC and one or zero tracks reconstructed inside FTC.

Cuts 1 and 2 (See Figures 4.4 4.5) eliminate all hadronic events and leave 1.2% $\tau^+\tau^-$ background, which is removed by cut 4. A few $\tau^+\tau^-$ Monte Carlo events have no tracks, but this is because the charged particles are emitted at very low polar angles. These events will be excluded in the analysis because they are outside our acceptance. Cut 4 also eliminates the Bhabha background. It is very important to detect these tracks because the Bhabha cross section is an order of magnitude higher than the two photon cross-section and a small inefficiency in the TEC or the FTC would contaminate our sample significantly. If the two bumps are in the angular coverage of FTC and TEC has reconstructed no tracks then only if FTC has 'seen' two tracks the event will be excluded. This was done to increase the efficiency for selecting two photon events because as will be described in 5.2 photons may convert to an electron-positron pair while crossing the TEC endflange or may cause backscattering of electrons while entering the BGO endcap. An optimization had to be reached to exclude all Bhabha background but keep the efficiency as high as possible. Cut 3 eliminates mainly cosmic ray background and low multiplicity noise events.

(B) $e^+e^- \rightarrow \gamma\gamma\gamma$

In this class of events we wish to select events with at least three photons in the final state. Keeping the previous cuts 1,2 and 4, we added the following ones:

(1) There must be at least 3 bumps in the BGO.

(2) The energy of the least energetic cluster must exceed 3 GeV.

(3) The least energetic cluster should have $S_9/S_{25} > 0.95$ and $\chi^2 < 20$

(4) The angle in space between any two bumps must be larger than 25°.

(5) The sum of the angles in space between bumps must be more than 350°, thus ensuring that the event is coplanar.

Cut 3 ensures that the third bump is electromagnetic. The coplanarity of the event(cut 5) is necessary to ensure that we really have three particles in the final state. Cuts 2 and 4 are designed to yield three photon events that deviate from the standard QED expectation. QED three photon events have the third photon at low energies and very colinear to one of the other two photons. Figure 4.9 shows the energy of the least energetic photon versus the minimum angle in space between any two photons for QED Monte Carlo events and Figure 3.2 shows the energy of the least energetic photon as a function of its polar angle. Two of the events selected with these cuts are shown in Figure 4.10. The top picture shows a three photon event with two photons being detected in the BGO endcaps. The second event is in fact a four photon event with all photons detected in the barrel BGO region. The least energetic photon has 0.7GeV of energy. The energy of the four photons adds up almost to the beam energy. There is some energy deposited in the hadron calorimeter(1.2GeV) which may be noise. The beam energy for this event is 91.27GeV and in total 90.47GeV is deposited in the BGO. This a very unlike QED event. It could be an electron-positron annihilation to two photons with two additional photons from initial state radiation. Unfortunately the Monte Carlo available was only $O(\alpha^3)$ and the probability for this event to be QED was not calculated. This is the only four photon event that we observed in 1990 and 1991.

(C) $e^+e^- \rightarrow e^+e^-\gamma(n\gamma)$ Of interest here is at least two electrons and one or more photons in the final state. The following cuts were applied to select candidates for this reaction.

(1) At least 70% of the center-of-mass energy to be in the BGO.

(2) The number of bumps in the BGO must be more than 3 but less than 9.

(3) Two of the clusters should have a track associated to them and the bumps with the tracks should be outside the region covered by FTC.

(4) The energy of the least energetic cluster must be more than 1 GeV.

(5) The bump with no associated track should have $S_9/S_{25} > 0.95$ and $\chi^2 < 20$

(6) The opening angle between any two bumps must be more than 8°.

Again cuts 1 and 2 eliminate all hadronic events and leave 1.2% $\tau^+\tau^-$ background. The remaining $\tau^+\tau^-$ events cannot be excluded. Cut (3) ensures

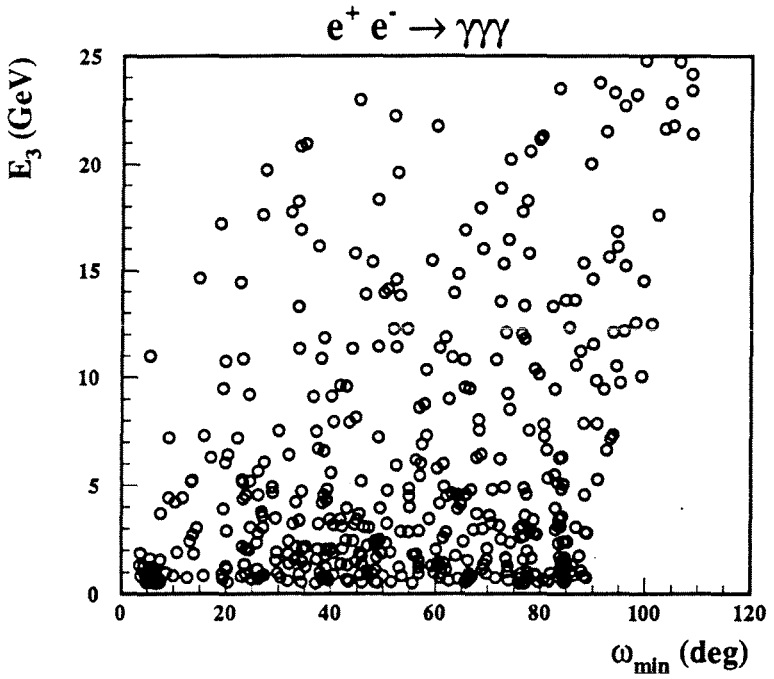

Figure 4.9: The energy of the least energetic photon versus the minimum angle in space between any two photons

that there are two charged particles and a photon. In order to study the detection efficiency for photons at low angles(Chapter 5) the photon will be required to be at the BGO endcap in a region covered by FTC but at the same time we wish the electrons to be away from the photon to avoid association of FTC hits to the photon. Cuts (4,5,6) ensure that the event is not noisy. One example of event selected with the above set of cuts is the doubly radiative Bhabha event shown in Figure 4.11. The two electrons are detected with the TEC and the barrel BGO, one photon is in the barrel BGO and one photon has crossed the TEC endflange and the FTC before entering the BGO endcap.

A problem that had to be resolved was the exclusion of periods when the TEC performance was poor. This becomes critical especially when studying the reaction $e^+e^- \rightarrow \gamma\gamma(\gamma)$ where Bhabha events, $e^+e^- \rightarrow e^+e^-(\gamma)$, constitute the main background which contaminates our data sample if both tracks would remain

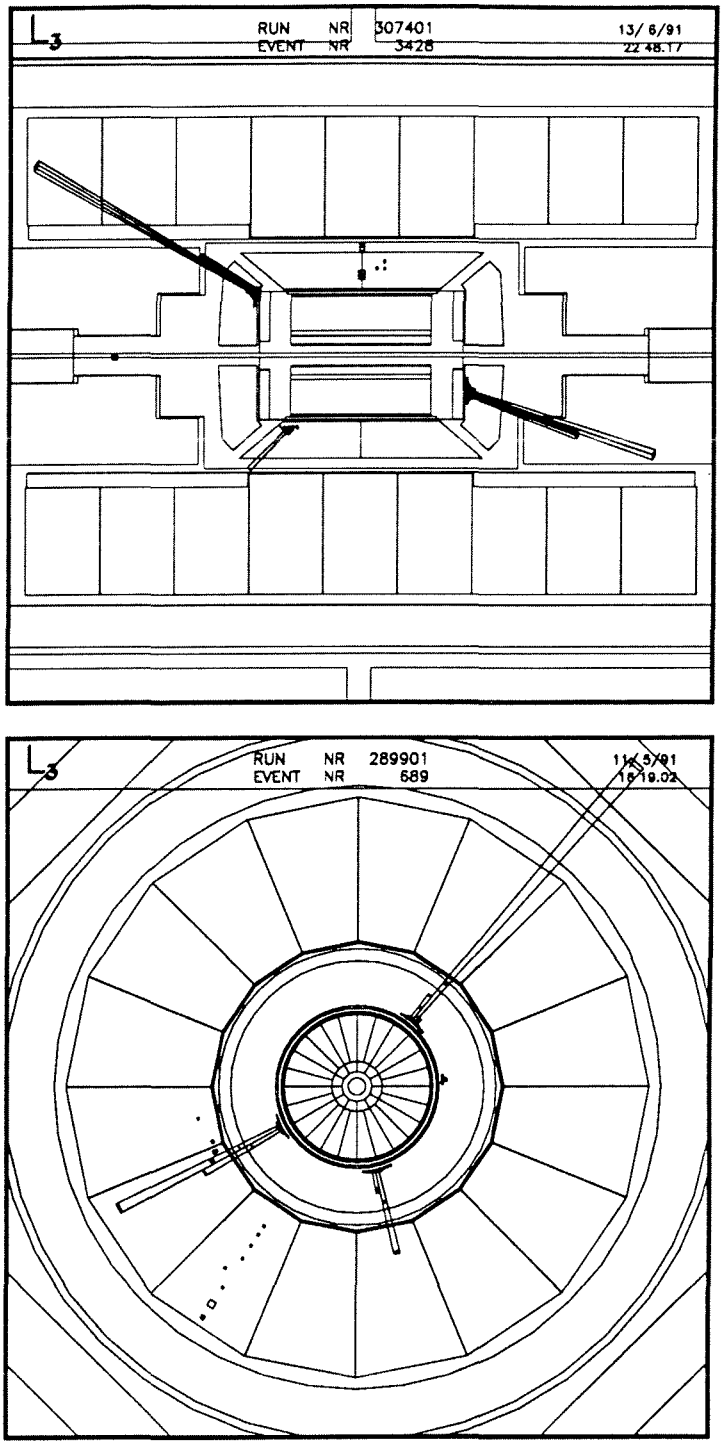

Figure 4.10: The top picture shows an $r-z$ view of three photon event with two of the photons detected with the BGO endcaps. The bottom picture shows an $r-\phi$ view of the only four photon event found in 1990 and 1991.

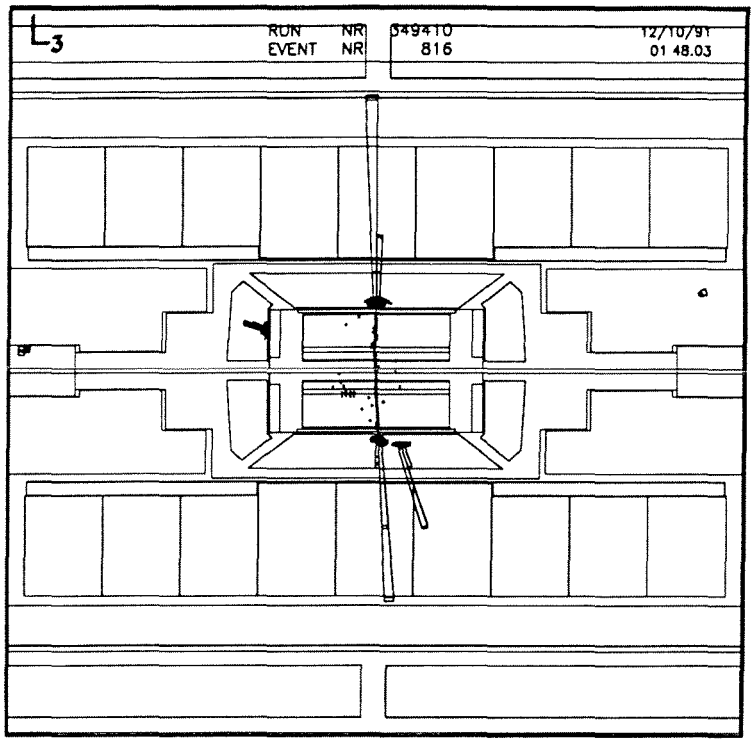

Figure 4.11: The $r-z$ view of a doubly radiative Bhabha event with one photon crossing the TEC endflange and the FTC before entering the BGO endcap.

undetected in the TEC and FTC. A few sectors of TEC or all of it can have low efficiency as a result of temporary hardware problems. For example during 1991 data taking period there were cases when the beam was not stable and a fraction of it entered the TEC detector. Many sectors received overcurrent and consequently tripped for self protection. The minimum time needed for the TEC high voltage to reach the nominal value again is about two minutes.

A method was developed to monitor the TEC performance offline and exclude periods with low efficiency to detect a charged particle. Hadronic events have a high track multiplicity and can be used to monitor TEC provided that their selection does not rely on TEC. When TEC is operating at nominal high voltage then for every hadronic event we observe on the average 17 tracks. Figure 4.12 shows the distribution of charge multiplicity in a hadronic event. If in a TEC sector there is a track found then we know that TEC was operating properly; if not then it could be either because of lack of statistics(there is not one track for every TEC

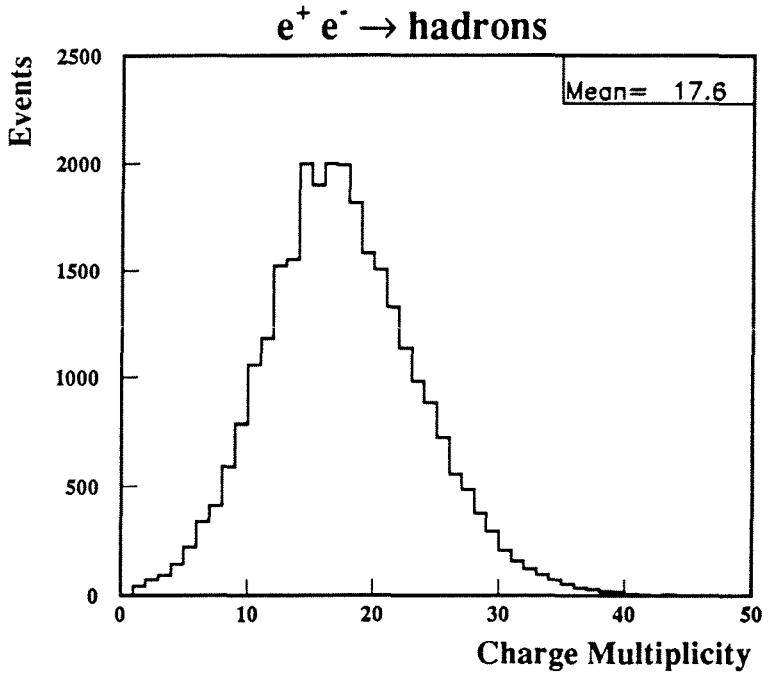

Figure 4.12: Charge multiplicity for hadronic events.

sector) or because TEC was not operating at nominal high voltage. The selection of hadronic events [28] relied solely on the calorimeters and the number of clusters in the event, therefore ensuring a selection unbiased from TEC.

The method to monitor TEC works as follows: Every year(1990,1991) is split in time units which are multiples of one minute intervals, starting at the beginning of the year. Inside every time unit we record all hadronic events and look for tracks. For each time unit a sector with at least one track is flagged as being operational. A table is made with this information including the run number, fill number and number of hadronic events in that time unit as well as the total number of hadronic events in the whole run that the time unit belongs to. From the bit pattern for all 24 outer and 12 inner sectors we can decide if a time unit should be excluded or not. If an interval is excluded then the luminosity must be corrected accordingly. For every center of mass energy bin we add up all hadronic events from the excluded intervals. This number is divided by the total number of hadronic events in the same center of mass energy bin and then the resulting

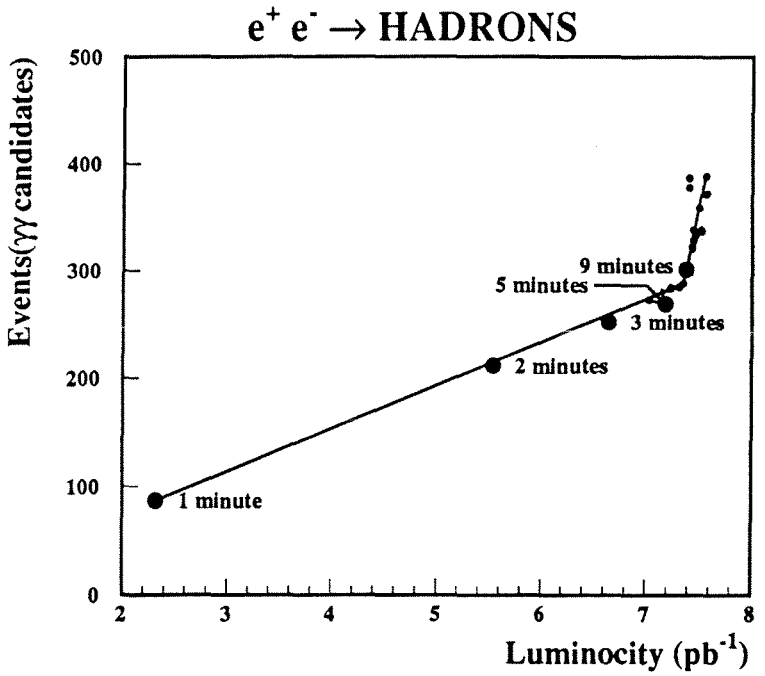

Figure 4.13: Number of two(three) photon events versus corrected luminosity.

factor is multiplied with the total luminosity for this center of mass energy bin. Thus we find how much is the excluded luminosity in an unbiased way. The final corrected luminosity for the center-of-mass energy bin i is:

$$\mathcal{L}_{i\,\text{Corrected}} = \mathcal{L}_{i\,\text{Total}} \left(1 - \frac{N_{\text{hadronic events excluded}}}{N_{\text{total hadronic events}}}\right)$$

For the two photon analysis we rejected all time units if any two sectors back to back were off. The reason for doing so is that if only one sector is not operational we can still reject a Bhabha event if the second track is detected.

It was mentioned that if a sector does not have a track it might just be a statistical effect. Therefore it is of importance to choose a time unit sort enough to be able to record accurately the TEC performance but not sorter than is needed because then we have inadequate number of hadronic events and time units with no problems would be excluded. The number of selected photon events is correlated to the length of the time unit but the ratio of number of events to the corrected

luminosity should be constant. When the time unit becomes bigger than the natural time scale needed to recover from a TEC trip then we start actually including bad intervals where the lack of tracks is not because of inadequate statistics but because of hardware problems. At this point the ratio of photon events to the luminosity increases because we start selecting Bhabha events as photon events. From Figure 4.13 we concluded that five minutes is the optimal time unit. We see that for time unit longer than 7 minutes the sample is clearly contaminated.

Chapter 5

Analysis

Study of the reaction $e^+e^- \rightarrow \gamma\gamma(\gamma)$.

5.1 Sample Purity

In 4.4(A) the final cuts for selecting events candidates of this reaction were given. The main background that could contaminate the event sample are Bhabha events when both tracks inside the TEC or the FTC remain undetected. Other sources of background have been eliminated with the selection cuts listed in 4.4(A). To be able to estimate the Bhabha contamination of the final sample we studied the TEC and FTC efficiency to detect a charged particle as a function of the polar angle θ(being measured with respect to the beam axis). All periods with problems in the performance of TEC or FTC were excluded(according to the scheme described in 4.4). The analysis was done with data collected during the 1990 and 1991 physics runs. In total we selected 418 events corresponding to $14.42pb^{-1}$ integrated luminosity. This is 75% of the total collected luminosity in the same period. From the total collected luminosity we excluded 18% because the corresponding time units failed the TEC high voltage test and 7% because one side of the FTC was not operational.

A track detection efficiency that is not flat in θ is assumed to be the result of limited acceptance and for that reason symmetric positions around $\theta = 90°$ are combined to yield higher statistics. The intrinsic efficiencies of TEC and FTC are

defined as follows:

ε_{TEC} = Probability to detect a charged particle inside TEC if there is one.

ε_{FTC} = Probability to detect a charged particle inside FTC if there is one.

In order to measure ε_{TEC} we selected Bhabha events inside TEC with one or both tracks detected. The selection criteria for a Bhabha event are the same as for a two photon event except that we require tracks matched with the BGO bumps(Figure 4.8). The cuts for selecting good quality tracks and the matching between tracks and BGO bumps was described in section 4.3(Figures 4.7 4.8). If only one track is present then that is a Bhabha event where the other track remained undetected. If in total there are N_{total} Bhabha and two photon events then apparently $N_{total} = N_{ee} + N_{\gamma\gamma}$ where N_{ee}, $N_{\gamma\gamma}$ is the number of Bhabhas and two photon events respectively. In terms of how many tracks were detected in the event we define N_0, N_1, N_2 as the number of events with no tracks, one track and two tracks detected respectively. Experimentally we measure N_{total}, N_0, N_1 and N_2. A last parameter that will be used is the noise level $\alpha = 0.03$ defined in 4.3. It must be included since noise may fake a track whether there was a charged particle that went through the detector or not. Then the following equations will yield the intrinsic track detection probability for TEC:

$$\begin{aligned} N_2 &= N_{ee}\varepsilon_{TEC}^2 + N_{\gamma\gamma}\alpha^2 \\ N_1 &= 2N_{ee}\varepsilon_{TEC}(1-\varepsilon_{TEC}) + 2N_{\gamma\gamma}\alpha(1-\alpha) \end{aligned}$$

The above equations are exact in considering the effect of noise. In fact when we write ε_{TEC}(or later ε_{FTC}) we really mean the probability to detect a charged particle including the possibility of a random detection because of noise. This means that if for some reason a charged particle is not 'seen' but the noise fakes a track we will still keep this track since there is no way of separating it from a real track. Of course we can always try to minimize noise and this is the reason for choosing a 3° opening angle when looking for TEC hits behind a BGO bump as was described in section 4.3. But the leftover noise will fake a real track and as a consequence the efficiency ε_{TEC} is an effective efficiency which includes the probability to truly detect a charged particle(because pulses were picked up by the TEC wires) and the probability not to detect the charged particle but nevertheless find a track because of noise.

$$\varepsilon_{TEC} = \varepsilon_{TEC\ true} + (1-\varepsilon_{TEC\ true})\alpha = \varepsilon_{TEC\ true} + \alpha - \varepsilon_{TEC\ true}\alpha$$

From the expressions for N_1, N_2 we get:

$$\left.\begin{array}{l} N_2 = N_{ee}\varepsilon_{TEC}^2 + (N_{total} - N_{ee})\alpha^2 \\ N_1 = 2N_{ee}(\varepsilon_{TEC} - \varepsilon_{TEC}^2) + 2(N_{total} - N_{ee})\alpha(1-\alpha) \end{array}\right\} \Longrightarrow$$

$$\left.\begin{array}{l} N_2 - N_{total}\alpha^2 = \varepsilon_{TEC}^2 - \alpha^2 \\ N_1 - 2N_{total}\alpha(1-\alpha) = 2\varepsilon_{TEC} - 2\varepsilon_{TEC}^2 - 2\alpha(1-\alpha) \end{array}\right\} \Longrightarrow \text{(divide by parts)}$$

$$\left.\begin{array}{l} 2\varepsilon_{TEC}A - 2\varepsilon_{TEC}^2 A - 2A\alpha(1-\alpha) = \varepsilon_{TEC}^2 - \alpha^2 \\ \text{with } A = \frac{N_2 - N_{total}\alpha^2}{N_1 - 2N_{total}\alpha(1-\alpha)} \end{array}\right\} \Longrightarrow$$

$$\left.\begin{array}{l} \varepsilon_{TEC}^2(1+2A) - 2\varepsilon_{TEC}A + 2A\alpha(1-\alpha) - \alpha^2 = 0 \end{array}\right\} \Longrightarrow$$

$$\varepsilon_{TEC} = \frac{A_2 \pm \sqrt{A_2^2 - 4A_1A_3}}{2A_1}$$

with $A_1 = 1 + 2A$, $A_2 = 2A$, $A_3 = 2A\alpha(1-\alpha) - \alpha^2$

The efficiency is therefore specified from the total number of Bhabhas and two photon events, the one track events, the two track events and the noise level. For every set of values for these parameters there is one and only one resulting TEC efficiency. The expression for ε_{TEC} above gives two solutions; one corresponds to the efficiency of TEC, and the second one just reproduces the noise level we input.

To estimate the error of the TEC detection efficiency we note that the noise level is only 3% and is introduced explicitly to the calculation only through the two photon events which are in any case an order of magnitude less than the Bhabha events. So for the error calculation of ε_{TEC} we can neglect α. If $\alpha \approx 0$ the expression for ε_{TEC} simplifies to: $\varepsilon_{TEC} = \frac{2N_2}{2N_2+N_1}$ The error on ε_{TEC} must take into account the variances of N_2, N_1. The problem however is that these numbers are highly correlated and the error propagation should include a term $2\partial^2\varepsilon_{TEC}/(\partial N_1 \partial N_2)\delta^2 N_{12}$ where δN_{12} is the off diagonal element of the covariance matrix for N_1, N_2. Rather than performing this error propagation we can calculate the error on ε_{TEC} in the following way. Assume that N_2 are successes from a total of $N = N_1 + N_2$ tries. The probability for a sucess is $p = N_2/N = N_2/(N_1+N_2)$. From binomial statistics we know that the variance on N_2 is:

$$\begin{aligned} \delta N_2 &= \sqrt{Np(1-p)} = \sqrt{N\frac{N_2}{N}\frac{N-N_2}{N}} \\ &= \sqrt{\frac{N_1N_2}{N}} \end{aligned}$$

Also the variance of p is just $\delta p = \frac{\delta N_2}{N}$ since we consider N as the fixed number of

total tries and we assign no error to it. Then

$$\begin{aligned} \delta p &= \sqrt{\frac{N_1 N_2}{N}} \frac{1}{N} \\ &= \frac{\sqrt{N_1 N_2}}{N^{3/2}} \end{aligned}$$

In a last step we observe that we can actually express ε_{TBC} as a function of p:

$$\begin{aligned} \varepsilon_{TBC} &= 2N_2/(2N_2 + N_1) = 2pN/(pN + N_2 + N_1) = 2pN/(pN + N) \Rightarrow \\ \varepsilon_{TBC} &= \frac{2p}{1+p} \end{aligned}$$

The error on ε_{TBC} as a function of δp is:

$$\delta\varepsilon_{TBC} = \frac{2\delta p}{(1+p)^2}$$

Figure 5.1(a) shows the TEC intrinsic efficiency as a function of $|\cos\theta|$. We observe that for $|\cos\theta| > 0.88$ the TEC intrinsic efficiency is no longer flat, but starts dropping rapidly. For $|\cos\theta| < 0.88$ the TEC intrinsic efficiency is $98\% \pm 0.3\%$

The same technic using one and two FTC track events could be used for the FTC as well but there is one complication. Photons that cross the TEC endflange may convert to an electron-positron pair that then enters FTC and leaves a track. In addition to this effect the outgoing photon may not convert inside the TEC endflange but after passing FTC it enters the BGO endcap and may cause showering electrons and positrons to be emitted backwards into the FTC. In this case a track is detected even though the initial photon did not convert. It would be wrong to include these tracks in the FTC efficiency calculation since they do not correspond to initial charged particles. We overcame this problem by using events that TEC detected two tracks within the FTC acceptance. The same selection cuts were used as for calculating the TEC efficiency, thus ensuring that only Bhabha events are used. In this way converted photons and electrons from backscattering are excluded from the FTC efficiency calculation.

In 4.3 we described how the FTC hits were used. The decision on whether the FTC detected a charged particle or not relied solely on the counting of the hits on each one of the X and Y planes. The calculation of ε_{FTC}, $\delta\varepsilon_{FTC}$ is done in exactly the same way as for TEC. The FTC intrinsic efficiency was found to be $99\% \pm 0.2\%$

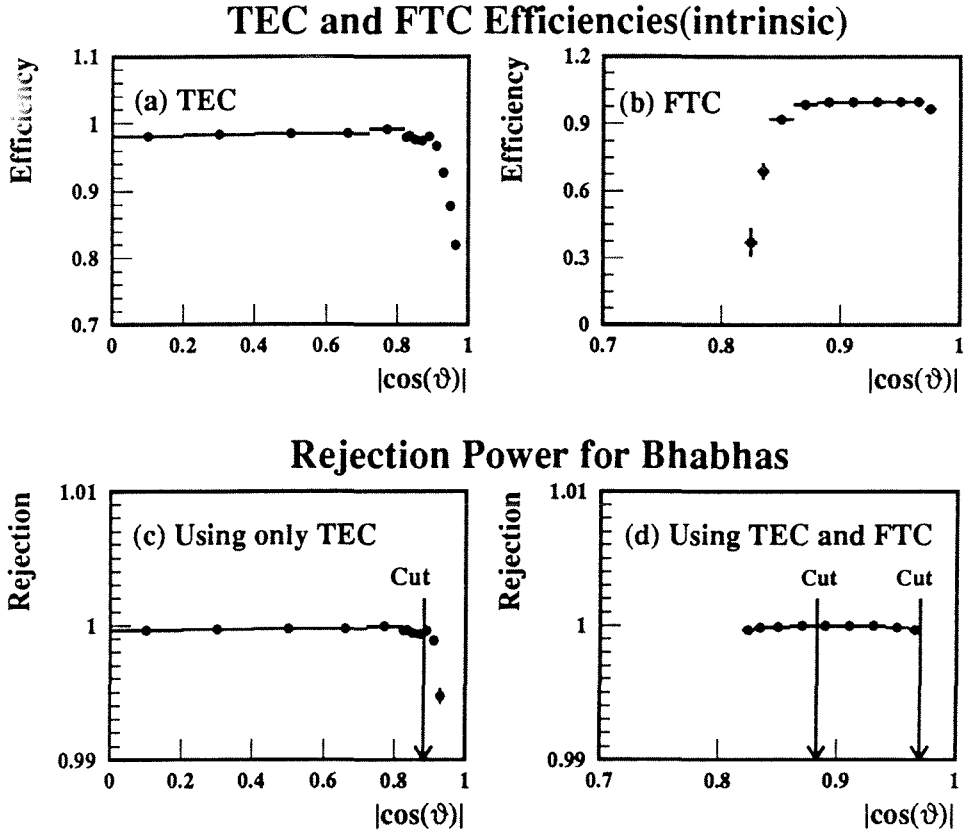

Figure 5.1: (a)TEC intrinsic efficiency as a function of cos(θ) (b)FTC intrinsic efficiency as a function of cos(θ) (c)TEC veto efficiency as a function of cos(θ) (d)Veto efficiency as a function of cos(θ) for the forward-backward region. For this region both TEC and FTC have been used.

in the region $0.88 < |\cos\theta| < 0.97$ Figure 5.1(b) shows the FTC intrinsic efficiency as a function of $\cos\theta$.

Veto efficiency(or rejection power) is the probability to reject a Bhabha event. This probability depends on ε_{TBC} and ε_{FTC}. In 4.4(A) we gave the TEC and FTC requirements to accept an event as a two photon event. If any TEC track is detected the event will be rejected. We define then the TEC veto efficiency as the probability to detect at least one of the two charged particles in a Bhabha event.

$$\varepsilon_{TBC\ veto} = 1-(1-\varepsilon_{TBC})^2 = \varepsilon_{TBC}(2-\varepsilon_{TBC})$$

Figure 5.1(c) shows $\varepsilon_{TBC\ veto}$ as a function of θ. We observe that for the angular range $|\cos\theta| < 0.883$ the TEC has a flat rejection power $99.96\% \pm 0.02\%$. For $|\cos\theta| > 0.883$ we have to use the FTC tracking information as well, namely still require no TEC tracks but also require at most one FTC track detected. The veto efficiency then is:

$$\begin{aligned}\varepsilon_{veto\ |\cos\theta|>0.883} &= 1-(1-\varepsilon_{TBC\ veto})(1-\varepsilon^2_{FTC}) \\ &= \varepsilon_{TBC\ veto}+\varepsilon^2_{FTC}-\varepsilon_{TBC\ veto}\varepsilon^2_{FTC}\end{aligned}$$

Figure 5.1(d) shows the veto efficiency in the forward-backward region when both TEC and FTC were used as described above. The veto efficiency is $99.98\% \pm 0.01\%$. From Figures 5.1(c) and (d) we see that the final range where the veto efficiency is flat is $|\cos\theta| < 0.970$ or $14^\circ < \theta < 166^\circ$. These limits define the acceptance for the analysis.

The above calculations assume that the electron and the positron in a Bhabha event are back to back and as a consequence the efficiency for detecting each of the charged particles is the same. One last case that must be examined is when the charged particles in a Bhabha event are not back to back. We may have for example a radiative Bhabha event with the electron in the barrel region of TEC and BGO and the positron in the BGO endcap behind the FTC. In such cases we have to rely on the TEC information solely since FTC is only used when both charged particles are within its acceptance. But clearly the TEC intrinsic efficiency drops after $|\cos\theta| > 0.883$(Figure 5.1(a)) and the veto efficiency must be calculated using the intrinsic efficiencies $\varepsilon_{TBC}(\theta_1)$ and $\varepsilon_{TBC}(\theta_2)$ which cannot be assumed to be the same. So for $|\cos\theta_1| < 0.883$ and $|\cos\theta_2| > 0.883$ or vise-versa the veto efficiency is:

$$\begin{aligned}\varepsilon_{veto\ |\cos\theta_1|<0.883\ \text{and}\ |\cos\theta_2|>0.883} &= \varepsilon_{veto\ |\cos\theta_2|<0.883\ \text{and}\ |\cos\theta_1|>0.883} \\ &= 1-(1-\varepsilon_{TBC}(\theta_1))(1-\varepsilon_{TBC}(\theta_2))\end{aligned}$$

Table 5.1 summarizes the different cases for $|\cos\theta_1|$ and $|\cos\theta_2|$ and lists the respective veto efficiency. Within our acceptance using the veto efficiencies for all

Range	Tracking Detectors used	Veto Efficiency.
$\|\cos\theta_1\| < 0.883$ $\|\cos\theta_2\| < 0.883$	TEC	$99.96\% \pm 0.02\%$
$\|\cos\theta_1\| > 0.883$ $\|\cos\theta_2\| > 0.883$	TEC and FTC	$99.98\% \pm 0.01\%$
$\|\cos\theta_1\| < 0.883$ $\|\cos\theta_2\| > 0.883$	TEC	$1-(1-\varepsilon_{TEC}(\theta_1))(1-\varepsilon_{TEC}(\theta_2))$

Table 5.1: The range of θ_1 and θ_2 and the corresponding veto efficiencies.

three possible cases we estimated that the contamination in Bhabha events is less than 10. This is 2.3% of the total number of two photon events that we selected. For the calculation of the cross-sections this contamination will be taken properly into account as is described in 5.4.

5.2 Photon conversions and electron backscattering

The probability for photon conversion in the TEC endflange or backscattering of electrons inside the BGO endcaps is of importance because it directly affects the efficiency for detecting photons. To measure this probability we selected all radiative Bhabha events with the two charged particles outside the FTC and the photon inside the FTC. The cuts for this selection were given in 4.4(C). In total 215 radiative Bhabha events were used.

Figure 5.2 shows the number of events(same as number of photons) populating every bin (N_x, N_y), where N_x, N_y is the number of FTC hits on the X, Y plane respectively. If N_x, $N_y < 2$ then we consider that the photon did not convert in

the TEC endflange and did not 'knock out' an electron in the BGO endcap. This is indicated with the hatched area on the same plot. From this plot we count up all photons that are not inside the hatched area and find 114 of them.

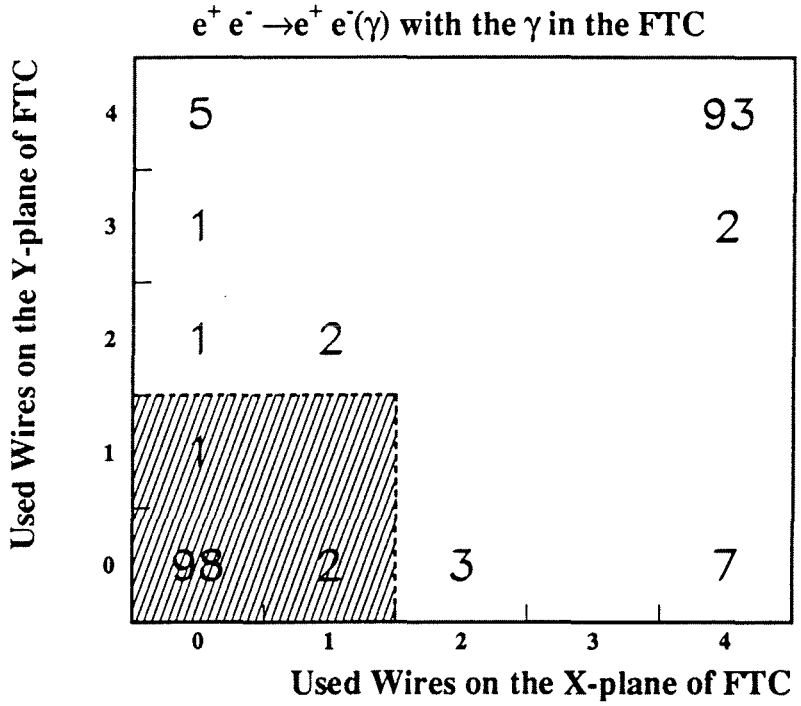

Figure 5.2: Number of FTC hits on the Y plane versus hits on the X plane. Every entry corresponds to a photon from a radiative Bhabha event. The events falling inside the hatched area correspond to photons that did not convert in the TEC endflange and did not cause back scattering of electrons in the BGO endcap.

Thus the conversion plus backscattering probability is:

$$p_{c+b} = \frac{\text{Number of photons with FTC track}}{\text{Total number of photons}} \equiv \frac{N_{c+b}}{N_{total}}$$
$$= \frac{114}{215} = 0.53$$

To find the error on this number we must use binomial statistics. The error on

N_{c+b} is:

$$\begin{aligned} \delta N_{c+b} &= \sqrt{N_{total}\, p_{c+b}(1-p_{c+b})} \\ &= \sqrt{215 \times 0.53 \times 0.47} = 7.3 \\ \delta p_{c+b} &= \frac{\delta N_{c+b}}{N_{total}} = 0.03 \end{aligned}$$

The final result is therefore $p_{c+b} = 53\% \pm 3\%$. Because of lack of statistics this probability was not derived as a function of θ but the dependence is expected to be statistically insignificant because the 14° that the FTC spans can only increase by 0.41cm the thickness of the 4.12cm Al TEC endflange. The Al has 8.9cm radiation length and the 4.12cm correspond to 37% conversion probability. The extra 0.41cm would add at most another 4.5% which is of the same magnitude as the statistical error.

The same measurement was done on QED Monte Carlo two photon events that went through detector simulation and reconstruction. We found $p_{c+B} = 38.2\% \pm 0.6\%$. This answer is certainly underestimating the effect since the conversion probability alone contributes at least 37% as shown in the last paragraph. The Monte Carlo value does not seem to take properly into account the cabling and additional to the TEC endflange material as well as the backscattering of electrons. We overcame the problem by overwriting the Monte Carlo value for p_{c+b} with the one measured experimentally.

5.3 Efficiency for selecting two photon events

The efficiency for selecting two photon events depends on the polar angles θ_1 and θ_2 of the photons. This dependence is understood since we combine information from three different detectors to select photons. In the next section the differential cross section with respect to one of the polar angles is measured but the efficiency used must be the probability to detect the whole event and involves both photons. If for example one of the photons is in a good region but the second photon is in the 'gap' between the barrel and endcap BGO then the whole event is excluded, not just the second photon. We define therefore a two dimensional efficiency $\varepsilon_{\gamma\gamma}(\theta_1, \theta_2)$ and divide the $|\cos\theta_1|, |\cos\theta_2|$ plane in six natural regions where the efficiency is calculated. These regions are defined by the angular ranges of the different subdetectors:

① $|\cos\theta_1| < 0.72$
$|\cos\theta_2| < 0.72$

Both photons are inside the barrel BGO. Bhabha events are rejected using the TEC.

② $0.82 < |\cos\theta_1| < 0.8829$ and $0.82 < |\cos\theta_2| < 0.8829$ or $0.82 < |\cos\theta_1| < 0.8829$ and $0.8829 < |\cos\theta_2| < 0.9703$ or

$0.8829 < |\cos\theta_1| < 0.9703$
$0.82 < |\cos\theta_2| < 0.8829$

Both photons are inside the BGO endcap but only one of them may be behind the FTC. Bhabha events are rejected using the TEC.

③ $0.8829 < |\cos\theta_1| < 0.9703$
$0.8829 < |\cos\theta_2| < 0.9703$

Both photons are inside the BGO endcap and also behind the FTC. Bhabha events are rejected using both the TEC and the FTC as described in 5.1.

④ $0.72 < |\cos\theta_1| < 0.82$ or $0.72 < |\cos\theta_2| < 0.82$

One or both photons are inside the 'gap' between the barrel and endcap BGO. All of these events are excluded.

⑤ $|\cos\theta_1| < 0.72$ and $0.82 < |\cos\theta_2| < 0.8829$ or $0.82 < |\cos\theta_1| < 0.8829$ and $|\cos\theta_2| < 0.72$

One of the photons is inside the barrel BGO and the other inside the endcap BGO but not behind the FTC. Bhabha events are rejected using TEC.

⑥ $|\cos\theta_1| < 0.72$ and $0.8829 < |\cos\theta_2| < 0.9703$ or $0.8829 < |\cos\theta_1| < 0.9703$ and $|\cos\theta_2| < 0.72$

One of the photons is inside the barrel BGO and the other inside the endcap BGO and behind the FTC. Bhabha events are rejected using TEC.

Most of the events fall into the first three categories. To calculate the efficiency in each region we used the QED Monte Carlo program described in Chapter 3. A table was constructed with every generated event being one entry according to the polar angles θ_1 and θ_2 of the two most energetic photons(Table 5.2(a)). Each event

belongs to one of the six regions listed above. Consequently the generated events went through detector simulation, reconstruction and the same selection cuts listed in 4.4(A). A non ideal detector was assumed and dead crystals were also taken into account. Table 5.2(b) contains all events that survived the selection cuts and the ratio with the previous one gives the efficiency for every one of the six regions. Note that in some bins in table 5.2(a) we have less entries than in 5.2(b). This is because after simulation and reconstruction the polar angles of the photons may change and the $(|\cos\theta_1|, |\cos\theta_2|)$ bins are repopulated. As a result we lose the initial information and we do not know exactly which photon went where. The efficiency measurement is statistical and gives the probability to detect a two photon event in a region including the possibility of this repopulation. The efficiencies for the six regions are:

$$\varepsilon_{\gamma\gamma\,①} = 90.9\% \pm 0.5\%$$

$$\varepsilon_{\gamma\gamma\,②} = 82.3\% \pm 1.0\%$$

$$\varepsilon_{\gamma\gamma\,③} = 62.7\% \pm 0.8\%$$

$$\varepsilon_{\gamma\gamma\,④} = 0.0\%$$

$$\varepsilon_{\gamma\gamma\,⑤} = 27.0\% \pm 3.6\%$$

$$\varepsilon_{\gamma\gamma\,⑥} = 4.4\% \pm 1.0\%$$

where the errors were calculated using binomial statistics: $\delta\varepsilon_{\gamma\gamma} = \sqrt{\frac{\varepsilon_{\gamma\gamma}(1-\varepsilon_{\gamma\gamma})}{N_{total}}}$, N_{total} being the total number of generated events in the angular range of interest. The above six efficiencies are valid for 1991 data when the BGO endcaps and the FTC were operational. For 1990 we used only barrel data and the efficiency is as in case one above with a small correction for the different number of dead crystals. We found $\varepsilon_{\gamma\gamma\,1990} = 90.2\% \pm 0.5\%$.

(a)

$\lvert\cos\theta_2\rvert$ \ $\lvert\cos\theta_1\rvert$	0 - 0.72	0.72 - 0.82	0.82 - 0.8829	0.8829 - 0.9703
0 - 0.72	① 2982	206	⑤ 140	⑥ 374
0.72 - 0.82	④ 0	941	133	132
0.82 - 0.8829	⑤ 12	1	② 948	256
0.8829 - 0.9703	⑥ 11	0	19	③ 3474

(b)

$\lvert\cos\theta_2\rvert$ \ $\lvert\cos\theta_1\rvert$	0 - 0.72	0.72 - 0.82	0.82 - 0.8829	0.8829 - 0.9703
0 - 0.72	① 2712	0	⑤ 40	⑥ 17
0.72 - 0.82	④ 0	0	0	0
0.82 - 0.8829	⑤ 1	0	② 732	210
0.8829 - 0.9703	⑥ 0	0	64	③ 2178

Table 5.2: (a) Number of generated events for the six different ($|\cos\theta_1|, |\cos\theta_2|$) bins. (b) Same as first part but the generated events were processed through detector simulation and reconstruction and subsequently went through the same set of cuts as real data. The ratio of the second table with the first one gives the efficiency for each region.

5.4 Cross-Section of the Reaction $e^+e^- \rightarrow \gamma\gamma(\gamma)$.

In this section we describe the measurement of the differential and total cross section. The calculation must take into account the contamination of the sample by Bhabha events (however small that might be). A second important issue is that any calculation should not depend on the assumption that we measure a QED process. In fact the reaction $e^+e^- \rightarrow \gamma\gamma(\gamma)$ is used to test QED and reveal new effects if QED breaks down at center-of-mass energies around 91GeV(i.e the mass of the Z^0 boson).

The cross section in some angular range is given by:

$$\begin{aligned} \sigma &= \frac{N_{\gamma\gamma}}{\varepsilon_{\gamma\gamma\ total}\,\mathcal{L}} \\ &= \frac{N_{\gamma\gamma\ selected} - N_{ee\ background}}{\varepsilon_{\gamma\gamma\ total}\,\mathcal{L}} \\ &= \frac{N_{\gamma\gamma\ selected} - N_{ee\ total}(1-\varepsilon_{veto})}{\varepsilon_{\gamma\gamma\ total}\,\mathcal{L}} \end{aligned} \tag{5.1}$$

but

$$\begin{aligned} N_{ee\ selected} &= N_{ee\ total}\,\varepsilon_{veto} \Longrightarrow \\ N_{ee\ total} &= \frac{N_{ee\ selected}}{\varepsilon_{veto}} \end{aligned}$$

and therefore

$$\sigma = \frac{N_{\gamma\gamma\ selected} - N_{ee\ selected}\dfrac{(1-\varepsilon_{veto})}{\varepsilon_{veto}}}{\varepsilon_{\gamma\gamma\ total}\,\mathcal{L}} \tag{5.2}$$

where $\mathcal{L}$ is the luminosity. Since σ is a total cross-section over some acceptance we must next find the exact value of $\varepsilon_{\gamma\gamma\ total}$ and ε_{veto}. In fact if the efficiency for detecting a two photon event is a function of θ_1, θ_2 then an assumption is necessary for the the event angular distribution in order to calculate the overall efficiency:

$$\varepsilon_{\gamma\gamma\ total} = \frac{\int_{\theta_1,\theta_2} \varepsilon_{\gamma\gamma}(\theta_1,\theta_2)\, N_{\gamma\gamma}(\theta_1,\theta_2)\, d\theta_1\, d\theta_2}{\int_{\theta_1,\theta_2} N_{\gamma\gamma}(\theta_1,\theta_2)\, d\theta_1\, d\theta_2}$$

Therefore if the assumption is made that the two photon events follow a QED distribution the overall efficiency can be found using the QED Monte Carlo. We point out however that another Monte Carlo(e.g. composite Z^0, excited electron

etc) would yield a different total efficiency. But the detection efficiency should not depend on some specific angular distribution or then a systematic error is introduced in the cross-section calculation. In addition to this there is another problem namely the fact that the veto efficiency is not exactly constant and in some cases it depends explicitly on θ_1, θ_2 as shown in Table 5.1.

These problems can be overcome by measuring the cross-section as follows:

$$\sigma = \sum_{i=1}^{N_{\gamma\gamma\ selected}} \frac{1}{\varepsilon^i_{\gamma\gamma}(\theta_1,\theta_2)\,\mathcal{L}} - \sum_{i=1}^{N_{ee\ selected}} \frac{(1-\varepsilon^i_{veto}(\theta_1,\theta_2))}{\varepsilon^i_{\gamma\gamma}(\theta_1,\theta_2)\varepsilon^i_{veto}(\theta_1,\theta_2)\,\mathcal{L}} \tag{5.3}$$

This equation directly comes from equation 5.2 but neither a total efficiency for selecting two photon events nor a constant veto efficiency is assumed. Every two photon selected event contributes to the cross-section according to the efficiency $\varepsilon^i_{\gamma\gamma}(\theta_1,\theta_2)$ of that particular event. In section 5.3 the efficiency was measured in six physical regions using the QED Monte Carlo program. However in each of these regions the efficiency is constant and therefore we do not bias ourselves to the specific model of QED. It is important to record the different efficiencies in the six regions because this is where the angular dependence comes in. When cross-sections are calculated every event falls in one of these six regions and rather than adding up all events and then dividing with a total efficiency we divide each event with one of those six efficiencies.

Every Bhabha selected event has a negative contribution to the cross section balancing the two photon selected events that are in reality Bhabha events. The veto efficiency is not assumed to be the same for all events but the correct value is used according to the polar angles in each case. The dependence of the veto efficiency on (θ_1, θ_2) is summarized in Table 5.1.

In the same spirit of measuring a cross-section in an unbiased way we conclude that we cannot extrapolate the cross-section to regions where there is no detector. In particular inside the 'gap' between the barrel and endcap BGO there is no data and we do not know what the efficiency would be if there was a detector there.

With this discussion we conclude that the measured cross-section has properly taken into account the background Bhabha events and is not biased from a model dependent total efficiency calculation.

Equation 5.3 gives the total cross section in an angular region. This cross-section can be normalized with respect to the polar angle of the first or the second photon and yields the differential cross section for that region.

$$\frac{d\sigma}{d\Omega_1} = \frac{\sigma}{2\pi \sin\bar{\theta}_1 d\bar{\theta}_1} \tag{5.4}$$

where $\bar{\theta_1}$ is the event-weighted average of the polar angle θ_1, i.e

$$\bar{\theta_1} = \sum_{i=1}^{N_{\gamma\gamma\ selected}} \theta_1^i \Big/ Number\ of\ events \tag{5.5}$$

From equation 5.1 the statistical error on the total and differential cross-section is:

$$\frac{\delta\sigma}{\sigma} = \frac{1}{\sqrt{N_{\gamma\gamma}}} \tag{5.6}$$

During 1990 and 1991 physics runs we collected data at seven center-of-mass energies. The integrated luminosity for the different center-of-mass energies is given in Table 5.3. This table also shows the number of events for the 1990 and 1991 data runs and the total measured cross sections. The QED predicted values were found using the Monte Carlo program described in Chapter 3. From the generated events the total and differential QED cross-sections were calculated. For the total QED cross section the region $0.72 < |\cos\theta| < 0.82$ corresponding to the 'gap' between the barrel and endcap BGO was excluded since this region is also missing from the data.

For the differential cross-section the barrel region was split in six bins, the endcap region before the FTC in one bin and the endcap region with FTC in two bins. In Table 5.4 the measured differential cross sections with respect to the most energetic photon and the prediction from QED is given.

The QED differential cross-section to $O(\alpha^3)$ was parameterized to an analytical formula. Initially from every differential cross-section value predicted according to QED(Table 5.4) the zero order differential cross-section as given by equation 1.2 is being subtracted. This yields the radiative corrections to $O(\alpha^3)$ for the nine $|\cos\theta|$ bins in Table 5.4. To these nine points the following function is fitted:

$$\left(\frac{d\sigma}{d\Omega}\right)_{QED\ radiative\ corrections} = A + B\frac{(1+\cos^2\theta)}{(1-\cos^2\theta)} \tag{5.7}$$

From the fit it is found that $A = -0.66 \pm 0.04$ and $B = 0.44 \pm 0.02$. Figure 5.3 shows the radiative corrections as a function of $|\cos\theta|$ for the nine $|\cos\theta|$ bins listed in Table 5.4 and superimposed is the result from the fit. We note that the radiative corrections have a negative contribution to the cross-section at low values of $\cos\theta$. At about $|\cos\theta| = 0.462$ radiative corrections become positive and increase the cross-section. This behaviour is understood in the context of what was said in Chapter 3. Virtual corrections and soft bremsstrahlung have a negative

(a)

$\sqrt{s}$ (GeV)	$\mathcal{L}_{int}$ 1991 (pb^{-1})	$N_{\gamma\gamma(\gamma)}$ (1991)	σ_{meas} (pb) (1991)	σ_{QED} (pb)
88.5	0.20	2	15.2 ± 10.7	51.4
89.4	0.59	15	34.4 ± 8.9	50.3
90.3	0.47	24	63.6 ± 13.0	49.4
91.2	7.52	269	46.9 ± 2.9	48.4
92.0	0.38	10	32.0 ± 10.1	47.5
93.0	0.72	24	41.6 ± 8.5	46.6
93.7	0.53	14	35.1 ± 9.4	45.9

(b)

$\sqrt{s}$ (GeV)	$\mathcal{L}_{int}$ 1990 (pb^{-1})	$N_{\gamma\gamma(\gamma)}$ (1990)	σ_{meas} (pb) (1990)	σ_{QED} (pb)
89.8	0.53	5	10.5 ± 4.7	18.1
91.2	2.59	43	18.4 ± 2.8	17.6
92.6	0.89	12	14.9 ± 4.3	17.0

Table 5.3: (a) The integrated luminosity as a function of the center-of-mass energies for the 1991 data ($14° < \theta < 166°$). Also given are the number of events observed, the total measured cross sections and the QED prediction to $O(\alpha^3)$. Data were not collected inside the 'gap' between the barrel and endcap BGO and so from the QED prediction this region is excluded as well. (b) The same table for the 1990 data ($44° < \theta < 136°$). The first and last three energy bins have been combined.

$\lvert\cos\theta_1\rvert$	$N_{\gamma\gamma(\gamma)}$ (1990+1991)	$\left(\frac{d\sigma_{meas}}{d\Omega_{\gamma\gamma(\gamma)}}\right)$ (pb/sr) (1990+1991)	$\left(\frac{d\sigma_{QED}}{d\Omega_{\gamma\gamma(\gamma)}}\right)$ (pb/sr)
0.062	13	1.8 ± 0.5	2.1
0.173	23	3.3 ± 0.7	2.6
0.290	25	3.5 ± 0.7	2.9
0.433	18	2.6 ± 0.6	3.7
0.551	29	4.1 ± 0.8	4.6
0.659	48	6.8 ± 1.0	6.7
0.855	44	19.6 ± 3.0	18.2
0.905	37	27.0 ± 4.4	29.0
0.951	75	56.3 ± 6.5	59.8

Table 5.4: Differential cross sections for nine $|\cos\theta|$ bins at the center-of-mass energy 91.2 GeV. The $|\cos\theta|$ values given in the first column are event-weighted averages(equation 5.5); the second column gives the number of events and the last column the QED prediction to $O(\alpha^3)$. Data from 1990 ($44° < \theta < 136°$) and 1991 ($14° < \theta < 166°$) have been combined.

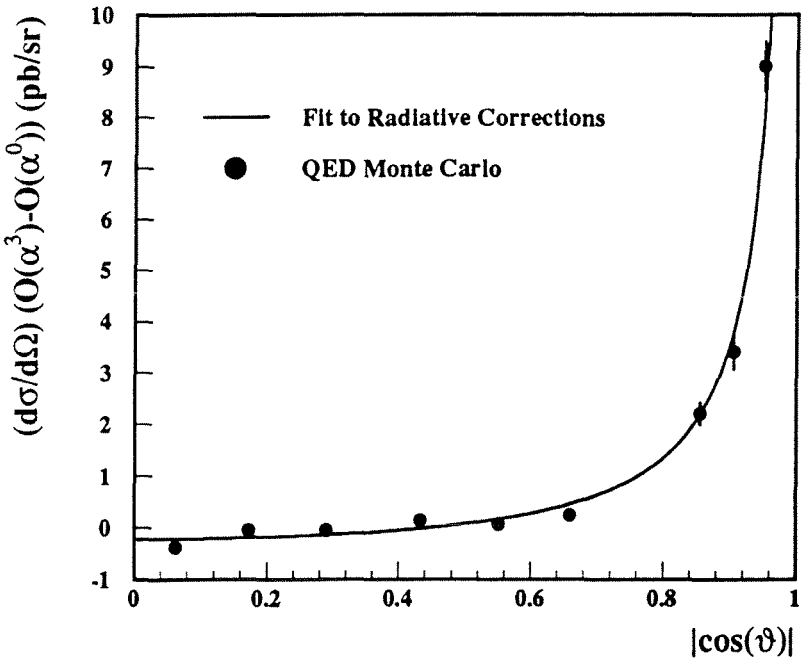

Figure 5.3: Radiative corrections as a function of $|\cos\theta|$. Points correspond to the QED Monte Carlo and the solid line is the fitted analytical formula.

effect on the cross-section while hard bremsstrahlung radiation has a positive effect and becomes most important in the forward-backward direction.

Next the formula for the radiative corrections is added to equation 1.2 and this yields the analytical expression for the total QED differential cross-section to $O(\alpha^3)$ at center-of-mass energy 91.2 GeV:

$$\left(\frac{d\sigma}{d\Omega}\right)_{QED\ to\ O(\alpha^3)} = -0.66 + 2.9329\left(\frac{1+\cos^2\theta}{\sin^2\theta}\right) \tag{5.8}$$

We arrive at the last expression substituting $\alpha = 1/137.0359$ and $s = 91.2^2 \mathrm{Gev}^2$ in equation 1.2. As a test the analytic expression for the differential cross-section was integrated from $|\cos\theta| = 0$ to $|\cos\theta| = 0.9703$ and the resulting total cross-section was found to be 55.39 pb as compared to 55.27 pb predicted numerically from the QED Monte Carlo. Figure 5.4 shows the data points compared to the zero-

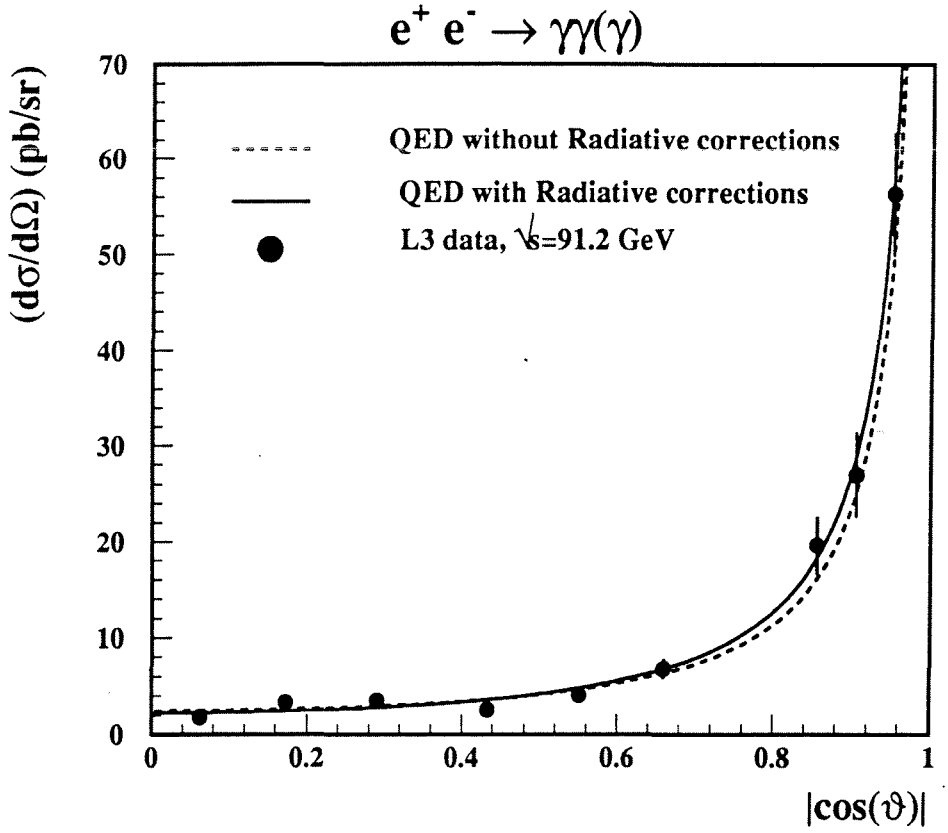

Figure 5.4: The measured differential cross section at center-of-mass energy 91.2 GeV. Data have been combined from 1990 and 1991 in the barrel region. The dashed line curve shows the zero order QED cross-section and the solid line curve is the QED cross section to $O(\alpha^3)$.

order(equation 1.2) and to the radiatively corrected QED prediction(equation 5.8).

The χ^2 of the data points compared to the QED expectation is defined as:

$$\chi^2 \equiv \sum_{i=1}^{9} \left(\frac{(d\sigma/d\Omega)^i_{measured} - (d\sigma/d\Omega)^i_{QED\ O(\alpha^3)}}{\sigma^i_{QED}} \right)^2 \tag{5.9}$$

The summation is over the nine bins in $|\cos\theta|$. For every bin the theoretical uncertainty σ^i_{QED}, is determined from the theoretical value of the differential cross-section and the luminosity available in the data:

$$\begin{aligned} \sigma^i_{QED} &= \frac{(d\sigma/d\Omega)^i_{QED\ O(\alpha^3)}}{\sqrt{N^i_{QED\ \gamma\gamma(\gamma)}}} \\ &= \frac{(d\sigma/d\Omega)^i_{QED\ O(\alpha^3)}}{\sqrt{\mathcal{L}^i_{data}\sigma^i_{QED}}} \end{aligned}$$

The χ^2 is 6.5 for the 9 degrees of freedom, indicating that the measured differential cross-section is in good agreement with the QED prediction.

5.5 Search for an Excited Electron

As was discussed in section 1.4.1 a virtual excited electron would enhance the two photon cross-section and change the angular distribution. Similarly the related QED cutoff parameters Λ_+ and Λ_- alter the angular distribution of the photons in the final state and change the absolute production rate as well. This means that a QED breakdown may be revealed with a combined study of the absolute production rate and the angular distribution as compared to the prediction from QED with these effects folded in. We used the unbinned maximum likelihood method to search for these new non QED effects. Every event is assigned a probability according to its polar angle. This probability is constructed from the differential cross-section that has folded in the QED and the breakdown effects. The probabilities of all events are multiplied together and this is the probability of the data sample corresponding to the parent distribution that is used to describe the data. The absolute number of produced two photon events must be taken into account as a separate multiplicative term in the likelihood. The distribution of the likelihood, which is the total probability of the data sample, as a function of the parameters that determine the parent distribution is used to either reveal the new physics or to set a limit on the QED cutoff parameters and the mass of an excited electron.

5.5.1 Construction of the Probability Density Function

If $\sigma(\theta)_M$ is the measured differential cross-section then it is related to the theoretical prediction through equation 1.10. The right hand side of this equation describes the model with respect to which the data are compared. We remind that in the notation used here $\sigma(\theta)_M$ stands for $\frac{d\sigma_M}{d\Omega}$. Similarly when we write from now on $P(\theta)$ we mean the differential probability density $\frac{dP}{d\Omega}$. This probability $P(\theta)$ to observe an event at polar angle θ is derived from the theoretical differential cross-section when it is properly normalized over all the solid angle that data were collected.

$$P(\theta) = \frac{\sigma(\theta)^{O(\alpha^3)}_{QED}\left(1 + \delta_{new}(\theta)\right)\varepsilon(\theta)}{\int \sigma(\theta')^{O(\alpha^3)}_{QED}\left(1 + \delta_{new}(\theta')\right)\varepsilon(\theta')\,d\Omega'} \tag{5.10}$$

where $\varepsilon(\theta)$ is the efficiency for selecting two photon events. This efficiency can be folded in the QED differential cross-section and the above equation is written:

$$P(\theta) = \frac{\sigma'(\theta)^{O(\alpha^3)}_{QED}\left(1 + \delta_{new}(\theta)\right)}{\int \sigma'(\theta')^{O(\alpha^3)}_{QED}\left(1 + \delta_{new}(\theta')\right)\,d\Omega'} \tag{5.11}$$

with $\sigma'(\theta)^{O(\alpha^3)}_{QED} = \sigma(\theta)^{O(\alpha^3)}_{QED}\,\varepsilon(\theta)$.

The advantage in folding the efficiency in the QED cross-section is that this can be done implicitly using the QED Monte Carlo. The functional form of $\varepsilon(\theta)$ is not needed to be known and in fact the efficiency is this analysis is found in six distinct regions (section 5.3) and not as a continuous function. We included the efficiency in the QED cross-section as follows:
The QED generated events go through detector simulation and reconstruction and consequently through the selection cuts. Events that pass those cuts provide a differential cross-section from which we subtract the Born level QED differential cross-section as given by equation 1.2. This is exactly the same procedure that led to the analytical formula for the QED differential cross-section in section 5.4. The only difference is that while in section 5.4 the Born level cross-section was subtracted from the $O(\alpha^3)$ QED cross-section to yield the radiative corrections now it is subtracted from the $O(\alpha^3)$ QED cross-section after the generated events have suffered losses through detector simulation, event reconstruction and event selection. This way we obtain effective radiative corrections which have the efficiency folded in. A fit is done to these effective radiative corrections. The result of the

fit is added back to the Born level cross-section and this is the final QED $O(\alpha^3)$ differential cross-section with the efficiency folded in. With the above procedure we found that:

(5.12)

$$\sigma'(\theta)^{O(\alpha^3)}_{QED} = \sigma(\theta)^{O(\alpha^3)}_{QED}\,\varepsilon(\theta) = \\ -0.235 - 1.2\,\frac{|\cos\theta|^{7.1}}{1-|\cos\theta|} + 2.4929\left(\frac{1+\cos^2\theta}{\sin^2\theta}\right)$$

for center-of-mass energy 91.3 GeV.

The expression for $\sigma'(\theta)^{O(\alpha^3)}_{QED}$ is substituted in the equation 5.11 for the probability along with the expressions for $(1 + \delta_{new}(\theta))$ as given by equations 1.3, 1.4

The denominator in equation 5.11 is the normalization necessary to convert the differential cross-section into probability density. The integration must be done over all solid angle that data were collected. For the 1990 physics run that was defined by $|\cos\theta| < 0.72$ and in 1991 by $|\cos\theta| < 0.9703$. However in 1991 we must take into account the 'gap' between the barrel and endcap BGO. Since no data were collected, this angular range must be excluded from the integration to correctly normalize the probability density. This concludes the discussion on the probability density for every event. Physically this probability expresses how likely it is to observe an event at some polar angle θ assuming some underlying physics distribution. In practise the probability is found as a function of the polar angle of one of the photons. This analysis used without loss of generality the angle of the most energetic photon.

Figure 5.5 shows the probability density for observing two photon events, as a function of $|\cos\theta|$, for two cases when $\Lambda_+ = 60$ GeV and 200 Gev. As mentioned already this probability density is defined for 1991 in the region $|\cos\theta| < 0.9703$. For the 'gap', where no data were collected, the probability is zero. The probability density for low Λ_+ values is more flat and with enhanced photon production in the barrel region. At the limit that Λ_+, Λ_-, $m_{e^*} \to \infty$ the pure QED result is recovered as can be seen from equations 1.3,1.4. Therefore the solid line curve in Figure 5.5 deviates more from the QED prediction while the dashed line curve approaches it.

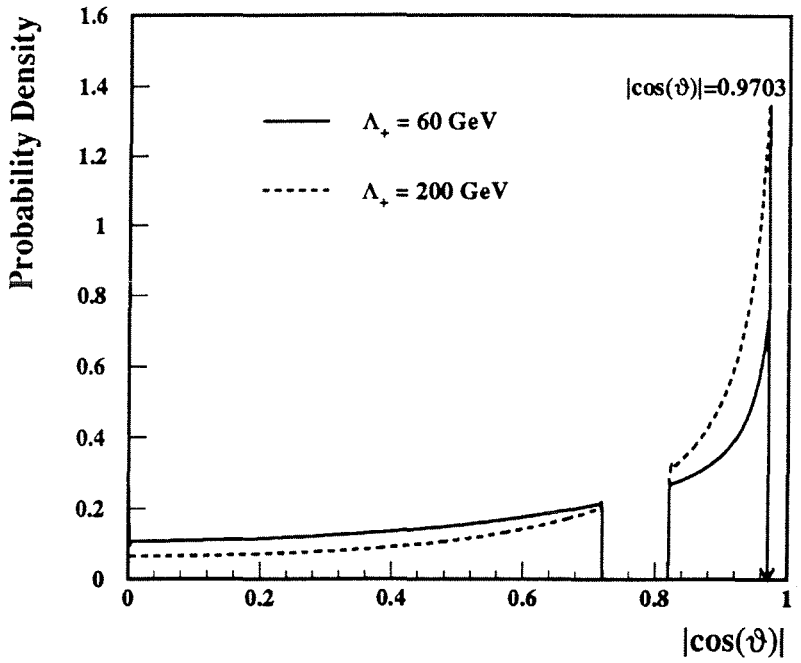

Figure 5.5: The probability density as a function of $\cos(\theta)$ for two different Λ_+ values. The probability is normalized to unity when integrated over the solid angle, which means integrating over $\cos(\theta)$ and multiplying by 2π.

5.5.2 The Likelihood function

The following likelihood function was used:

$$L = \overbrace{\frac{1}{\sqrt{2\pi\sigma^2}} \exp\left(\frac{-(N_{obs} - N(Par))^2}{2\sigma^2}\right)}^{\text{Probability for observing } N_{obs} \text{ events}} \overbrace{\prod_{i=1}^{N_{obs}} P(\theta_i, Par)}^{\text{Probability for this configuration}} \tag{5.13}$$

where Par is the parameter under consideration(Λ_+, Λ_-, m_{e^*}), N_{obs} is the observed number of events, $N(Par)$ is the expected number of events, σ is the uncertainty on the number of expected events and $P(\theta_i, Par)$ is the event probability density, discussed in the previous section, that depends on the parameter Par and on $|\cos\theta_i|$; θ_i being the polar angle of the most energetic photon in the event.

The probability density $P(\theta_i, Par)$ depends on the center-of-mass energy as well. We used an event averaged center-of-mass energy $\sqrt{s} = 91.3$ GeV since lack of statistics does not allow us to perform the analysis on every center-of-mass energy bin separately. Equation 5.12 provides the QED contribution to the cross-section with efficiencies folded in and was derived for this center-of-mass energy.

The first term in equation 5.13 imposes an explicit constraint that the total number of predicted events must within errors agree with the total number of observed events. It is the Gaussian probability to observe N_{obs} events when we expect $N(Par)$. The error σ on the number of expected events includes in quadrature the statistical error and an overestimated systematic error of 3%. The statistical error on the theoretical number of events comes from considering how many events one expects with the luminosity available in the data and the theoretical cross-section that incorporates the QED prediction and the contribution from the breakdown effects. The total error σ is then:

$$\sigma = \sqrt{\sigma^2_{stat\ theory} + \sigma^2_{systematic}} = \sqrt{(\mathcal{L}_{data}\sigma_{QED+new})^2 + 0.03^2}$$

where $\sigma_{QED+new}$ is the total theoretical cross-section inside our acceptance.

The second term in equation 5.13 is the product of all probability densities, one per event, that imposes the constraint on the shape of the angular distribution of the two photon events. The probability density for Λ_+ and Λ_- is given from equation 5.11 with δ_{new} given by 1.3. To fit the mass of the excited electron we used the full expression for the differential cross section given by equation 1.4, assuming the relative coupling constant $\lambda = 1$.

In 1990 the data were limited in the barrel region and as a consequence the integration in equation 5.11 for 1990 data is done over a different angular range than in 1991. This leads to two probability densities for every parameter, one for 1990 data and one for 1991 and therefore there are two likelihood functions. The aim is however to combine both data samples and increase statistics. This is achieved by multiplying the likelihood functions together to form a single function.

$$L_{1990+1991}(Par) = L_{1990}(Par) \times L_{1991}(Par) \tag{5.14}$$

where Par denotes one of the three parameters Λ_+, Λ_- or m_{e^*}.

5.5.3 Results on the search for an Excited Electron

If $L(\alpha)$ is a likelihood function depending on the parameter α then the best estimate for α is found by varying the parameter until $L(\alpha)$ maximizes. The maximum

likelihood principle relies on the sensible assumption that when the parameter of a model we are testing approaches its true value then the probability of the data sample maximizes. That is because the probability depends on the parameter and describes the agreement between data and the model we are assuming. In the limit of a large number of measurements the likelihood will be a Gaussian as a consequence of the central limit theorem:

$$L(\alpha) = \frac{1}{\sigma\sqrt{2\pi}} \exp -(\alpha - \hat{\alpha})^2/2\sigma^2 \tag{5.15}$$

The best estimate for α is $\alpha = \hat{\alpha} \pm \sigma$. In many cases it is more convenient to take the log of the likelihood function because the likelihood being a probability may have very small values:

$$\log L(\alpha) = \log \frac{1}{\sigma\sqrt{2\pi}} - (\alpha - \hat{\alpha})^2/2\sigma^2 \tag{5.16}$$

The logarithm of a Gaussian is a parabola and when the likelihood maximizes so does the logarithm and therefore the same solution for α yields. The error calculation has also a simple correspondence between the likelihood L and the $\log L$. The one standard deviation in the likelihood corresponds to moving 0.5 units down from the peak in the $\log L$ curve and the two standard deviations correspond to 2 units. For example the 2σ difference of α from $\hat{\alpha}$ in L, which is a 95.45% Confidence Level, becomes in $\log L$:

(5.17)

$$\log L(\hat{\alpha} + 2\sigma) - \log L(\hat{\alpha}) =$$

$$\log \left(\frac{1}{\sigma\sqrt{2\pi}} \exp -(\hat{\alpha} + 2\sigma - \hat{\alpha})^2/2\sigma^2 \right) - \log \left(\frac{1}{\sigma\sqrt{2\pi}} \exp -(\hat{\alpha} - \hat{\alpha})^2/2\sigma^2 \right)$$

$$= \log \frac{1}{\sigma\sqrt{2\pi}} - \log \frac{1}{\sigma\sqrt{2\pi}} - 2 = -2$$

The advantage using the $\log L$ is that we can find the mean value and perform the error calculation graphically. One plots the $\log L$(or the negative of that since L is less than one and $\log L$ is negative) as a function of the parameter. The best estimate for the parameter is $\hat{\alpha}$ which maximizes $\log L$ or equivalently minimizes $-\log L$. We then move two units away from the maximum(minimum) value of $\log L$ ($-\log L$) and find the corresponding values for the parameter, α_r, α_l. Then at 95.45% CL the solution is $\alpha = \hat{\alpha}^{+\alpha_r}_{-\alpha_l}$. These arguments are demonstrated in Figure 5.6 for an arbitrary Gaussian probability function.

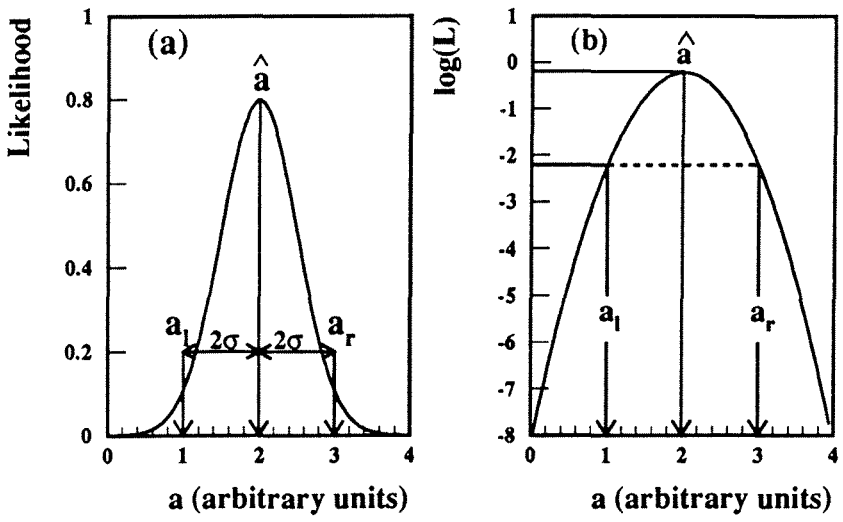

Figure 5.6: (a) A Gaussian Likelihood as a function of the parameter it depends on. (b) The logarithm of the Likelihood as a function of the parameter.

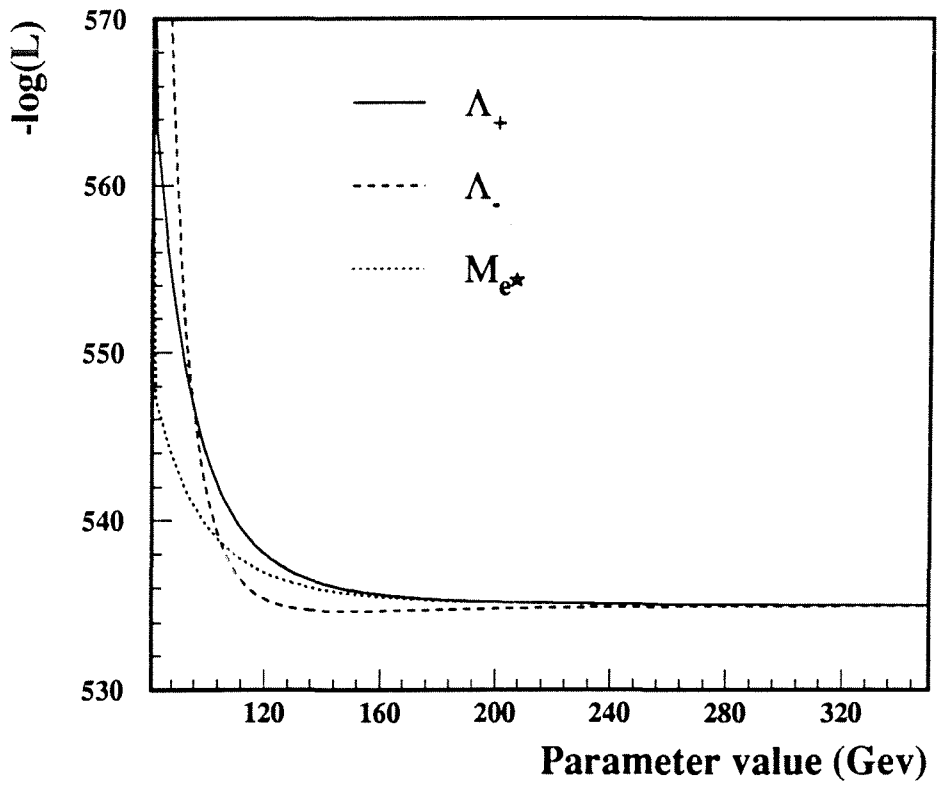

Figure 5.7: The negative log likelihood as a function of the parameter value in Gev. Data from 1990 and 1991 have been combined.

Figure 5.7 shows the $-\log L$ as a function of the parameter value in Gev for the data. The three curves correspond to Λ_+, Λ_-, m_{e^*} which we want to determine. We notice that the $-\log L$ drops as the parameters increase and asymptotically reaches a stable value. This behaviour of the likelihood is consistent with the statement that the true values for Λ_+, Λ_-, m_{e^*} tend to infinity which means that there is agreement of QED with the data sample. The first conclusion is therefore that within statistics a QED breakdown is not observed. Next we aim in setting limits at 95% confidence level for Λ_+, Λ_-, and m_{e^*}. The complication is that the $-\log L$ is not a parabola as is seen from Figure 5.7. A way to go around this would be to go back to the likelihood itself and integrate it with respect to Λ_+, Λ_- and m_{e^*}. For example when:

$$\int_{\Lambda_+^{min}}^{\infty} L(\Lambda_+)d\Lambda_+ = 0.95$$

then at 95% CL, Λ_+ must be more than Λ_+^{min}. The same could be done with the other two parameters if it were not for the fact that the actual likelihood is not bounded, but rather reaches asymptotically a steady value and the integral $\int_0^{\infty} L(\Lambda_+)d\Lambda_+$ cannot be normalized to unity.

We go a step backwards and reconsider equation 5.15. In the case where all values of $\alpha < \hat{\alpha}$ are unphysical the likelihood is a half gaussian and the logarithm of it is a half parabola. The best estimate of α cannot be found but a one sided limit can be set along the lines that followed equation 5.16. At 95.45% CL the parameter is less than α_r which translates in moving away from the maximum(or minimum) value of the $\log L$ $(-\log L)$ by two. As long as the maximum value of the Gaussian is in the physical region we can keep the correspondence of 2σ with the two units in the parabola. In our analysis all of the three parameters Λ_+, Λ_-, m_{e^*} have to be greater than zero to be physical,which equivalently means that $\hat{\alpha} \geq 0$. Still our problem is not solved because the $-\log L$ of Figure 5.7 is not a one sided parabola, because the likelihood as a function of the parameters is not a one sided Gaussian. We may however think of a transformation of the original parameters to new ones such that the likelihood is a one sided Gaussian satisfying the condition $\widehat{\alpha'} \geq 0$ with $\alpha' = \phi(\alpha)$ for each of the parameters. Then the logarithm is a one sided parabola and the limit for α' can be set as described. Let for example α'_r be the 95.45% CL limit on the transformed parameter α'. We then transform back and obtain $\alpha_r = \phi^{-1}(\alpha'_r)$ which is the 95.45% CL limit on the original parameter and which is the same with the value we get for α if on the original plot for $-\log L(\alpha)(\alpha$ being Λ_+, Λ_-, or $m_{e^*})$ we move away from the minimum by two units. The final conclusion is therefore that we only need to prove

that such a transformation $\phi(\alpha)$ exists that makes the likelihood at least a one sided Gaussian satisfying the condition $\widehat{\alpha'} \geq 0$. If this is true then it is legitimate to quote that at 95.45% CL the limits for Λ_+, Λ_- and m_{e^*} are obtained by moving up two units from the minimum asymptotic value of $-\log L(\Lambda_+)$, $-\log L(\Lambda_-)$ and $-\log L(m_{e^*})$.

We demonstrate this and derive the limits with Figures 5.8, 5.9 5.10, 5.11. From Figure 5.8 it is seen that the $-\log L$ for Λ_+ and m_{e^*} has a common

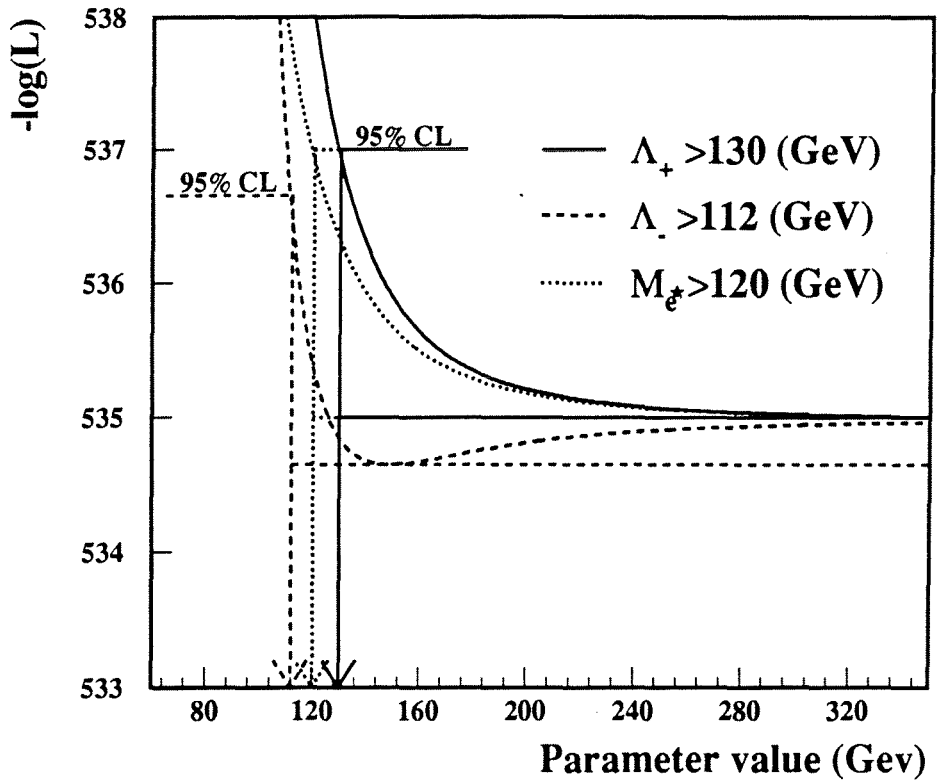

Figure 5.8: The negative logarithm of the likelihood as a function of the parameter value in GeV. Limits at 95% CL are set for Λ_+, Λ_- and m_{e^*} when we move up from the minimum value of the negative log likelihood by two units.

asymptotic minimum. Moving up from that minimum by two units yields at 95.45% CL that $\Lambda_+ > 130$ GeV and $m_{e^*} > 120$ GeV. The third parameter has

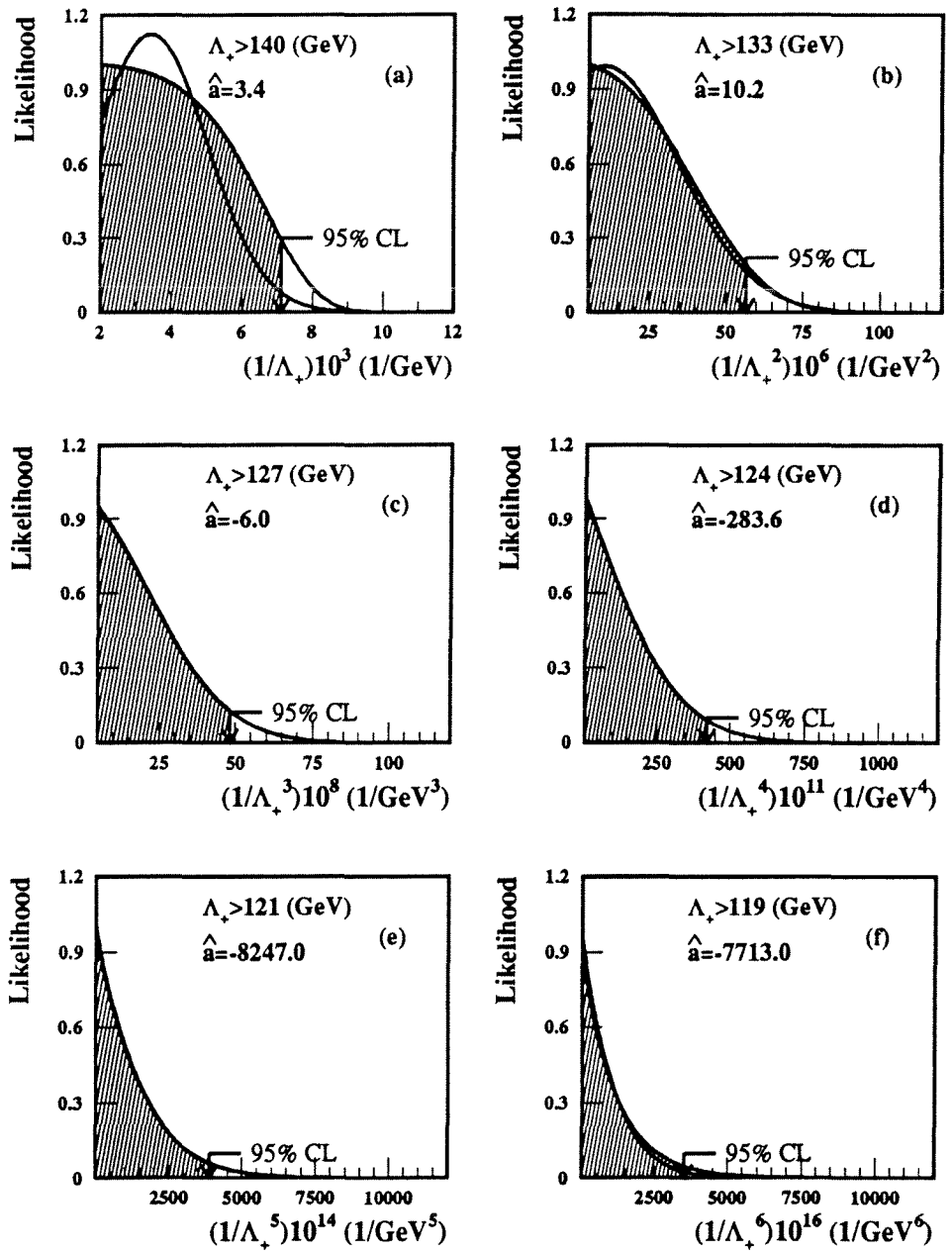

Figure 5.9: The likelihood as a function of the inverse of Λ_+ exponentiated to different powers.

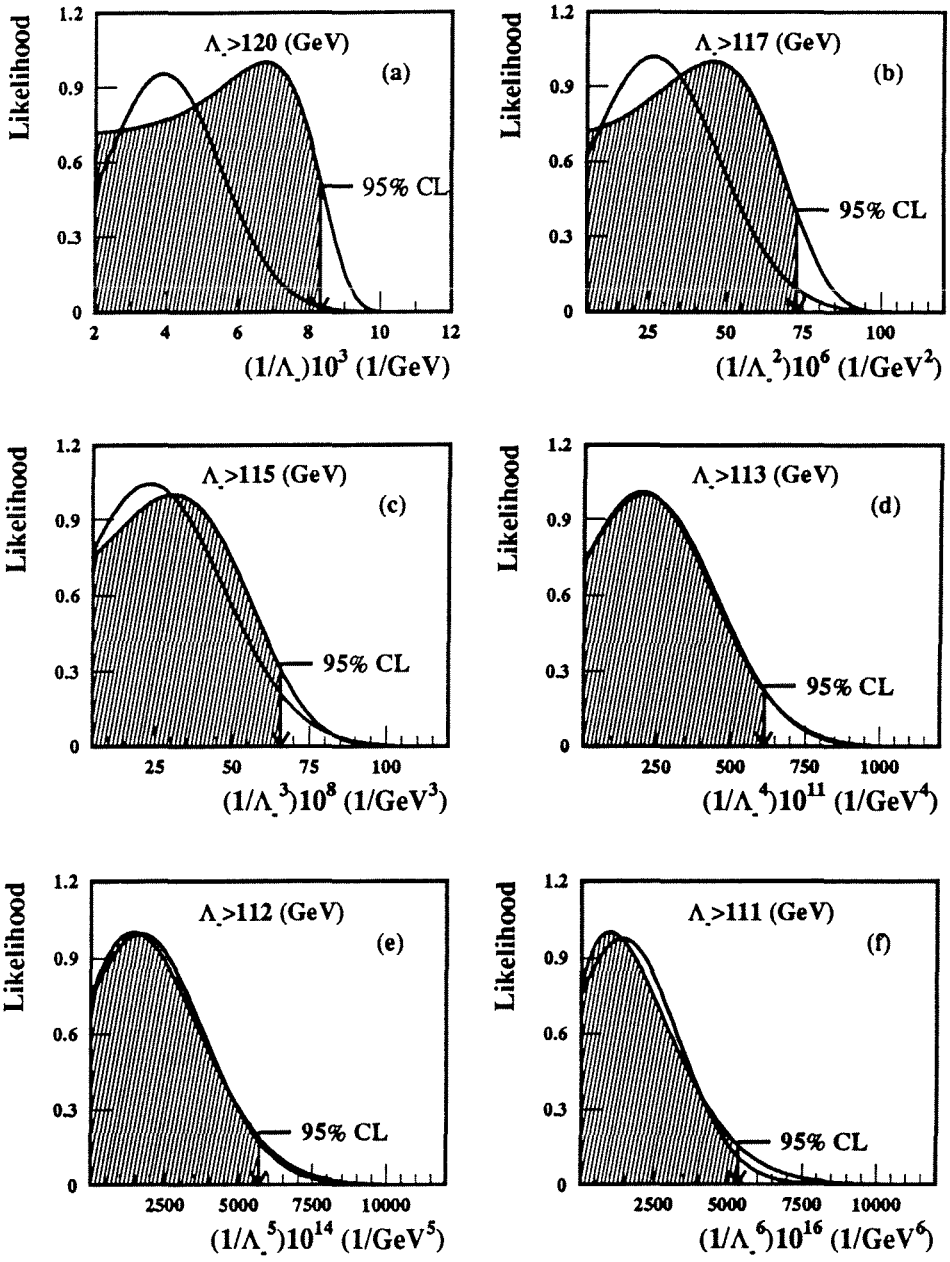

Figure 5.10: The likelihood as a function of the inverse of Λ_- exponentiated to different powers.

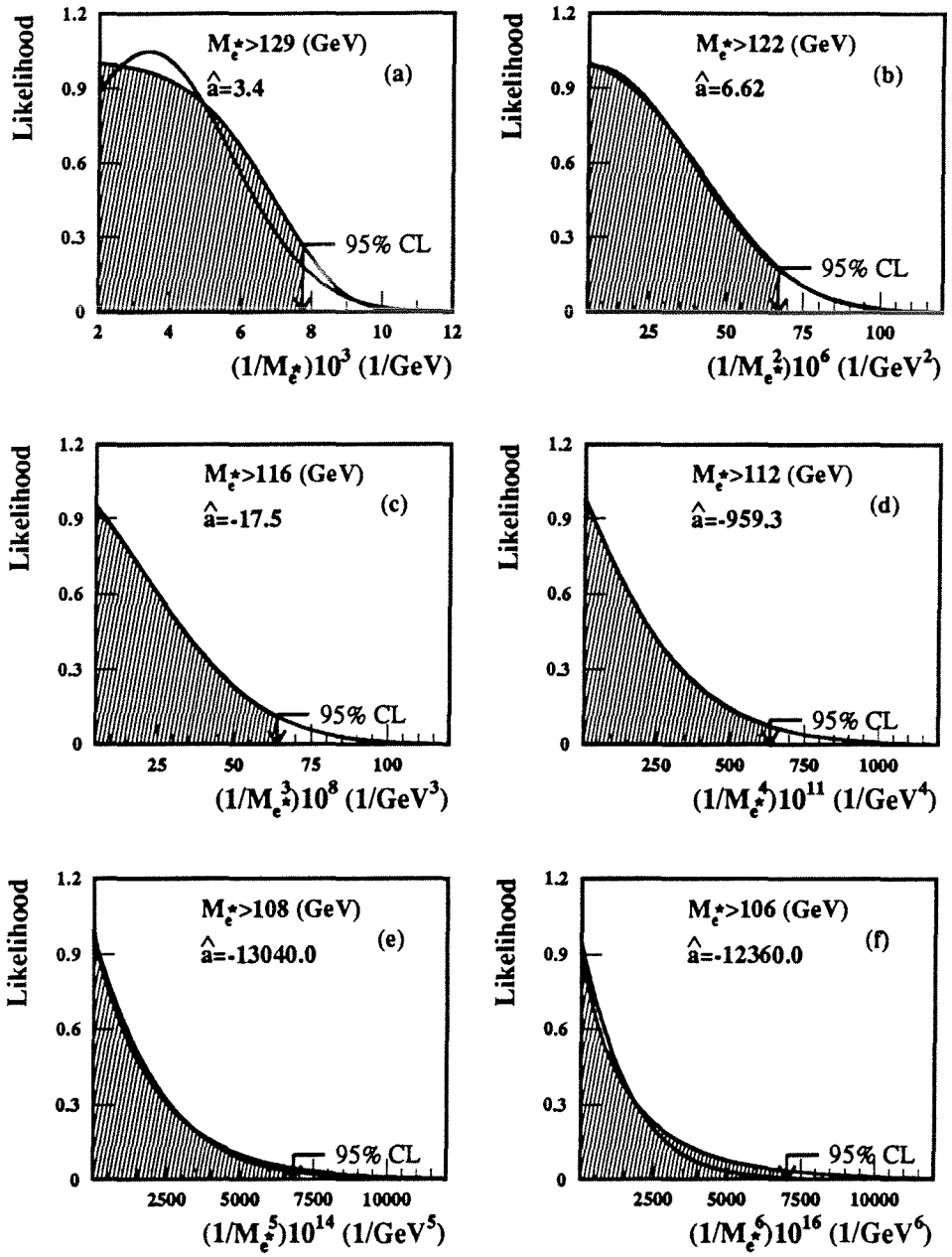

Figure 5.11: The likelihood as a function of the inverse of m_{e^*} exponentiated to different powers.

a distinct minimum which is not however statistically significant. Moving up by two units from that minimum we find that $\Lambda_- > 112$ GeV. The 2σ away from the minimum meets only the left side of the negative log likelihood and that is why we set a one sided limit only. These results are the same with the ones obtained if we perform a transformation of the original parameter to something that makes the likelihood at least a half Gaussian. Figure 5.9 shows the likelihood as a function of the inverted Λ_+ parameter raised to different powers. We notice that transformation (b) is almost a half Gaussian with positive mean value. The Gaussian fit is superimposed and the hatched area indicates the 95% CL limit on the transformed parameter. If the transformed parameter is inverted back to the original one we get from plot (b) that $\Lambda_+ > 133$ GeV. From plot (c) it is found that $\Lambda_+ > 127$ GeV and the Gaussian fits perfectly. But in this plot the mean value is already negative. Therefore the best transformation is somewhere between (b) and (c) and practically we see a complete agreement between the result obtained from the Gaussian transformation and the one obtained directly from the $-\log L(\Lambda_+)$. Figure 5.11 shows the same for the parameter m_{e^*}.

For Λ_- we note that appropriate inversion and exponentiation transforms the likelihood to more than a half Gaussian. In Figure 5.10 transformation (d) makes the likelihood almost a perfect Gaussian and the limit set is $\Lambda_- > 113$ GeV. From the $-\log L(\Lambda_-)$ we found $\Lambda_+ > 112$ GeV which again shows that the method used is consistent.

For everything discussed above we assume that the likelihood or the negative log likelihood is constant when the parameters become more than a few hundred GeV. In particular all limits above were set using an upper cutoff at 500 GeV. The limits however do not depend strongly on this cutoff and this is shown in Figure 5.12 for the case of Λ_+. The limit on this parameter is shown as a function of the inverse of the cutoff and is clearly seen that the limit changes very slowly at low cutoff values. The first point in the plot corresponds to a 300 GeV cutoff and the limit is 129 GeV. As the cutoff increases the limit stabilizes and becomes flat in the TeV range. For a 3 TeV cutoff(which corresponds to the last point in this plot) the limit on Λ_+ is 130.5 GeV.

The effect of these lower bounds on the QED differential cross-section is shown in Figure 5.13 where the ratio of the total cross-section to the QED prediction is plotted. The total cross sections are given from equations 1.3,1.4 with the lower limits found above used for Λ_+, Λ_- and m_{e^*}. The QED prediction to $O(\alpha^3)$ is given from equation 5.8. In the same plot the ratio of the measured to the QED differential cross-section is shown. It is noted that both parameters Λ_+ and

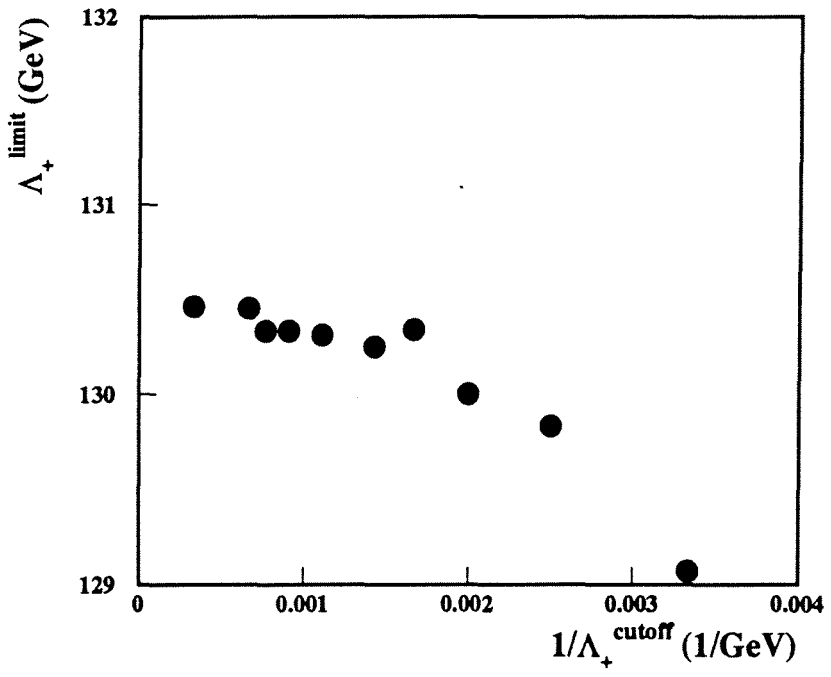

Figure 5.12: The limit set on Λ_+ as a function of the inverse of the cutoff

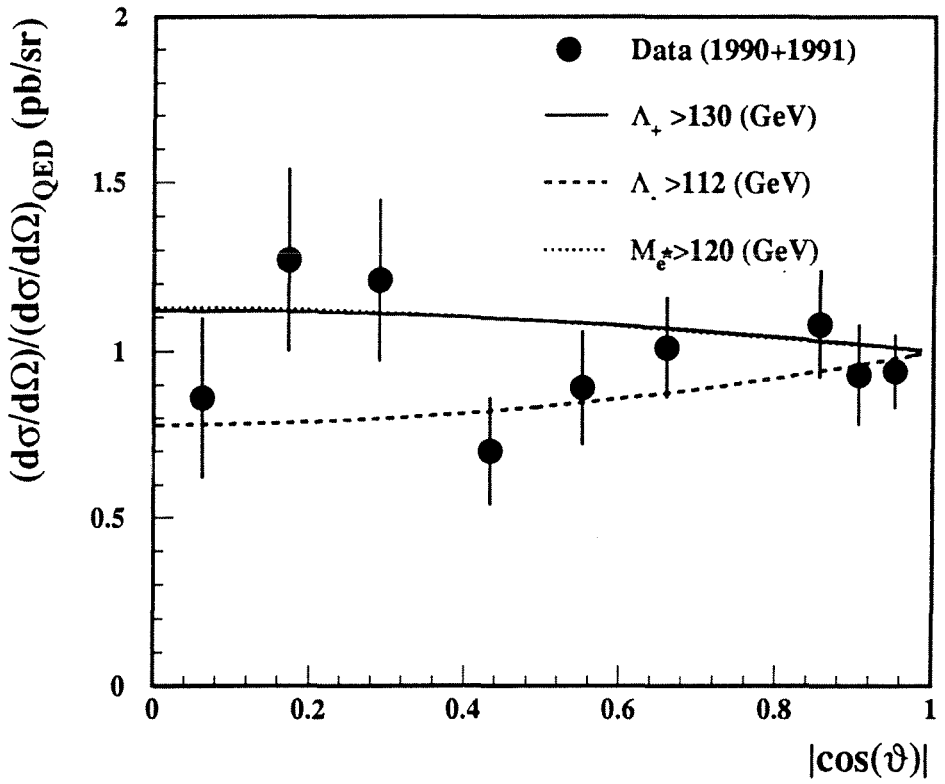

Figure 5.13: The ratio of the measured differential cross section to the QED prediction as a function of the polar angle. Superimposed is the same ratio for the cross-section in the case of a QED breakdown with values for Λ_+, Λ_- and m_{e^*} the lower limits found.

m_{e^*} tend to increase the cross-section through a different functional form. In Figure 5.13 the two curves coincide showing that regardless the functional form used, the data exclude at 95% CL any new effect that would increase(Λ_+, m_{e^*}) or decrease(Λ_-) the cross-section more than it is shown.

5.5.4 Results on Z^0 Rare Decays and Compositeness

In the introduction(1.4.2) we discussed the possibility of photons in the final state as a result of the reactions: $Z^0 \rightarrow \pi^0\gamma$, $Z^0 \rightarrow \eta\gamma$, $Z^0 \rightarrow \gamma\gamma$. The first two have a $(1 + \cos^2\theta)$ angular distribution and the third is forbidden as was shown in 1.4.2. For the forbidden process we conservatively assume a $(1 + \cos^2\theta)$ angular distribution as well. In Chapter 3 we mentioned the different decay modes of π^0 and η and the fact that experimentally we are not able to distinguish between the neutral decay products in the final state because they are all highly colinear. Therefore the experimental signature of such decays is exactly two photons in the final state back to back with half the beam energy each. The QED background cannot be subtracted; so we are looking for an excess of events.

To each process we assign a total efficiency which is the acceptance defined by the angular region covered by the detector, multiplied by the selection efficiency. To find the acceptance we integrate the differential cross-section over the solid angle covered by the detector and divide by the integration over the full solid angle:

(5.18)

$$Acceptance = \frac{\int_{|\cos\theta|_{min}}^{|\cos\theta|_{max}} A\,(1 + \cos^2\theta)d\Omega}{\int_0^1 A\,(1 + \cos^2\theta)d\Omega}$$

$$= 2\pi\frac{(|\cos\theta|_{max} - |\cos\theta|_{min}) + \frac{1}{3}(|\cos\theta|^3_{max} - |\cos\theta|^3_{min})}{8.3775}$$

Using this equation we find the acceptance for 1990 to be 0.6333 and for 1991 0.8365. For 1991 we exclude from the acceptance the 'gap' between barrel and endcap BGO. The efficiency for selecting two photon events was found in section 5.3. For 1990 the selection efficiency is 0.902. Therefore for data collected in the 1990 physics run the total efficiency for the processes $Z^0 \rightarrow \pi^0\gamma$ and $Z^0 \rightarrow \gamma\gamma$ is $0.6333 \times 0.902 = 0.57$. The process $Z^0 \rightarrow \eta\gamma$ has the same total efficiency multiplied by 0.708 to correct for the fact that only this fraction of the η decay modes can be detected.

For the 1991 physics run we split the detector into three regions: (a) the barrel region which is the same as in 1990, (b) the endcap region before FTC and (c) the endcap region with FTC. The efficiency for selecting two photon events in each of these regions was found in section 5.3. Multiplying the acceptance of each of the above regions with the efficiency in that region we find that in 1991 the total efficiency for selecting events candidates of the reactions $Z^0 \to \pi^0\gamma$ and $Z^0 \to \gamma\gamma$ is $0.6333 \times 0.909 + 0.0814 \times 0.823 + 0.1218 \times 0.627 = 0.72$. The total efficiency for the Z^0 decaying into $\eta\gamma$ must again be corrected with the factor 0.708 to account for the η decay modes not observed. Table 5.5 lists the various processes and the total efficiencies for the 1990 and 1991 data.

Process	Acceptance×Efficiency	
	$44° < \theta < 136°$ (1990)	$14° < \theta < 166°$ (1991)
$Z^0 \to \pi^0\gamma$, $\gamma\gamma$	0.57	0.72
$Z^0 \to \eta\gamma$	0.40	0.51

Table 5.5: The acceptance×efficiency for the various processes in the two angular regions considered.

In general the Born cross section at the Z^0 peak for any reaction $Z^0 \to X$ is given by:

$$\sigma_{peak} = \frac{12\pi}{m_Z^2} \frac{\Gamma_{ee}\,\Gamma_X}{\Gamma_Z^2}$$

where Γ_{ee} is the electronic width of the Z^0, Γ_Z the total Z^0 width and Γ_X the width of the rare decay mode under consideration. For the variation of the cross section with the center-of-mass energy we used a Breit Wigner formula with energy dependent width:

$$\sigma_s = \sigma_{peak} \frac{s\Gamma_Z^2}{(s - m_Z^2)^2 + \left(\frac{s\Gamma_Z}{m_Z}\right)^2}$$

For Γ_{ee}, Γ_Z and m_z we used the $L3$ measured values of reference 28. The likelihood constructed uses Poisson statistics to compare for every center-of-mass energy bin the observed and the expected number of events with contributions from QED to $O(\alpha^3)$ and from the Z^0 rare decays:

$$\mathcal{L} = \prod_{i=1}^{7} P(N_i, N_{exp}(\Gamma_X))$$

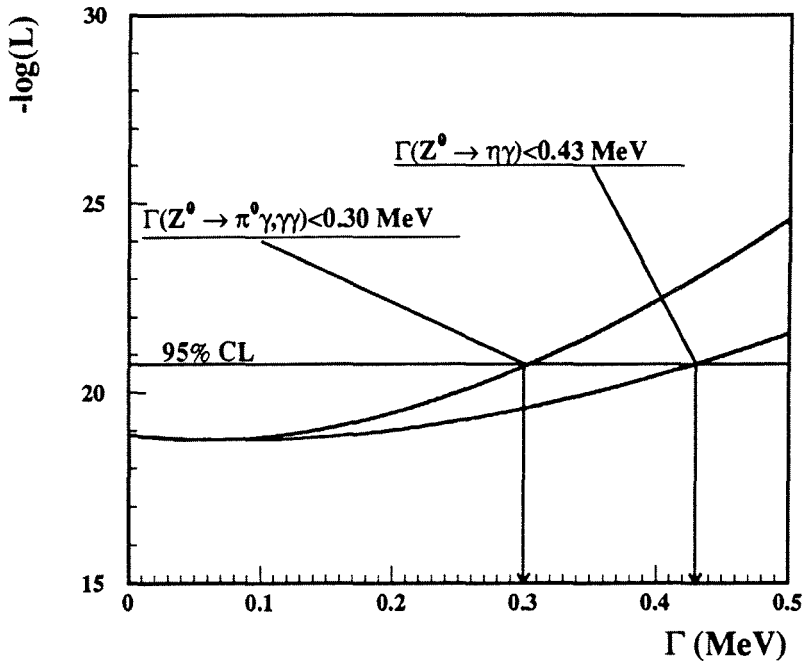

Figure 5.14: The negative log likelihood as a function of the decay width in Mev.

where N_i is the observed number of events for energy bin 'i' and N_{exp} is the expected number for that energy bin. An overestimated total systematic error of 3% was taken into account which includes in quadrature the luminosity uncertainty of 0.9% and the errors on the efficiencies(section 5.3). The negative log likelihood as a function of the width of the decay modes is shown in Figure 5.14. In the last section we discussed how the likelihood function is interpreted. From Figure 5.14 we see that a statistically significant minimum does not exist. We set therefore a 95% CL limit on these rare decays. This is done by moving up from the minimum value of the negative log likelihood by two units and by determining the corresponding widths. At 95% CL the following limits are set:

$$\Gamma(Z^0 \to \eta\gamma) < 0.43\ MeV\ or\ BR(Z^0 \to \eta\gamma) < 1.7 \times 10^{-4}$$

$$\Gamma(Z^0 \to \pi^0\gamma/\gamma\gamma) < 0.3\ MeV\ or\ BR(Z^0 \to \pi^0\gamma/\gamma\gamma) < 1.2 \times 10^{-4}$$

As discussed in the introduction(section 1.4.2) an excess of $e^+e^- \to \gamma\gamma\gamma$ events would be a clear signature for new physics. In composite models the Z^0 may couple to photons through its charged constituents [21]. The three photons in the final state coming from a Z^0 decay may be separated from the QED process $e^+e^- \to \gamma\gamma\gamma$ through their distinct topology. For example the energy of the least energetic photon for a QED event is preferentially low and it is emitted in the forward-backward direction. The cuts for three photon selection were given in section 4.4(B). The number of events expected from QED is calculated using the QED Monte Carlo described in Chapter 3.

We found 10 events(listed in Table 5.6) and from QED we expect 12 $e^+e^- \to \gamma\gamma\gamma$ events.

We should note here that the anomalous term which couples Z^0 to photons has negligible effect away from the Z^0 pole [21] and we therefore only considered events on the Z^0 peak. In total there are 5 events on the Z^0 peak whereas from QED we expect 8.6. Statistically these five events might be coming both from QED and from rare Z^0 decays. In order to put a limit on the number of signal events we must use Poisson statistics taking into account the QED background. Let us assume a mean number of background events μ_B, a mean number of signal events μ_s and a total number of observed events n_0. The accumulative probability to observe up to n_0 events coming all from the background process is:

$$A = \exp -(\mu_B) \sum_{n=0}^{n_0} \frac{(\mu_B)^n}{n!} \tag{5.19}$$

Event	$\sqrt{s}$ (GeV)	E_1 (GeV)	E_2 (GeV)	E_3 (GeV)	θ_3 (deg)	θ_{12} (deg)	θ_{13} (deg)	θ_{23} (deg)
1	91.27	37.4	36.4	9.8	133.0	169.2	113.7	76.9
2	91.27	40.5	33.0	16.3	63.5	158.1	130.2	71.2
3	91.27	45.5	43.7	3.7	60.9	175.0	81.6	103.4
4	89.57	44.2	39.3	5.51	35.8	171.9	123.9	64.1
5	93.00	41.7	36.7	3.6	21.2	175.7	147.8	36.4
6	93.00	44.2	38.1	10.8	49.5	166.2	129.0	64.8
7	93.00	42.0	40.0	13.0	31.3	160.2	112.0	87.7
8	91.27	40.9	29.8	18.2	124.4	157.4	140.2	62.4
9	91.27	45.0	24.5	21.5	81.4	168.1	166.5	25.3
10	92.00	43.4	39.4	7.6	149.1	171.8	115.9	72.2

Table 5.6: Topologies of the three photon events. The center-of-mass energy, the energy of every photon, the polar angle of the least energetic photon and the angle in space between photons are listed.

The accumulative probability to observe up to n_0 events with signal and background contributions is:

$$B = \exp -(\mu_B + \mu_s) \sum_{n=0}^{n_0} \frac{(\mu_B + \mu_s)^n}{n!} \tag{5.20}$$

If the experiment would be repeated many times the probability to observe more than n_0 events given that we expect μ_s signal events and μ_B background events is $1 - B/A$. The 95% CL limit on the number of signal events is given then from the following equation:

$$1 - \frac{\exp -(\mu_B + N) \sum_{n=0}^{n_0} \frac{(\mu_B + N)^n}{n!}}{\exp -(\mu_B) \sum_{n=0}^{n_0} \frac{\mu_B^n}{n!}} = 0.95 \tag{5.21}$$

where N is the signal that we are putting a limit on and it is varied until the above equation is satisfied. With the number of observed events being $n_0 = 5$ and the number of expected background events $\mu_B = 8.6$ the 95% CL limit on the signal is 5 events(it is a coincidence that the limit on the signal is the same as the number of observed events). This result is model independent.

In order to go a step further and derive a limit on the cross-section for the process $Z^0 \rightarrow \gamma\gamma\gamma$(or equivalently a limit on the branching ratio) one needs to make an assumption about the angular distribution of the three photon events coming from the Z^0 decay, consequently one makes a model dependent assumption. From this angular distribution we can find the acceptance which is then multiplied with the selection efficiency to yield the total efficiency. We used an analytic matrix element calculation(Chapter 3) to find the acceptance. The acceptance in a limited angular region is found by dividing the matrix element integrated in the specified region with the matrix element integrated over the whole solid angle. For 1990 the acceptance for detecting Z^0 decaying to three photons was found to be 0.33 and the total efficiency is 0.3. For 1991 the acceptance for the same process is 0.72 and the total efficiency is 0.49. With these total efficiencies, the peak luminosity for 1990 and 1991 and the limit on the number of signal events found above we set a 95% CL limit on the cross-section:

$$\sigma_{Z^0 \rightarrow \gamma\gamma\gamma} < \frac{5}{\mathcal{L}_{1990}\, 0.3 + \mathcal{L}_{1991}\, 0.49} = 1.12\ pb \tag{5.22}$$

or equivalently $\mathrm{BR}(Z^0 \rightarrow \gamma\gamma\gamma) < 3.3 \times 10^{-5}$.

Chapter 6

Conclusions

We studied the reaction $e^+e^- \rightarrow \gamma\gamma(\gamma)$ using the $L3$ detector at energies around the Z^0 resonance. For this analysis the forward-backward electromagnetic calorimeter and the forward-backward tracking chamber were used, in addition to the central tracking chamber and the barrel electromagnetic calorimeter, thus covering 97% of the solid angle(the best among the four LEP experiments). Within the acceptance the total cross-section at seven center-of-mass energy bins was measured(Table 5.3) as well as the differential cross-section at the Z^0 resonance(Table 5.4). The agreement with the QED prediction is very good.

Consequently we looked for non QED effects that would signal new physics. In particular we examined the possible existence of an excited electron coupled to the electron and photon via a new magnetic coupling(section 1.4.1). The diagram involving a virtual excited electron exchanged between the electron and positron would enhance the two photon production rate. No evidence of such an electron was found and lower limits on its mass, m_{e^*}, and the QED cutoff parameters Λ_+ and Λ_-, were set at 95% CL.

Rare or forbidden decay modes of Z^0 with photonic signature in the final state were also looked for. In particular we searched for possible decays of Z^0 to $\pi^0\gamma/\gamma\gamma$ and $\eta\gamma$. For these reactions upper limits on the branching ratios were set at 95% CL. Finally if Z^0 were a composite object it would couple to photons via its charged constituents and one would expect an enhanced three photon production in the final state. Such evidence was not found and we set upper limits on the branching ratio of Z^0 decaying to three photons.

Similar studies have been performed from the other LEP experiments. Table 6.1 summarizes the above results and presents also the published limits set by the other

LEP experiments. The $L3$ publication was based on the analysis described in this

Experiment	$\mathcal{L}$ (pb^{-1})	Acceptance	Λ_+, Λ_- (GeV)	m_{e^*} (GeV)	BR($Z^0 \to \eta\gamma$), BR($Z^0 \to \pi^0\gamma$), BR($Z^0 \to \gamma\gamma\gamma$)
This analysis	14.42	$\lvert\cos\theta\rvert < 0.97$	> 130, 112	> 120	$< 1.7 \times 10^{-4}$, $< 1.2 \times 10^{-4}$, $< 3.3 \times 10^{-5}$
$L3$ [29]	14.20	$\lvert\cos\theta\rvert < 0.97$	> 139, 108	> 127	$< 1.8 \times 10^{-4}$, $< 1.2 \times 10^{-4}$, $< 3.3 \times 10^{-5}$
ALEPH [13]	8.47	$\lvert\cos\theta\rvert < 0.95$	> 107, 132	> 99	$< 5.1 \times 10^{-5}$, $< 2.1 \times 10^{-4}$, $< 1.9 \times 10^{-5}$
DELPHI [30]	4.70	$\lvert\cos\theta\rvert < 0.87$	> 113, 95	> 100	$< 2.8 \times 10^{-4}$, $< 1.5 \times 10^{-4}$, $< 1.4 \times 10^{-4}$
OPAL [15]	7.21	$\lvert\cos\theta\rvert < 0.90$	> 117, 110	> 116	$< 2.0 \times 10^{-4}$, $< 1.4 \times 10^{-4}$, $< 6.6 \times 10^{-5}$

Table 6.1: Summary of results and comparison with other LEP experiments. All limits are at 95%CL.

thesis. The results of the $L3$ publication are slightly different because of minor modifications on the final selection cuts and analysis techniques used for the thesis.

Appendix A

Lowest Order Calculation for $e^+e^- \rightarrow \gamma\gamma$

The lowest order diagrams are shown in Figure 1.1. In the notation used here u, p_2, s_2 are the spinor, four momentum and spin of the incoming electron, v, p_1, s_1 are the same as above but for the incoming positron, ε_1^*, k_1 are the four component polarization and momentum of the first outgoing photon and ε_2^*, k_2 the same for the second outgoing photon. The following definitions are made: $\bar{v} = v^\dagger\gamma^0$ where $v^\dagger$ is the hermitian conjugate of v and for any four vector a, $\not{a} \equiv a_\mu\gamma^\mu = \gamma^\mu a_\mu$ The momentum carried by the virtual electron satisfies four momentum conservation and it is $p = p_1 - k_1$ for the first diagram and $p = p_2 - k_1$ for the second. Using the Feynman rules we form the invariant amplitude $-iM$ which includes both diagrams:

$$-iM = \overbrace{\underbrace{\bar{v}}_{\substack{\text{Incoming}\\\text{Positron}}}\ \underbrace{ie\gamma^\nu}_{\substack{\text{Vertex}\\\text{Factor}}}\ \underbrace{\varepsilon_{1\nu}^*}_{\substack{\text{Outgoing}\\\text{Photon}}}\ \underbrace{\left[i\frac{(\not{p}_1 - \not{k}_1 + m)}{(p_1 - k_1)^2 - m^2}\right]}_{\substack{\text{Electron}\\\text{Propagator}}}\ \underbrace{\varepsilon_{2\mu}^*}_{\substack{\text{Outgoing}\\\text{Photon}}}\ \underbrace{ie\gamma^\mu}_{\substack{\text{Vertex}\\\text{Factor}}}\ \underbrace{u}_{\substack{\text{Incoming}\\\text{Electron}}}}^{\text{First Diagram}} + \overbrace{\bar{v}ie\gamma^\mu\varepsilon_{2\mu}^*\left[i\frac{(\not{p}_2 - \not{k}_1 + m)}{(p_2 - k_1)^2 - m^2}\right]\varepsilon_{1\mu}^*ie\gamma^\nu u}^{\text{Second Diagram}}$$

We introduce now the Mandelstam Lorentz invariant variables s,t,u:

$$s = (p_1 + p_2)^2$$
$$t = (p_1 - k_1)^2$$
$$u = (p_1 - k_2)^2 = (p_2 - k_1)^2$$

To avoid confusion wherever the u channel appears in the same equation with the electron spinor I will be writing $u_{channel}$. For energies around the Z^0 peak the electron mass can be neglected(relativistic limit). Then the amplitude M becomes:

$$M = e^2\bar{v}\left[\gamma^\nu\varepsilon^*_{1\nu}\frac{(\not{p}_1 - \not{k}_1)}{t}\gamma^\mu\varepsilon^*_{2\mu} + \gamma^\mu\varepsilon^*_{2\mu}\frac{(\not{p}_2 - \not{k}_1)}{u_{channel}}\gamma^\nu\varepsilon^*_{1\mu}\right]u$$

and since ε^*_1 and ε^*_2 are just four vectors we can pull them out from the square brackets:

$$M = e^2\varepsilon^*_{1\nu}\varepsilon^*_{2\mu}\bar{v}\left[\gamma^\nu\frac{(\not{p}_1 - \not{k}_1)}{t}\gamma^\mu + \gamma^\mu\frac{(\not{p}_2 - \not{k}_1)}{u_{channel}}\gamma^\nu\right]u$$

Next the amplitude M must be squared so that it corresponds to a probability. The probability that yields has explicit dependence on the spins of the electrons and the polarization of the photons. If the experiment can distinguish between different spin and polarization states then it is correct that the cross-section depends on the spin and the polarization of these states. In the opposite case we must somehow average the contributions to the cross-section of the different spin and polarization states. To see how this is done lets consider the reaction $e^+e^- \to e^+e^-$ were the initial and final electron spins can be either "up" or "down". The following six cases may happen;

$$\overbrace{<\uparrow\uparrow}^{Initial\ State} \mid \overbrace{\uparrow\uparrow>}^{Final\ State} \xrightarrow{Produces} \sigma_1 \equiv \sigma_{\uparrow\uparrow}\ (cross\ section)$$
$$<\downarrow\downarrow \mid \downarrow\downarrow> \longrightarrow \sigma_2 \equiv \sigma_{\downarrow\downarrow}$$
$$\left.\begin{array}{l} <\downarrow\uparrow \mid \downarrow\uparrow> \longrightarrow \sigma_3 \\ <\downarrow\uparrow \mid \uparrow\downarrow> \longrightarrow \sigma_4 \end{array}\right\} \sigma_3 + \sigma_4 \equiv \sigma_{\downarrow\uparrow}$$
$$\left.\begin{array}{l} <\uparrow\downarrow \mid \downarrow\uparrow> \longrightarrow \sigma_5 \\ <\uparrow\downarrow \mid \uparrow\downarrow> \longrightarrow \sigma_6 \end{array}\right\} \sigma_5 + \sigma_6 \equiv \sigma_{\uparrow\downarrow}$$

The notation $\sigma_{\uparrow\uparrow}$ means the cross-section if the intial beams were polarized as shown by the subscript. The question now is what is the cross-section if we do

not know what was initially the polarization of the beams. The electrons will collide with equal probability if the intial spin states were $\uparrow\uparrow$ or $\downarrow\downarrow$ or $\downarrow\uparrow$ or $\uparrow\downarrow$. The cross-section for every one of these initial spin states depends on the possible final spin state configurations and was given above. Then the total average cross-section for unpolarized initial beams is: $\sigma_{Average} = \frac{1}{4}\sigma_{\uparrow\uparrow} + \frac{1}{4}\sigma_{\downarrow\downarrow} + \frac{1}{4}\sigma_{\downarrow\uparrow} + \frac{1}{4}\sigma_{\uparrow\downarrow} = \frac{1}{4}\Big[\sigma_1 + \sigma_2 + (\sigma_3 + \sigma_4) + (\sigma_5 + \sigma_6)\Big]$. Now the famous recipe for providing a spin-independent cross-section is clear: we average over all possible initial spin-states(in this example 4) and we sum over all possible final spin-states arising from each initial spin state(in this example a sum that contains 6 terms). This procedure gives a physical answer and is an average over cross-sections and not amplitudes. Back now to the electron-positron annihilation to two photons. The number of initial spin states for the electron and the positron is four and we must divide with that number. The amplitude squared is:

$$
\begin{aligned}
|M|^2 &= e^4 \overbrace{\varepsilon^*_{1\nu}\varepsilon^*_{2\mu}}^{A} \overbrace{\bar{v}\left[\gamma^\nu \frac{(\not{p}_1 - \not{k}_1)}{t}\gamma^\mu + \gamma^\mu \frac{(\not{p}_2 - \not{k}_1)}{u_{channel}}\gamma^\nu\right]u}^{B} \; (A\,B)^\dagger \\
&= \varepsilon^*_{1\nu}\varepsilon^*_{2\mu}\left(\varepsilon^*_{1\alpha}\varepsilon^*_{2\beta}\right)^* \; \left(B\,B^\dagger\right)_{\nu\alpha\mu\beta}
\end{aligned}
$$

and the polarization plus spin summation must be performed now(dividing by 4 at the same time)

$$
\begin{aligned}
\overline{|M|^2} &= \frac{1}{4}\, e^4 \sum_{T_1}\sum_{T_2}\left[\left(\varepsilon^*_{1\nu}\varepsilon^*_{2\mu}\varepsilon_{1\alpha}\varepsilon_{2\beta}\right)\sum_{s_1}\sum_{s_2}\left(B\,B^\dagger\right)_{\nu\alpha\mu\beta}\right] \\
&= \frac{1}{4}\, e^4 \sum_{T_1}\varepsilon^*_{1\nu}\varepsilon_{1\alpha}\left[\sum_{T_2}\varepsilon^*_{2\mu}\varepsilon_{2\beta}\left(\sum_{s_1}\sum_{s_2}\left(B\,B^\dagger\right)_{\nu\alpha\mu\beta}\right)\right]
\end{aligned}
$$

The "completeness" relations for the electron and positron spinors and for the photon's polarization help to carry out the summation. For the electron's spinors we have that:

$$\sum_{s=1,2} u^{(s)}(p)\bar{u}^{(s)}(p) = \not{p} + m \overset{\nearrow}{0} \text{ (relativistic limit)}$$

and for the positron:

$$\sum_{s=1,2} v^{(s)}(p)\bar{v}^{(s)}(p) = \not{p} - m \overset{\nearrow}{0} \text{ (relativistic limit)}$$

The derivation of these relations is straightforward, if spinors are explicitly written and the summation is carried out [3]. The other summation that needs to be

performed is over the photon polarizations. In general there are four possible polarization states:

$\varepsilon_\mu^{RT} = -\sqrt{\frac{1}{2}}(\varepsilon_1 + i\varepsilon_2)$	Right Handed Transverse Polarization
$\varepsilon_\mu^{LT} = \sqrt{\frac{1}{2}}(\varepsilon_1 - i\varepsilon_2)$	Left Handed Transverse Polarization
$\varepsilon_\mu^{L} = \varepsilon_3$	Longitudinal Polarization
$\varepsilon_\mu^{S} = \varepsilon_0$	Scalar(time like) Polarization

where the four vectors $\varepsilon_1, \varepsilon_2, \varepsilon_3, \varepsilon_4$ are defined as:

$$\varepsilon_1 = (1,0,0,0),\ \varepsilon_2 = (0,1,0,0),\ \varepsilon_3 = (0,0,1,0),\ \varepsilon_0 = (0,0,0,i)$$

So we get:

$$\sum_{\lambda=1}^{4} \varepsilon_\mu^{(\lambda)*}\, \varepsilon_\nu^{(\lambda)} =$$

$$\varepsilon_\mu^{RT*}\varepsilon_\nu^{RT} + \varepsilon_\mu^{LT*}\varepsilon_\nu^{LT} \begin{cases} 1 \text{ for } \mu = \nu = 1,2 \\ 0 \text{ for any other value of } \mu, \nu \end{cases}$$

$$+ \varepsilon_\mu^{L*}\varepsilon_\nu^{L} \qquad \begin{cases} 1 \text{ for } \mu = \nu = 3 \\ 0 \text{ for any other value of } \mu, \nu \end{cases}$$

$$+ \varepsilon_\mu^{S*}\varepsilon_\nu^{S} \qquad \begin{cases} -1 \text{ for } \mu = \nu = 0 \\ 0 \text{ for any other value of } \mu, \nu \end{cases}$$

and therefore:

$$\sum_{\lambda=1}^{4} \varepsilon_\mu^{(\lambda)*}\, \varepsilon_\nu^{(\lambda)} = -g_{\mu\nu}$$

where g is the 4×4 metric tensor defined as:

$$g \equiv \begin{pmatrix} 1 & 0 & 0 & 0 \\ 0 & -1 & 0 & 0 \\ 0 & 0 & -1 & 0 \\ 0 & 0 & 0 & -1 \end{pmatrix}$$

Now we can go back and perform the summing on all photon polarization states:

$$\begin{aligned}
\overline{|M|^2} &= \frac{1}{4}\, e^4 \sum_{T_1} \varepsilon^*_{1\nu}\varepsilon_{1\alpha} \left[\sum_{T_2} \varepsilon^*_{2\mu}\varepsilon_{2\beta} \left(\sum_{s_1}\sum_{s_2} \left(B\, B^\dagger\right)_{\nu\alpha\mu\beta}\right)\right] \\
&= \frac{1}{4}\, e^4(-g_{\nu\alpha})(-g_{\mu\beta}) \left(\sum_{s_1}\sum_{s_2} \left(B\, B^\dagger\right)_{\nu\alpha\mu\beta}\right) \\
&= \frac{1}{4}\, e^4 \sum_{s_1}\sum_{s_2} \Bigg(\bar{v}\left[\gamma^\nu \frac{(\not p_1 - \not k_1)}{t}\gamma^\mu + \gamma^\mu \frac{(\not p_2 - \not k_1)}{u_{channel}}\gamma^\nu\right] u \\
&\qquad \left(\bar{v}\left[\gamma^\nu \frac{(\not p_1 - \not k_1)}{t}\gamma^\mu + \gamma^\mu \frac{(\not p_2 - \not k_1)}{u_{channel}}\gamma^\nu\right] u\right)^\dagger \Bigg)
\end{aligned}$$

$$\begin{aligned}
\overline{|M|^2} = \frac{1}{4}\, e^4 \sum_{s_1}\sum_{s_2} \Bigg(& \left[\bar{v}\gamma^\nu \frac{(\not p_1 - \not k_1)}{t}\gamma^\mu u\right] \left[\bar{v}\gamma^\nu \frac{(\not p_1 - \not k_1)}{t}\gamma^\mu u\right]^\dagger && (B_1) \\
& + \left[\bar{v}\gamma^\mu \frac{(\not p_2 - \not k_1)}{u_{channel}}\gamma^\nu u\right] \left[\bar{v}\gamma^\mu \frac{(\not p_2 - \not k_1)}{u_{channel}}\gamma^\nu u\right]^\dagger && (B_2) \\
& + \left[\bar{v}\gamma^\nu \frac{(\not p_1 - \not k_1)}{t}\gamma^\mu u\right] \left[\bar{v}\gamma^\mu \frac{(\not p_2 - \not k_1)}{u_{channel}}\gamma^\nu u\right]^\dagger && (B_3) \\
& + \left[\bar{v}\gamma^\mu \frac{(\not p_2 - \not k_1)}{u_{channel}}\gamma^\nu u\right] \left[\bar{v}\gamma^\nu \frac{(\not p_1 - \not k_1)}{t}\gamma^\mu u\right]^\dagger \Bigg) && (B_4)
\end{aligned}$$

Now the spin summation for the four terms (B_1), (B_2), (B_3), (B_4) must be performed. The momentum and spin of the spinors is explicitly shown hereafter. The following identities will be used: $\gamma^{0\dagger} = \gamma^0$, $\gamma^{\mu\dagger} = \gamma^0\gamma^\mu\gamma^0$, $(\gamma^0)^2 = \gamma^0$. Also for any two matrices we have: $(AB)^\dagger = B^\dagger A^\dagger$.

First we treat the term (B_1). The second part of this first term is the hermitian conjugate of the first part. We will rearrange the conjugated terms to be able to

perform afterwards the spin summation:

$$
\begin{aligned}
(B_1) = \sum_{s_1}\sum_{s_2} & \left[\bar{v}(p_1,s_1)\gamma^\nu \frac{(\not{p}_1 - \not{k}_1)}{t}\gamma^\mu u(p_2,s_2)\right] \quad \left[\bar{v}(p_1,s_1)\gamma_\nu \frac{(\not{p}_1 - \not{k}_1)}{t}\gamma_\mu u(p_2,s_2)\right]^\dagger \\
= \sum_{s_1}\sum_{s_2} & \vdots \qquad u(p_2,s_2)^\dagger \left[\bar{v}(p_1,s_1)\gamma_\nu \frac{(\not{p}_1 - \not{k}_1)}{t}\gamma_\mu\right]^\dagger \\
= \sum_{s_1}\sum_{s_2} & \vdots \qquad u(p_2,s_2)^\dagger \left[\gamma_\nu \frac{(\not{p}_1 - \not{k}_1)}{t}\gamma_\mu\right]^\dagger \bar{v}(p_1,s_1)^\dagger \\
= \sum_{s_1}\sum_{s_2} & \vdots \qquad u(p_2,s_2)^\dagger \gamma_\mu^\dagger \left[\gamma_\nu \frac{(\not{p}_1 - \not{k}_1)}{t}\right]^\dagger (v(p_1,s_1)^\dagger\gamma_0)^\dagger \\
= \sum_{s_1}\sum_{s_2} & \vdots \qquad u(p_2,s_2)^\dagger \gamma_0\gamma_\mu\gamma_0 \frac{(\not{p}_1 - \not{k}_1)^\dagger}{t}\gamma_\nu^\dagger\gamma_0^\dagger v(p_1,s_1) \\
= \sum_{s_1}\sum_{s_2} & \vdots \qquad \bar{u}(p_2,s_2)\gamma_\mu\gamma_0 \frac{(\gamma_\mu^\dagger p_1^\mu - \gamma_\mu^\dagger k_1^\mu)}{t}\gamma_0\gamma_\nu\gamma_0\gamma_0 v(p_1,s_1) \\
= \sum_{s_1}\sum_{s_2} & \vdots \qquad \bar{u}(p_2,s_2)\gamma_\mu\gamma_0 \frac{(\gamma_0\gamma_\mu\gamma_0 p_1^\mu - \gamma_0\gamma_\mu\gamma_0 k_1^\mu)}{t}\gamma_0\gamma_\nu v(p_1,s_1) \\
= \sum_{s_1}\sum_{s_2} & \vdots \qquad \bar{u}(p_2,s_2)\gamma_\mu \frac{(\gamma_\mu p_1^\mu - \gamma_\mu k_1^\mu)}{t}\gamma_\nu v(p_1,s_1) \\
= \sum_{s_1}\sum_{s_2} & \vdots \qquad \bar{u}(p_2,s_2)\gamma_\mu \frac{(\not{p}_1 - \not{k}_1)}{t}\gamma_\nu v(p_1,s_1)
\end{aligned}
$$

Now each matrix will be assigned indices so we can group terms together and use the electron's and positron's completeness relations given above to perform the spin summation:

$$
\begin{aligned}
(B_1) =& \frac{1}{t^2}\left(\sum_{s_1}\bar{v}(p_1,s_1)_\alpha\gamma^\nu_{\alpha\beta}(\not p_1 - \not k_1)_{\beta\gamma}\gamma^\mu_{\gamma\delta}\right)\times \\
& \left(\sum_{s_2}u(p_2,s_2)_\delta\bar{u}(p_2,s_2)_\epsilon\gamma^{\epsilon\zeta}_\mu(\not p_1 - \not k_1)_{\zeta\eta}\gamma^{\eta\theta}_\nu v(p_1,s_1)_\theta\right) = \\
& \frac{1}{t^2}\left(\sum_{s_1}v(p_1,s_1)_\theta\bar{v}(p_1,s_1)_\alpha\gamma^\nu_{\alpha\beta}(\not p_1 - \not k_1)_{\beta\gamma}\gamma^\mu_{\gamma\delta}\right)\times \\
& \left(\sum_{s_2}u(p_2,s_2)_\delta\bar{u}(p_2,s_2)_\epsilon\gamma^{\epsilon\zeta}_\mu(\not p_1 - \not k_1)_{\zeta\eta}\gamma^{\eta\theta}_\nu\right) = \\
& \frac{1}{t^2}\not p_{1\theta\alpha}\gamma^\nu_{\alpha\beta}(\not p_1 - \not k_1)_{\beta\gamma}\gamma^\mu_{\gamma\delta}\not p_{2\delta\epsilon}\gamma^{\epsilon\zeta}_\mu(\not p_1 - \not k_1)_{\zeta\eta}\gamma^{\eta\theta}_\nu
\end{aligned}
$$

Notice now that all matrix indices are in sequence and this is just the trace of the whole matrix expression:

$$
(B_1) = \frac{1}{t^2}\,Trace\left(\not p_1\gamma^\nu(\not p_1 - \not k_1)\gamma^\mu\not p_2\gamma_\mu(\not p_1 - \not k_1)\gamma_\nu\right)
$$

Standard trace theorems are used to handle the remaining of the calculation. Those that we will use here are: $Tr(\not a\ \not b\ \not c\ \not d\ ) = 4[(a\cdot b)(c\cdot d) - (a\cdot c)(b\cdot d) + (a\cdot d)(b\cdot c)]$ where a, b, c, d are the four vectors(like momentum p for example) Also the following matrix relations: $\gamma_\mu\gamma^\mu = 4$, $\gamma_\mu\not a\gamma^\mu = -2\not a$,
$\gamma_\mu\not a\not b\not c\gamma^\mu = -2\not c\not b\not a$.

$$
\begin{aligned}
(B_1) =& \frac{1}{t^2}\,Tr(\not p_1\gamma^\nu(\not p_1 - \not k_1)(-2)\not p_2(\not p_1 - \not k_1)\gamma_\nu) \\
=& (-2)\frac{1}{t^2}\,Tr((\not p_1\gamma^\nu\not p_1 - \not p_1\gamma^\nu\not k_1)(\not p_2\not p_1\gamma_\nu - \not p_2\not k_1\gamma_\nu)) \\
=& (-2)\,\frac{1}{t^2}\,Tr(\not p_1\gamma^\nu\not p_1\not p_2\not p_1\gamma_\nu - \not p_1\gamma^\nu\not p_1\not p_2\not k_1\gamma_\nu - \\
& \qquad \not p_1\gamma^\nu\not k_1\not p_2\not p_1\gamma_\nu + \not p_1\gamma^\nu\not k_1\not p_2\not k_1\gamma_\nu) \\
=& 4\,\frac{1}{t^2}\,Tr(\not p_1\not p_1\not p_2\not p_1 - \not p_1\not k_1\not p_2\not p_1 - \not p_1\not p_1\not p_2\not k_1 + \not p_1\not k_1\not p_2\not k_1)
\end{aligned}
$$

$$
\begin{aligned}
(B_1) = 4\,\frac{1}{t^2}\ \times\ & \Big(4\ [(p_1\cdot p_1)(p_2\cdot p_1) - (p_1\cdot p_2)(p_1\cdot p_1) + (p_1\cdot p_1)(p_1\cdot p_2)] - \\
& 4\ [(p_1\cdot k_1)(p_2\cdot p_1) - (p_1\cdot p_2)(k_1\cdot p_1) + (p_1\cdot p_1)(k_1\cdot p_2)] - \\
& 4\ [(p_1\cdot p_1)(p_2\cdot k_1) - (p_1\cdot p_2)(p_1\cdot k_1) + (p_1\cdot k_1)(p_1\cdot p_2)] + \\
& 4\ [(p_1\cdot k_1)(p_2\cdot k_1) - (p_1\cdot p_2)(k_1\cdot k_1) + (p_1\cdot k_1)(k_1\cdot p_2)] \Big) \\
= 4\,\frac{1}{t^2}\ 8\ & \overbrace{(p_1\cdot k_1)}^{-t/2}\overbrace{(p_2\cdot k_1)}^{-u/2} \\
= 32\,\frac{1}{4}\,\frac{u}{t} & \\
= 8\,\frac{u}{t} &
\end{aligned}
$$

This is the contribution to the cross-section from the t channel. The term (B_2) is the u channel contribution and the calculation is done in exactly the same way as for the t channel. We find that:

$$(B_2) = 8\,\frac{t}{u}$$

Finally we must calculate the interference terms (B_3) and (B_4). Following the same procedure as for the term (B_1) we arrive at the expressions:

$$
\begin{aligned}
(B_3) &= \frac{1}{t\,u}\ Trace\Big(\not p_1\gamma^\nu(\not p_1 - \not k_1)\gamma^\mu\ \not p_2\gamma_\nu(\not p_2 - \not k_1)\gamma_\mu \Big) \\
(B_4) &= \frac{1}{u\,t}\ Trace\Big(\not p_1\gamma^\mu(\not p_2 - \not k_1)\gamma^\nu\ \not p_2\gamma_\mu(\not p_1 - \not k_1)\gamma_\nu \Big)
\end{aligned}
$$

The same trace theorems as before can be used:

$$
\begin{aligned}
(B_3) &= \frac{1}{t\,u}\ Tr[(-2)\ \not p_1\gamma^\nu(\not p_1 - \not k_1)(\not p_2 - \not k_1)\gamma_\nu\ \not p_2] \\
&= \frac{-8}{t\,u}\ Tr[\ \not p_1[(p_1 - k_1)\cdot(p_2 - k_1)])\ \not p_2] \\
&= \frac{-32}{t\,u}\ (p_1\cdot p_2)[(p_1 - k_1)\cdot(p_2 - k_1)] \\
&= \frac{-32}{t\,u}\ (p_1\cdot p_2)[p_1\cdot p_2 - k_1\cdot(p_1 + p_2)]
\end{aligned}
$$

This term does not vanish. The second interference term comes out to be the same exact expression:

$$(B_4) = \frac{-32}{u\,t}\,(p_1 \cdot p_2)[p_1 \cdot p_2 - k_1 \cdot (p_1 + p_2)]$$

Therefore the interference terms do not cancel out and are non zero. However the final expression does not involve the interference terms in the high energy limit for the following reason: The product of the two four momenta $p_1 \cdot p_2$ is

$$\begin{aligned} p_1 \cdot p_2 &= E_{beam}^2 - (\vec{p_1} \cdot \vec{p_2}) \\ &= E_{beam}^2 - (-p_e^2) \\ &= p_e^2 + m_e^2 + p_e^2 \end{aligned}$$

The colliding beams have space momenta of the same magnitude in opposite directions and therefore $p_1 + p_2 = (0, 2E_{beam})$ The photon space momentum is in magnitude equal to the beam energy. The product then $k_1 \cdot (p_1 + p_2)$ becomes:

$$k_1 \cdot (p_1 + p_2) = 2\ E_{beam}^2$$

Subtracting the last two expressions we see that:

$$(B_3) = (B_4) = \frac{-32}{u\,t}\left(2\,p_e^2 + m_e^2 - 2\,E_{beam}^2\right) \approx 0$$

The last result is true if the electron mass is neglected; i.e at the high energy limit.

We arrive consequently to the following final matrix element:

$$\overline{|M|^2} = 2\,e^4\left(\frac{t}{u} + \frac{u}{t}\right)$$

This is the well known matrix element for the lowest order two photon annihilation. Note again that the above result is only a good approximation in the high energy limit(beam energy above a few MeV).

Appendix B

Analysis of the PSF data

B.1 Quality of data, Technical performance

B.1.1 Dead fibers and Misthreadings

To facilitate TEC installation some fibers had to be cut. A few others were damaged. With adequate statistics we can plot the fiber hit distribution for all runs and determine which fibers (or regions) are cut or are dead. Figure B.1 shows this distribution for the first ribbon. The first 23 fibers are known to be cut. The few hits in these fibers are because of electronic noise. One way to estimate the random electronic noise is to sum all hits for these 23 cut fibers and divide with the number of hits of 23 active fibers. The electronic noise is of the order of 1%. In addition to these known twenty three we can see two more fibers (number 57 and 89) which are certainly dead.

At the end of every ribbon there are two faceplates in which the fibers are threaded. Every faceplate is then aligned to the multianode photomultiplier. There is a map of how the fibers are threaded in and which fiber corresponds to which anode. From now on the following two fundamental quantities will be used :

1. X_{track} *is the distance of the track at the PSF from the anode plane extrapolated to ribbon.*

2. X_{psf} *is the distance of the fiber hit from the anode plane.*

If we define a variable $X_{separation} = X_{track} - X_{psf}$, this should be a continuous distribution as a function of the fiber number which should normally be centered

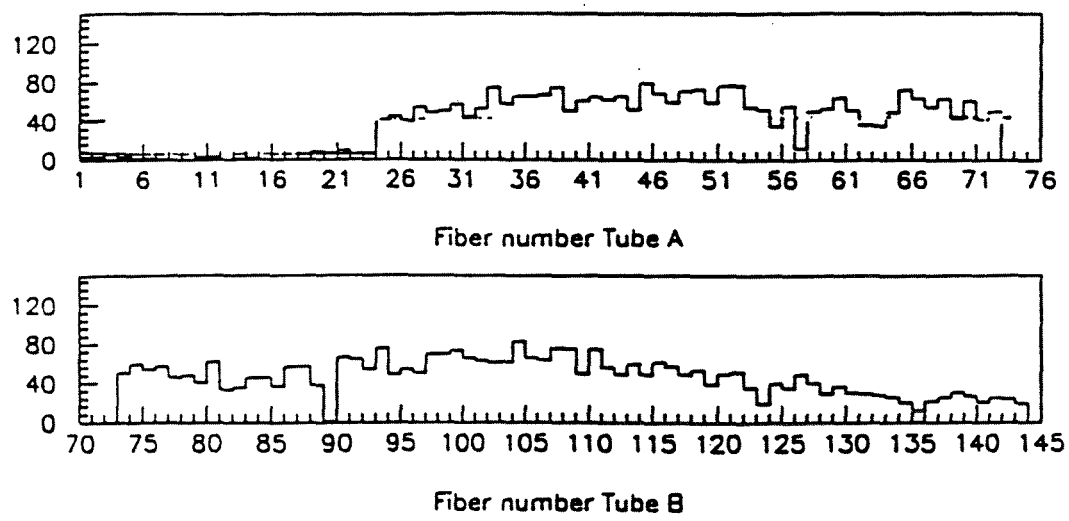

Figure B.1: Fiber number distribution for the first ribbon. From this fiber hit pattern dead fibers can be determined.

around zero. Discontinuities or gaps in this distribution expose misthreadings, which can be corrected offline. Figure B.2 and Figure B.3 shows two such examples.

B.1.2 Efficiency of the system, Resolution

We assess the efficiency of the PSF system by defining the average efficiency per half sector. This choice comes naturally because each half sector is covered by 72 fibers which are read by a single tube. Tracks are extrapolated to PSF and a window is defined in which we look for a fiber hit. If a fiber hit is found the track is considered to be associated with this fiber. In an ideal case 0.350 mm (half a fiber width) window on either side of the track would be sufficient. Instead the window chosen was 1.5 mm to avoid losing data since the efficiency calculation was done before the detector was aligned. The efficiency per half sector is defined:

$$EFFICIENCY\ PER\ HALF\ SECTOR = \frac{Number\ of\ Tracks\ with\ PSF\ attached}{Total\ Number\ of\ Tracks}$$

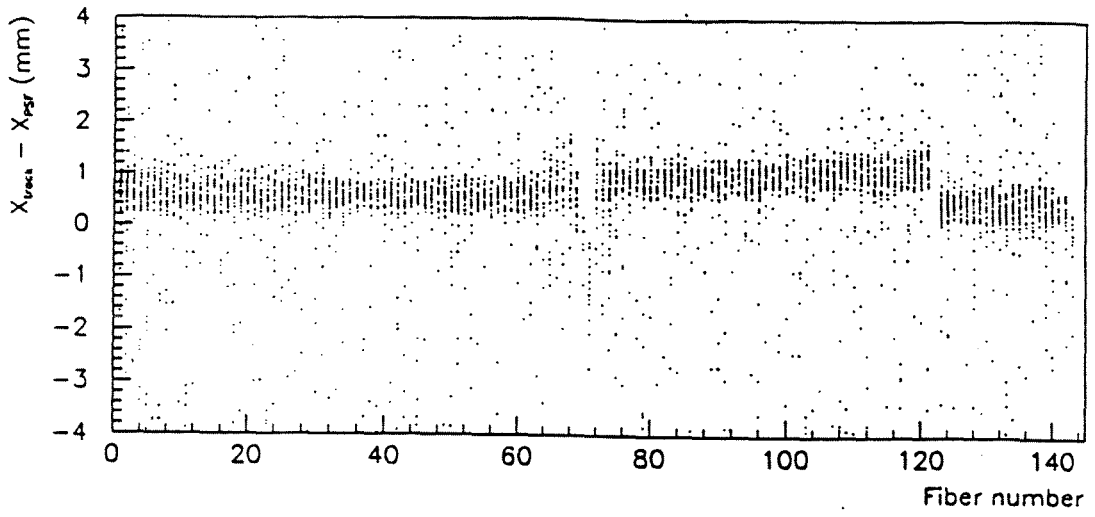

Figure B.2: Track-fiber separation versus fiber number. Ribbon 16 has most of its second half misthread. As a result a discontinuity is formed.

In calculating the average efficiency we accounted for :

1. *Dead fibers*
2. *Limited geometrical acceptance of TEC from PSF*
3. *Cladding between fibers*

With the above definition random electronic noise has little influence on the efficiency calculation. Within the small window that we require for a track-PSF match there is small probability for a random PSF hit. A few tubes were broken and efficiency for these half sectors was not calculated. No significant dependence of the efficiency along the Z axis was observed.

Ideally the $X_{track} - X_{PSF}$ distribution(resolution plot) should be a square wave with a width of 570 μm (active region of fiber) centered around zero. However any deviation from the ideal case would change this shape (George Alverson Northeastern University, L3 note # 314). We know for example that the tracks have an extrapolation error of about 50-100 μm (due to diffusion of the drifting pulses,

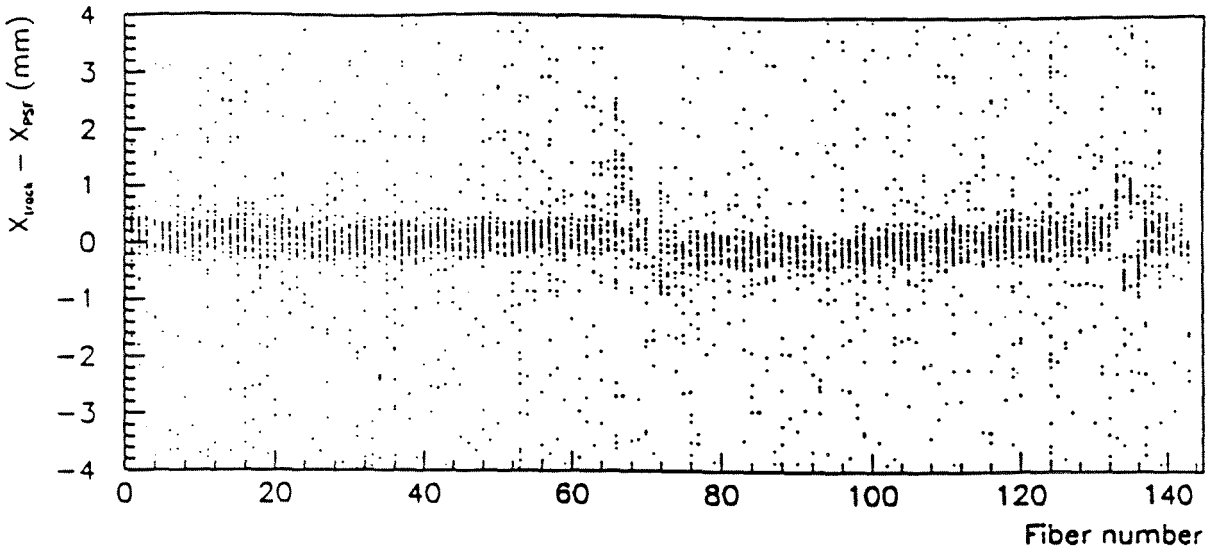

Figure B.3: Track-fiber separation versus fiber number.Ribbon 17 has only a local misthread on the second half. As a result a hole is formed.

fitting problems, multiple scattering). A gaussian is fitted to the resolution plot and the σ of the fit is the resolution for the particular ribbon. Figure B.4 shows the efficiency per half sector and Figure B.5 the Z dependence of the efficiency.

B.1.3 Tube alignment, Correlated hits

The accurate alignment between the fibers threaded in the faceplate and the tube, is done using an intermediate ring. In this way one fiber corresponds to one anode on the other side of the photocathode plate. However offline we discovered in some cases a small misalignment. Because of the effect just mentioned and the particular fiber-anode mapping that we are using, we notice a second peak about 4 mm (six fibers) away from zero. This was not a problem for our analysis and only contributed to a small inefficiency for those sectors (since sometimes the wrong anode picks up the light). We took the necessary measures to correct the hardware. To quantify the problem we measured the number of entries under the second peak and divide with the number of entries under the main peak. Figure B.6 shows an

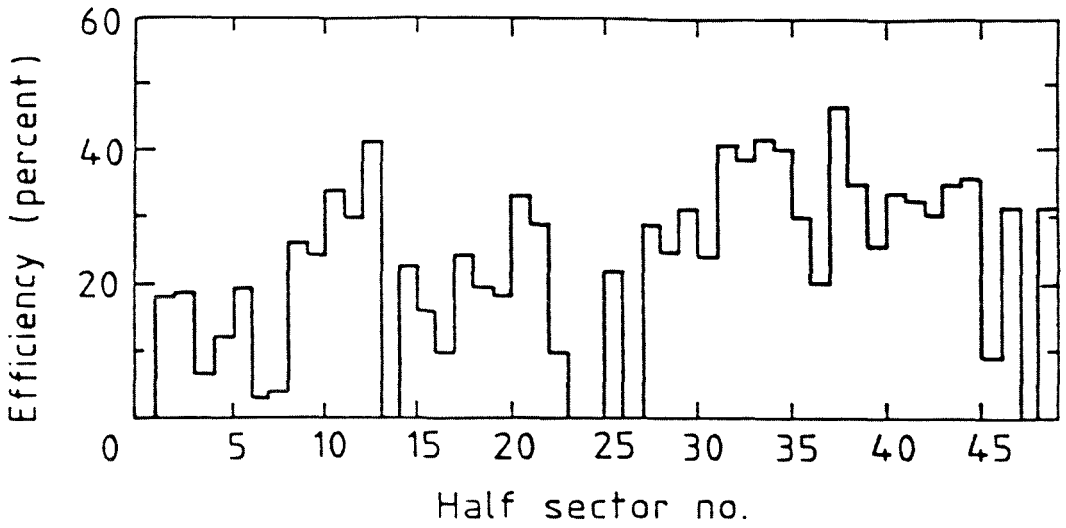

Figure B.4: Efficiency versus half sector number for 1990 physics run period.

example of a sector with a misalignment problem. Another unknown effect was the observation of secondary correlated hits adjacent to the original ones. When a track goes through a particular fiber it may create an additional hit on the nearby fiber. Using real data the magnitude of the effect was measured and was found that given a primary matched fiber there is a probability of 5%-7% to have a secondary fiber hit associated to the same track. This interesting phenomenon (its importance is more general than in just our calibration, as for example in the detectors that may use fibers in the SSC accelerator) was studied in more detail with Geant by (George Alverson Northeastern University, L3 note # 314). The conclusion is that we may account for it with δ rays emitted, from the passage of the primary particle, inside TEC, or the TEC Al cylinder. Table B.1 summarizes the results on the hardware performance of the detector.

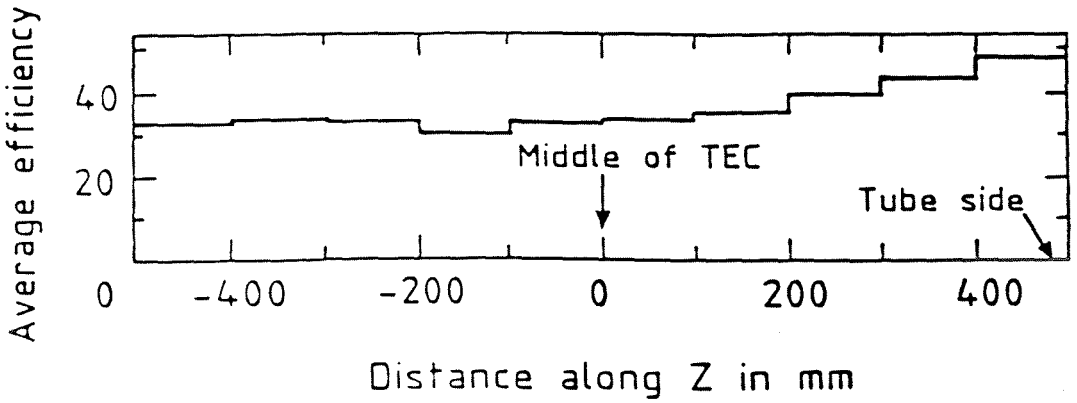

Figure B.5: The dependence of efficiency on the Z coordinate.

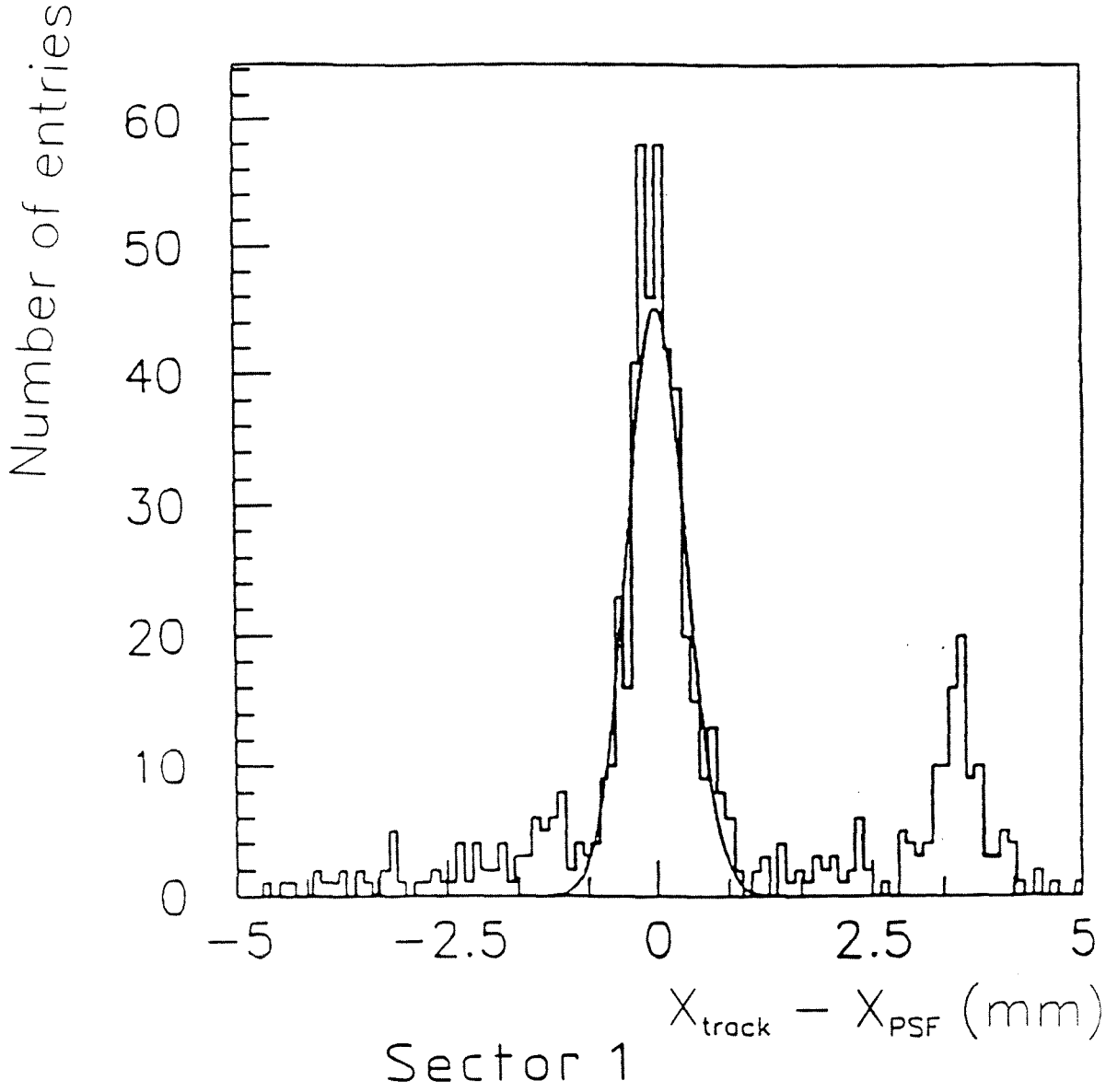

Figure B.6: Separation between tracks and fiber hits for tube 1. Notice the second peak 4 mm apart from the primary peak.

Sector	Half sector	Tube	Resolution (μm)	Efficiency (%)	Dead fibres	Misalignment (%)
1	1	1A	241	18.2	24	27.5
	2	1B		18.7	1	6.2
2	3	2A	228	6.4	—	<5
	4	2B		12.2	2	<5
3	5	3A	287	19.5	0	17.5
	6	3B		2.8	—	52.7
4	7	4A	274	3.7	—	<5
	8	4B		26.2	2	<5
5	9	5A	229	24.4	0	41.0
	10	5B		34.1	2	6.2
6	11	6A	253	29.9	0	<5
	12	6B		41.3	1	<5
7	13	7A	230	—	—	<5
	14	7B		22.4	0	16.6
8	15	8A	264	15.8	11	<5
	16	8B		9.8	0	16.2
9	17	9A	219	24.1	0	9.4
	18	9B		19.5	0	11.7
10	19	10A	240	18.1	0	8.7
	20	10B		33.5	0	7.2
11	21	11A	230	29.1	0	8.0
	22	11B		9.7	0	49.5
13	25	13A	221	21.9	23	<5
	26	13B		—	—	<5
14	27	14A	215	28.8	1	<5
	28	14B		24.8	0	<5
15	29	15A	220	31.1	0	<5
	30	15B		24.1	0	<5
16	31	16A	304	40.1	0	<5
	32	16B		38.8	1	<5
17	33	17A	232	42.0	0	<5
	34	17B		40.3	0	10.4
18	35	18A	213	30.0	0	<5
	36	18B		20.1	1	<5
19	37	19A	270	46.8	0	<5
	38	19B		35.1	0	<5
20	39	20A	303	25.8	1	<5
	40	20B		33.8	1	<5
21	41	21A	212	32.7	0	<5
	42	21B		30.5	0	<5
22	43	22A	231	35.2	0	<5
	44	22B		36.2	0	5.8
23	45	23A	243	9.2	0	<5
	46	23B		31.7	0	<5
24	47	24A	198	—	—	—
	48	24B		31.5	27	<5

Table B.1: Summary of the PSF performance in 1990. Outer TEC sector 12 was dead and PSF was not tested for this sector.

B.2 Alignment of the PSF detector

B.2.1 Definition of PSF geometry

The analysis above was only preliminary and it was meant to reveal hardware problems (broken tubes, dead fibers, misalignment, correlated hits). The next question to be answered was the positioning of the PSF detector with respect to TEC. The precise knowledge of its position is crucial to achieve the desired accuracy (0.1%) on the drift velocity calibration. There are four parameters that specify completely the geometry of the PSF(refer to second plot of Figure 2.13 for a cross section of an outer TEC sector with the PSF on it) :

1. *The distance of the intersection point of the extrapolated anode plane with the ribbon, from the center of TEC, known as radius of the PSF. The nominal value is 459.3 mm*

2. *The angle of the normal of the ribbon with respect to the anode plane, known as slant. The nominal value is* 0°.

3. *The mean distance between fibers, known as pitch. The nominal value is 0.7 mm*

4. *The distance of the middle of the ribbon from the extrapolated anode plane, known as global offset. The nominal value is 1 mm*

The above parameters completely specify the geometry on the $r\Phi$ plane. In addition there could be a dependence along the Z axis (that runs along the cylinder of TEC) but as mentioned before it shows to be very small. The above nominal values are just indicative. A more detailed study of the exact geometry of the PSF system was needed in order to reach the desired level of accuracy for the calibration. PSF is meant to be a precise external point on the track. Suffice to say here that using PSF the aim is to get the drift distance of the pulses and with the drift time from the FADC's the drift velocity. The analytical formulas for the drift distance use explicitly all of the above PSF geometric parameters. For example a systematic error of 1% on the Radius or the Pitch would translate to 1% in the drift velocity calculation with the algorithm that will be described later on. A method was developed that uses positive and negative tracks(opposite curvature) and the continuity between two halves of a TEC sector, to obtain accurate values for the geometry.

B.2.2 Tools and Constraints

The method to be described uses four data samples. Every outer TEC sector is naturally divided into two halves one for either side of the anode plane. For every half we considered positive and negative tracks crossing the drift volume and then the fiber plane. TEC is located inside a homogeneous magnetic field and particles with opposite charges have opposite curvature. When we observe a fiber hit this can be either from positive or negative tracks. Therefore the tracks cross at the vertex and at the PSF. In other words positive and negative tracks are circles with opposite curvature and two common points. One is the vertex and the other must be located on the PSF. In addition we have continuity within a ribbon. So the pitch is assumed to be the same (on the average) throughout the ribbon and the results from the first half must agree with the second half. A third point is that the track-hit separation must be minimum in an ideal situation. Thus the underlying constraints can be summarized in the following three conditions :

CONDITION A *With the correct geometry the positive and negative tracks must meet at the PSF, i.e.. the track-hit separation must be the same for positive and negative tracks (triangulation).*

CONDITION B *The first and second half of the same TEC sector must give consistent results.*

CONDITION C *In an ideal case the track-hit separation must be minimum.*

The geometry parameters defined in section B.2.1 are strongly correlated and also correlated to the track parameters. The conditions described in this section are the principles used to determine the geometry parameters. In order to find a unique solution the correlations must be resolved. The alignment method described breaks these correlations and this will be shown in a forthcoming paragraph.

B.2.3 Introduction to the Alignment Method

The fibers give the information whether a track went through or not. Therefore fundamentally the only direct measurement we can make is the determination of the distance between the PSF hit and the intersection point of the track(extrapolated at the PSF) with the PSF ribbon, $X_{track} - X_{PSF}$. We can use the resolution plot to determine where PSF exactly is. The resolution plot is fitted to a gaussian and the mean value and the σ of the fit can be used (one set for every data sample) :

1. M_{n1h}, σ_{n1h} *is the mean value and the* σ *of the fit using all negative tracks in the first half.*

2. M_{p1h}, σ_{p1h} *is the mean value and the* σ *of the fit using all positive tracks in the first half.*

3. M_{n2h}, σ_{n2h} *is the mean value and the* σ *of the fit using all negative tracks in the second half.*

4. M_{p2h}, σ_{p2h} *is the mean value and the* σ *of the fit using all positive tracks in the second half.*

The above indices (n,p,1h,2h) will be used elsewhere as well.

For every data sample above the offset from zero of the mean value and the σ depend on the geometry and the TEC track parameters. So the important starting point is that, because of adequate statistics, we know the mean value of the gaussian fit to the resolution plot to better than 15 μm.(δMean $=\frac{\sigma}{\sqrt{N}}$ N is the number of tracks used). Figure B.7 shows a typical resolution plot. A center of gravity method and a 3σ cut was done to eliminate the tails. It is very important to eliminate tails on the gaussian distribution because they seriously bias the mean value of the gaussian fit. The sensitivity of the particular fits to rebinning and repopulation of the bins was examined to see the upper limit of a bias that could arise from the fit. We found that this bias is less than 15μm. Because the geometry is wrong the mean has an offset from zero. This offset is different for the different data samples used consisting of positive and negative tracks first and second half. To illustrate the above argument Figure B.8 presents a set of four diagrams. The view displayed is the $r\Phi$, slice of one TEC sector. There are 4 cases each one illustrating the PSF geometry if one of the geometry parameters is wrong

B.2.4 Calculation of the Radius and the Slant

An arbitrary starting value for the radius is chosen and we form two differences one for every half :

$$D_{1h} = M_{n1h} - M_{p1h} \ , D_{2h} = M_{n2h} - M_{p2h}$$

With some step size the procedure is repeated. Then D_{1h} , D_{2h} are drawn as a function of the radius Figure B.9. Referring to Figure B.8 (a) we realize that if the correct radius is chosen then $D_{1h} = D_{2h} = 0$. A straight line is fitted as a

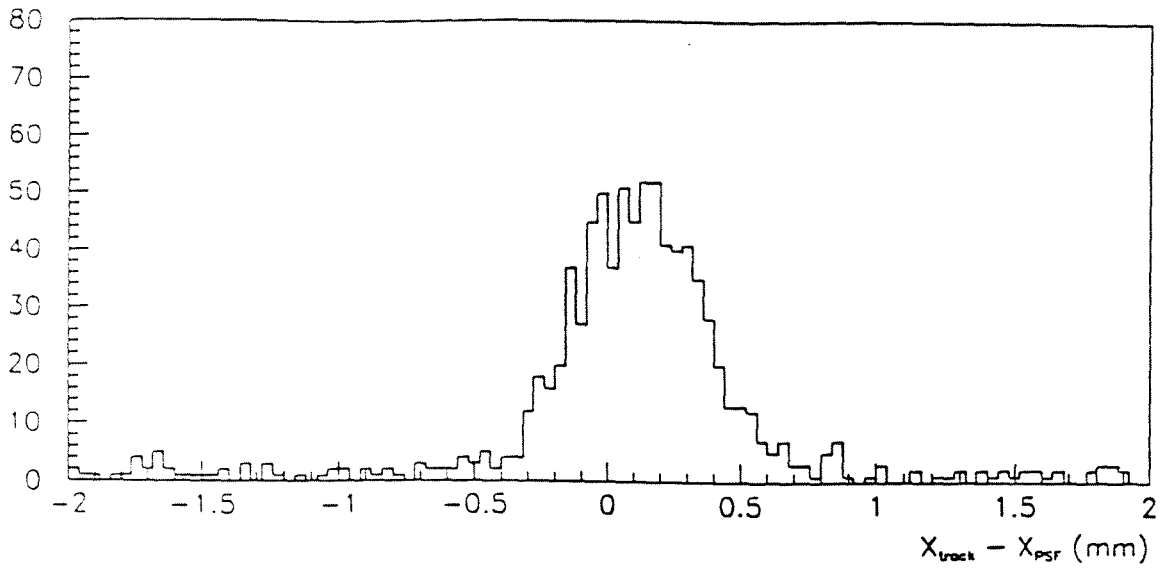

Figure B.7: Separation between tracks and PSF hits. Here the data sample includes all positive tracks in the first half.

consequence to every one of the two plots in Figure B.9 and we find the radii for which $D_{1h} = D_{2h} = 0$ That is $R_{1h} \implies D_{1h} = 0$ and $R_{2h} \implies D_{2h} = 0$. This may seem strange since by definition there is only one radius for every sector. Referring to Figure B.8 (b) we realize that the above result comes from the fact that we did not account for the slant. If we shift the PSF plane perpendicular to the anode plane trying to minimize D_{1h} and D_{2h} we notice that a correction on the radius of δR_{1h} is needed for one half and δR_{2h} for the other. But this is all because the PSF plane is shifted at the wrong angle with respect to the anode plane. Changing the slant we eventually arrive to a slant value that compromises the two halves to the same radius, which by definition is the correct one. In practice what is done is to make two more plots were the difference $R_{1h} - R_{2h}$ is plotted as a function of the slant Figure B.10 and as a function of R_{1h} Figure B.11. In both plots we fit a straight line. The abscissa for which $R_{1h} - R_{2h} = 0$ yields the correct slant and the correct radius.

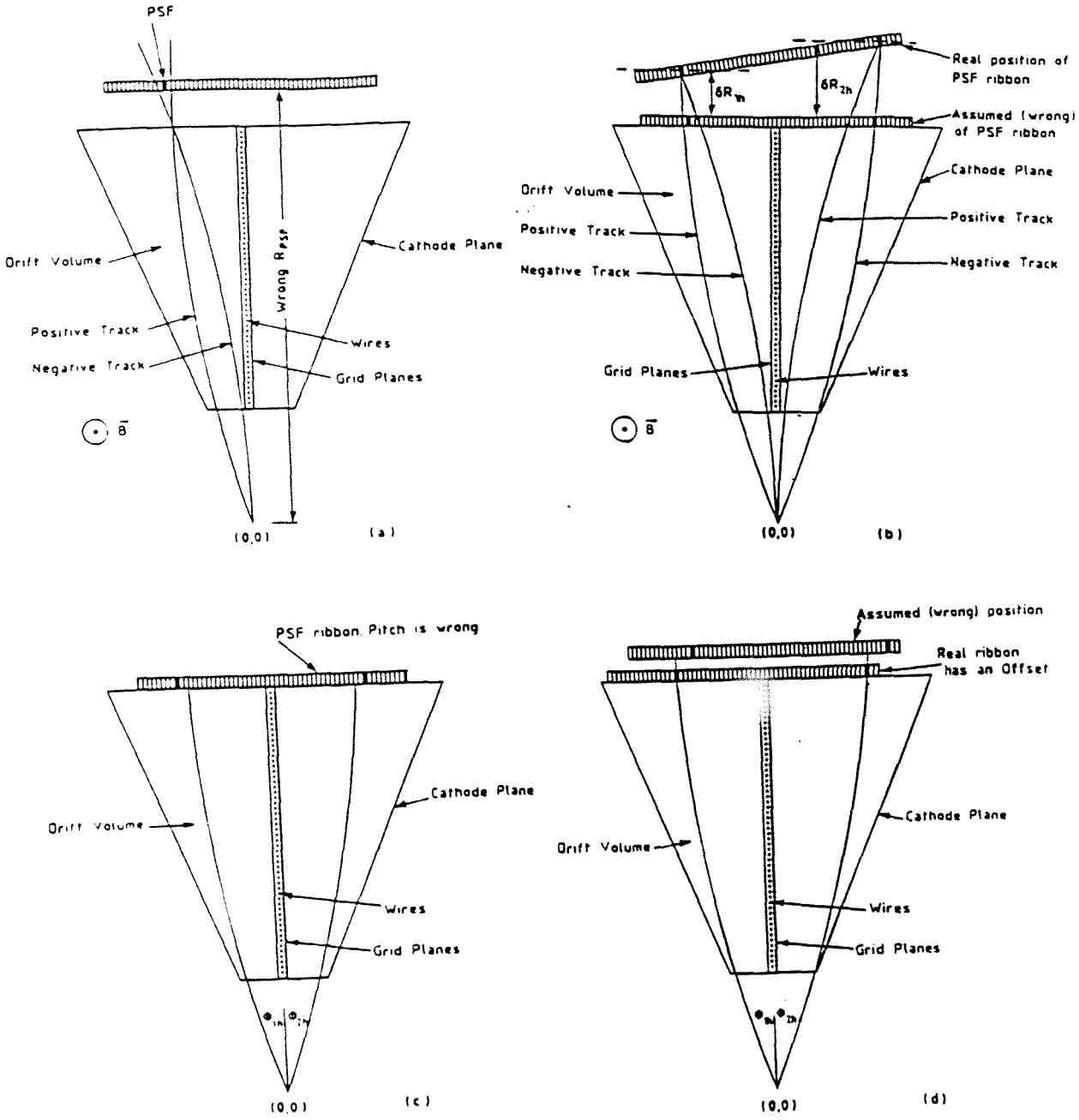

Figure B.8: Schematic $r\Phi$ slice of a TEC sector with the PSF on it to illustrate 4 cases: (a) The Radius is wrong, (b) There is a Slant, (c) The Pitch is wrong, (d) There is an Offset.

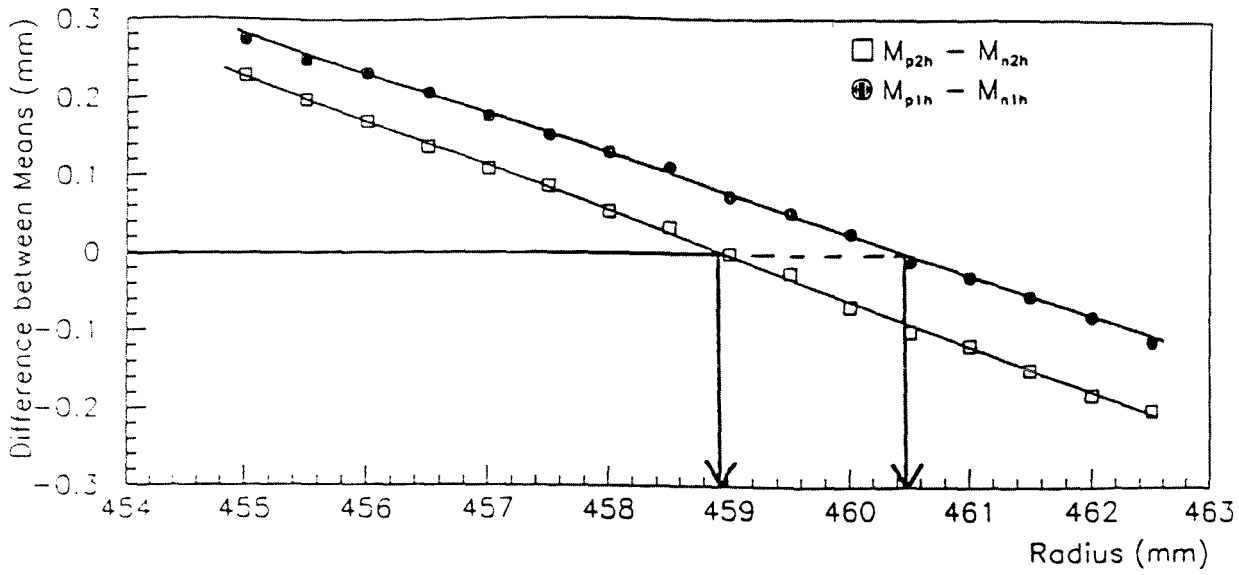

Figure B.9: The difference between the mean values of positive and negative tracks versus the radius used for the two halves of a sector.

B.2.5 Calculation of the Global Offset

Referring to Figure B.8 (d) the correction for the global offset is essentially a shift of the ribbon parallel to itself until the fiber hits on either side of the anode plane lie on top of the tracks. That is if everything else is assumed correct. We will see how under given conditions (wrong pitch or wrongly reconstructed tracks) we cannot assume a perfect track-PSF hit association. In any case the requirement to resolve the global offset is that $M_{n1h} = M_{p1h} = M_{n2h} = M_{p2h}$ in magnitude and in sign, but not necessarily zero. In practice for a given starting value of the global offset and some step size the $M_{n1h} - M_{p2h}$ is plotted as a function of the global offset. A straight line fit is performed and when the difference $M_{n1h} - M_{p2h}$ is zero the global offset is resolved Figure B.12. Of course the other set of data samples can be used and the distribution $M_{p1h} - M_{n2h}$ as a function of the global offset must yield the same answer (since already from the calculation of the radius and the slant the geometry is such that both positive and negative tracks cross the PSF at the same point).

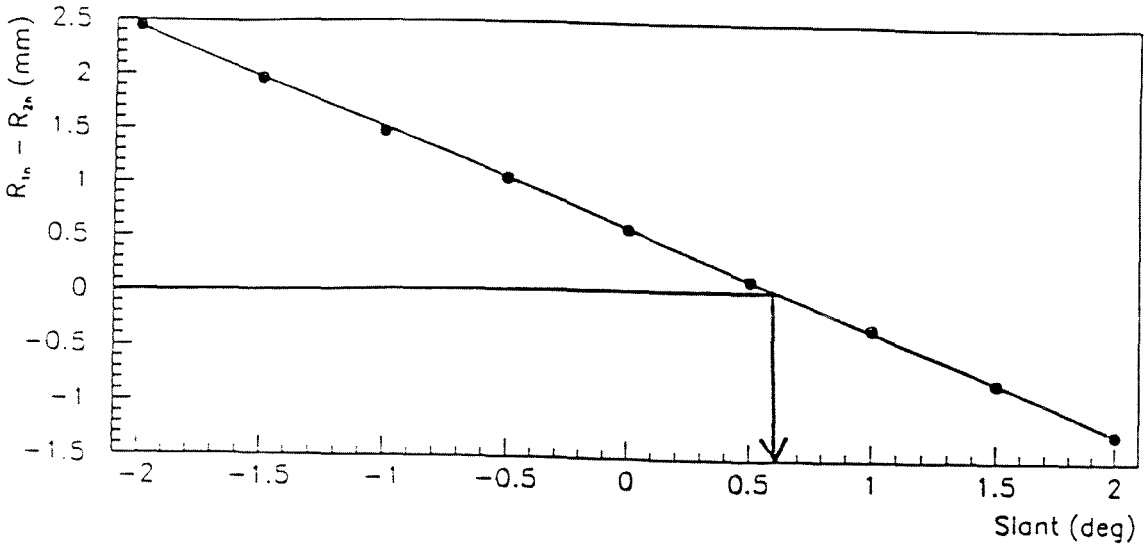

Figure B.10: $R_{1h} - R_{2h}$ as a function of the slant.

B.2.6 Calculation of the Pitch

As explained so far we have used 3 constraints which in the last two subsections have been exploited to derive 3 geometry parameters. Referring to the previous two subsections and Figure B.8 we can summarize :

CONSTRAINT A Demand that $M_{n1h} = M_{p1h}$ *and* $M_{n2h} = M_{p2h}$ *to get* R_{1h} *and* R_{2h}.

CONSTRAINT B Demand that R_{1h} *and* R_{1h} *are equal to get simultaneously the correct radius and the correct slant.*

CONSTRAINT C Demand that $M_{n1h} = M_{p1h} = M_{n2h} = M_{p2h}$ *to get the global offset of the ribbon.*

We need an additional constraint to specify the pitch. It can be that the σ of the resolution plot must be minimum with correct pitch or the final track fiber separation is zero. Both ways are equivalent and not independent. Figure B.13 shows the resolution as a function of the pitch. A parabola is fitted and the pitch is found.

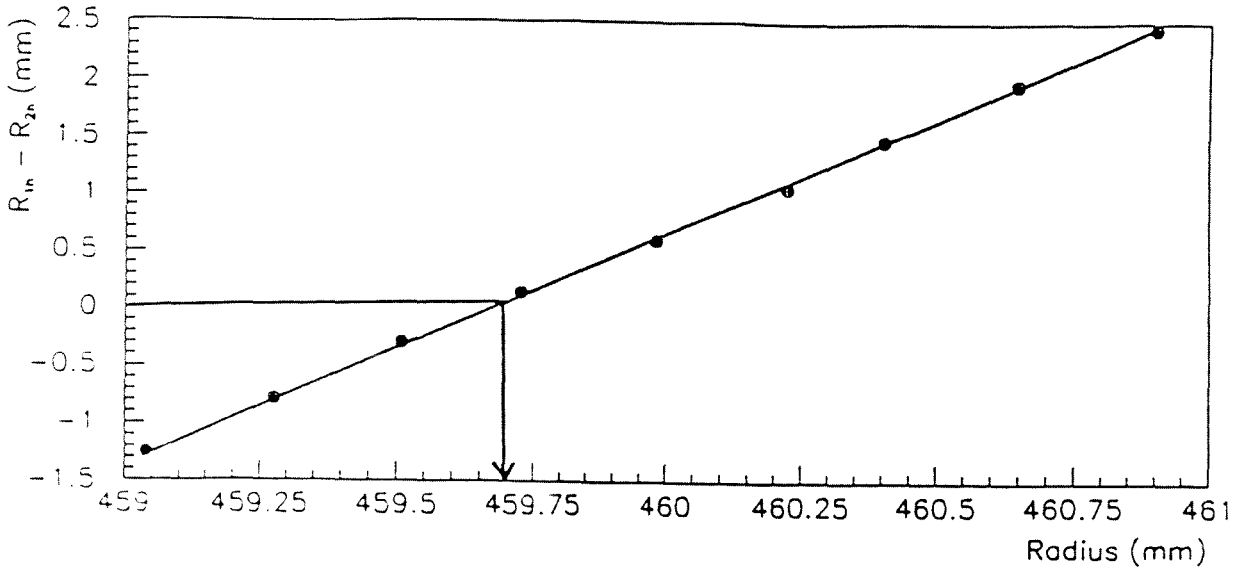

Figure B.11: $R_{1h} - R_{2h}$ as a function of the Radius.

B.2.7 Error estimation

It must be shown that the error on the geometry parameters is less than 0.1 %. There are two sources of error. One is the statistical accuracy of the mean and the σ of the gaussians fitted to the resolution plot. The second is the systematic error on the mean and the σ which comes from the fact that the bins of the resolution plot are repopulated when the constraints of a data sample are changed. Both of these sources of error stay below the 15 μm level, but how this starting error propagates through to the final geometry parameters has to be answered. When stepping through the parameter space to find the solution that gives a consistent answer for all positive and negative tracks, first and second half, we observe the behavior of the same data sample under different constraints. Therefore a usual χ^2 treatment to calculate the errors is not allowed, because any two points on Figures B.9, B.10, B.12 and B.13 are almost completely correlated. The mean of the resolution plots shifts according to the geometry constants imposed every time. Given the behavior of the system at some point in the parameter space, we can predict the next point or points. So treating these points as independent measurements and applying χ^2 statistics is not legitimate. On the other hand

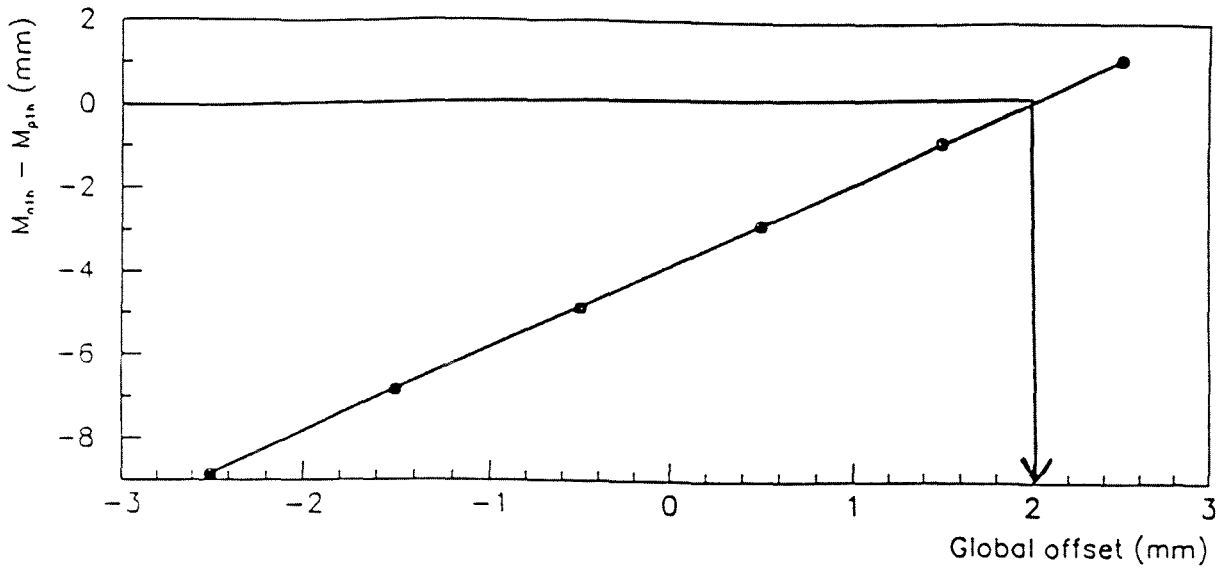

Figure B.12: $M_{n1h} - M_{p2h}$ as a function of the Global Offset.

when we change the constraints we have repopulation of the bins of the fitted resolution plots and this does in fact introduce a small uncertainty in the behavior of one point given the previous one. That is why points in Figures B.9, B.10 and B.12 do not lie exactly on a straight line and Figure B.13 is not exactly a parabola. So from this point of view it is legitimate to use all points in these plots and fit some curve to derive the mean value for the geometry(so that these biases from the repopulation would cancel out). The statistical accuracy of the measurement though is obtained otherwise. The information that has to be used is the statistical accuracy of the fundamental measurement, which is the mean value of the resolution plot (Figure B.8). This error is propagated to the difference of the mean values : $\delta(M_{n1h} - M_{p1h}) = \sqrt{\delta M_{n1h}^2 + \delta M_{p1h}^2} = ; \sqrt{2} \times 15 \sim 20 \mu m$. Then from Figure B.9 an estimate on the radius error can be obtained if $(M_{n1h} - M_{p1h})$ is shifted from zero by 20 μm. Similarly for all quantities used to calculate the geometry. The estimated errors on the geometry parameters are :

For the radius $\longrightarrow \delta R = \pm 0.3$ (mm)

For the slant $\longrightarrow \delta S = \pm 0.3$ (deg)

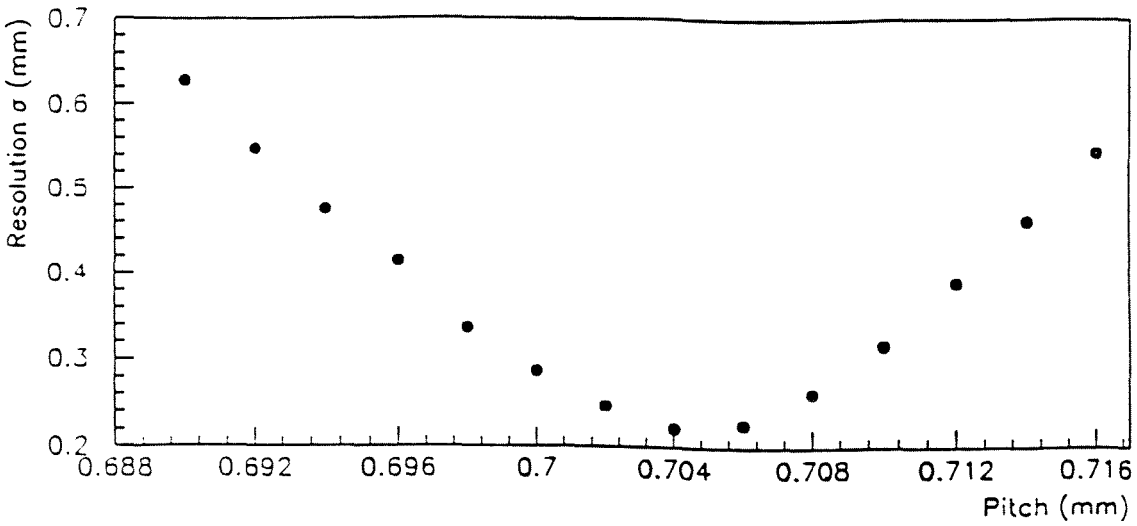

Figure B.13: Resolution as a function of the Pitch.

For the offset $\longrightarrow \delta O = \pm 0.02$ (mm)

For the pitch $\longrightarrow \delta P = \pm 0.0005$ (mm)

B.2.8 Correlation between parameters

The method described determines four geometry parameters. There are six possible correlations between the parameters. It has to be shown that the method is insensitive to these correlations. The geometry parameters are derived one at a time rather than simultaneously. When deriving the radius and the slant the exact value of the pitch and the offset is not assumed. Similarly when calculating the offset the correct value of the pitch is not assumed. In fact not even the radius and the slant need to be known before calculating the offset. The insensitivity of the method to these internal correlations can be understood with qualitative arguments and examples but of course the final test is a check over all parameters with respect to each other. Using real data it will be shown that the method indeed is sufficiently insensitive. This means that in practice the geometry parameters are decoupled sufficiently so that the whole procedure would converge to the same

final answers to the desired 0.1% level of accuracy. Two qualitative examples are presented.

As a first example consider the calculation of the global offset. The result should be the same irrelevant from the pitch :

$$X_{track_{1h}} = Fiber \times Pitch_{real} + Offset$$

$$X_{PSF_{1h}} = Fiber \times Pitch_{assumed}$$

$$X_{track_{2h}} = Fiber \times Pitch_{real} - Offset$$

$$X_{PSF_{2h}} = Fiber \times Pitch_{assumed}$$

So we get :

$$X_{track_{1h}} - X_{PSF_{1h}} = Fiber \times (Pitch_{real} - Pitch_{assumed}) + Offset \ (first\ half)$$

$$X_{track_{2h}} - X_{PSF_{2h}} = Fiber \times (Pitch_{real} - Pitch_{assumed}) - Offset \ (second\ half)$$

If now these equations for the first and second half are subtracted then only the offset is left and the pitch dependence drops out. The result is independent from the pitch because we used the symmetry that exists between the two halves.

As a second example consider the radius and the pitch. The key when calculating the radius is to shift he PSF plane until both positive and negative tracks meet at the same fiber (refer to Figure B.8 (a) and (b)). If the pitch is wrong then a scaled offset is introduced (as in Figure B.8 (c)) but still positive and negative tracks would have the same separation from the PSF hit at the correct radius. The tracks of opposite charge still cross the same fiber and this is the requirement to derive the radius, not to minimize the track-PSF hit distance.

Two other checks were also made. The sensitivity of the method to the efficiency of the fibers across a ribbon and the sensitivity to the low momentum cut imposed on the tracks. It is a fact that along the ribbon there may be dead fibers or fibers that have a bad coupling to the photocathode. Therefore we had to check how the alignment method behaves to such variations of the efficiency. Also even though low momentum tracks are expected to work better since the triangulation is more sensitive, we certainly do not wish a strong dependence on the momentum cut. All these effects were checked and for sector 14 the results are shown in Table B.2, Table B.3, Table B.4: In these tables the fixed parameters are varied by 0.5% from their nominal values. (459.3 mm for radius,0.7 mm for pitch. For offset percent refers to the length of one ribbon and for only absolute comparison can be done). The effect on the measured parameter is observed. We conclude the following concerning the correlations between parameters :

Measured parameters		Fixed parameters		Efficiency	P_t cut (GeV)
Radius (mm)	Slant (deg)	Offset (mm)	Pitch (mm)		
459.7	0.8	0.	0.7	All fibers active	$P_t > 0.5$
459.7	0.7	2.	0.7	All fibers active	$P_t > 0.5$
459.85	0.7	0.	0.7035	All fibers active	$P_t > 0.5$
459.85	0.7	2.	0.7035	All fibers active	$P_t > 0.5$
458.9	0.0	2.	0.7035	All fibers active	$P_t > 2.$
459.9	1.0	0.	0.7	First 35 fibers disabled	$P_t > 0.5$

Table B.2: The dependence of Radius and Slant on all other geometry parameters, the fiber efficiency and the low P_t cut.

Measured parameter	Fixed parameters			Efficiency	P_t cut (GeV)
Global Offset (mm)	Radius (mm)	Pitch (mm)	Slant (deg)		
1.949	459.0	0.7	0.0	All fibers active	$P_t > 0.5$
1.955	459.0	0.7035	0.0	All fibers active	$P_t > 0.5$
1.954	461.3	0.7	0.0	All fibers active	$P_t > 0.5$
1.935	459.0	0.7	0.5	All fibers active	$P_t > 0.5$
1.946	461.3	0.7035	0.5	All fibers active	$P_t > 0.5$
1.959	461.3	0.7035	0.5	All fibers active	$P_t > 2.0$
1.972	459.0	0.7	0.0	First 35 fibers disabled	$P_t > 0.5$
1.947	459.0	0.7035	0.0	First 35 fibers disabled	$P_t > 0.5$

Table B.3: The dependence of Global Offset on all other geometry parameters, the fiber efficiency and the low P_t cut.

Measured parameters	Fixed parameters			Efficiency	P_t cut (GeV)
Pitch (mm)	Radius (mm)	Slant (deg)	Offset (mm)		
0.70296	459.0	0.0	2.0	All fibers active	$P_t > 0.5$
0.70613	461.3	0.0	2.0	All fibers active	$P_t > 0.5$
0.70290	459.0	0.5	2.0	All fibers active	$P_t > 0.5$
0.70627	461.3	0.5	2.0	All fibers active	$P_t > 0.5$
0.70198	459.0	0.0	0.0	All fibers active	$P_t > 0.5$
0.70642	461.3	0.5	2.0	All fibers active	$P_t > 2.0$
0.70283	459.0	0.0	2.0	First 35 fibers disabled	$P_t > 0.5$

Table B.4: The dependence of Pitch on all other geometry parameters, the fiber efficiency and the low P_t cut.

(a) A 0.5% change on the pitch translates in 0.04% change in the radius and practically no change in the slant.

(b) A 0.5% change on the offset has no influence on the radius and the slant.

(c) If the first quarter of the ribbon is assumed dead then the radius is only influenced by 0.05%. The slant changes only by 0.2°

(d) If the low momentum cut is moved from 0.5 GeV to 2.0 GeV then the radius changes by 0.2% and the slant by 0.7°. Some sensitivity therefore to momentum is observed when calculating the radius and the slant. This is understood since tracks with big curvature define more accurately the crossing point at the PSF. It can also be statistical since the 2 GeV momentum cut reduces significantly the sample.

(e) If the radius and the pitch is changed by 0.5% from their nominal value and the slant by 0.5° the offset by only 0.04%. At the same very low level is the sensitivity of the offset calculation to the momentum and the inefficiencies.

(f) The pitch must be calculated last when all other geometry parameters have been fixed to their correct values.

Independent from all above the method does not assume dependence on the acceptance for positive and negative tracks. It does not require same number of positive and negative tracks as long as there are enough for statistical accuracy.

B.2.9 Bias from the track parameters

A final but most important factor that must be examined is the bias introduced when we use tracks. PSF is meant to calibrate TEC and provide drift velocities that will then be used to reconstruct tracks. Instead we assume some drift velocity, we reconstruct tracks and then raise the question :

Can we use those tracks to align PSF and then in a second step recalibrate TEC independent of the initial input V_d?

Of course the aim is an independent, unbiased calibration of TEC. A method attempting to specify the PSF geometry using TEC tracks must be proved unbiased from these TEC tracks. The obstacle is the assumption of the drift velocity V_d. If this drift velocity is overestimated then all tracks would systematically shift

and rotate away from the anode plane. The intersection point of the tracks with the PSF ribbon would also move out. A method attempting to match the fibers with the tracks could be biased from this effect. However it was shown that in this method relative differences are considered rather than absolute minimization. Figure B.14 shows the case when the drift velocity is overestimated and as a consequence the reconstructed tracks shift and rotate outwards. But the radius

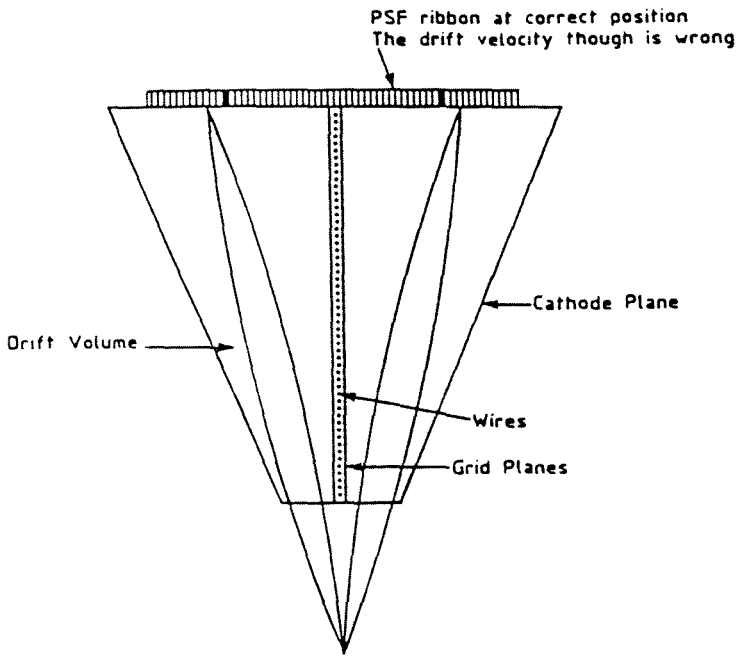

Figure B.14: Schematic $r\Phi$ slice of a TEC sector with the PSF on it.With wrong drift velocity tracks shift and rotate outwards.

would be calculated as before. Positive and negative tracks would still meet at the PSF ribbon,thus yielding the same radius as before. The slant comes from the same principle and is also unbiased. The global offset depends on the displacement on the two halves which cancels out the effect of the drift velocity(exactly in the same way that it cancels out the dependence on the pitch.)We can write :

$$X_{track_{1h}} = Fiber \times Pitch + V_{d_{correction}} + Offset \ (for\ the\ first\ half)$$

$$X_{track_{2h}} = Fiber \times Pitch + V_{d_{correction}} - Offset \ (for\ the\ second\ half)$$

When we subtract those two to get the offset the dependance on the drift velocity goes away. These qualitative arguments have been tested with real data.

We change the drift velocity by a global factor and then reconstruct the tracks. Then the geometry is recalculated. We find that 1.% change in the drift velocity translates to 0.1% bias in calculating the radius, slant and the offset. The only stumbling block is the pitch. The pitch is directly correlated to the drift velocity. It is derived from essentially matching the tracks with the PSF hits. After the other three geometry parameters are specified then pitch is the only reason why the tracks would not exactly match the PSF hits. An overestimated pitch would push all fiber hits outwards on the ribbon. This is exactly the same as if the drift velocity is underestimated and the pitch is right. This becomes more obvious if one compares Figure B.8 (c) where the pitch is wrong and Figure B.14 where the drift velocity is wrong. This direct correlation of pitch to the drift velocity was also shown with real data. A data sample was reconstructed with a drift velocity 0.3% bigger than the nominal one. Assuming that the tracks before reconstruction are the correct ones and that the pitch is right we know already that :

$$X_{track_{before\ reconstruction}} = Fiber \times Pitch$$

After reconstruction it is shown that the tracks actually intersect PSF at a different point 0.3% outwards from where it was previously. That is

$$X_{track_{before\ reconstruction}} - X_{track_{after\ reconstruction}} = 0.3\% \times X_{track_{before\ reconstruction}}$$

This is shown in Figure B.15. The conclusion is that if the pitch is known, then the drift velocity can be varied so that tracks are exactly associated with the PSF hit and the fibers constitute an absolute reference. Otherwise with an error on the global drift velocity and an unknown pitch there is no unique solution. That was one main concern in analyzing the 1990 data. The pitch calculation was done eventually relative to the 1990 data. Given that in 1990 TEC was also calibrated internally to the 0.2% level the pitch is also known at least to this accuracy (systematic error). So in 1991 a relative calibration can be done with respect to the 1990 data (using the pitch found in 1990). There are a few schemes that in principle could be used to obtain an absolute pitch. One is to use very low momentum tracks and then try to see their behavior under changes of the global drift velocity. A second one is try to exploit the fact that the inner part of TEC is asymmetric with respect to the outer part of TEC. If the drift velocity was wrong by a global factor then the tracks would be pulled more in one outer half sector than in its complementary part because the inner TEC has contradicting effects in each outer half. A third scheme is based on the fact that the detection gap does not depend on global changes of the drift velocity inside the drift volume. So far

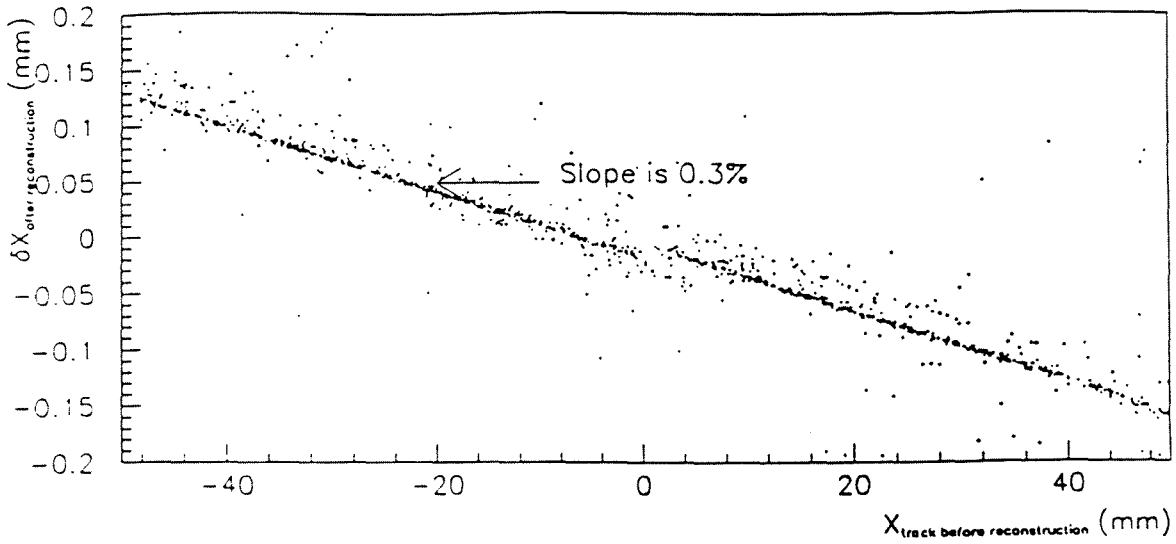

Figure B.15: The shift of the intersection point of the track with the PSF versus the initial distance of the track at the PSF from the anode plane. 0.3% change on the drift velocity translates to a 0.3% shift of the intersection point of the tracks at the PSF.

the above methods were not proved sensitive enough to decouple pitch from drift velocity.

B.2.10 Conclusions and results on the PSF alignment

Table B.5 presents the results from the alignment of the PSF detector. Sectors with severe problems on one half did not yield reliable results. The analysis for those sectors can only be based on one half only. The advantages of the method using both halves are of course lost.

Sector	Radius (mm)	Slant (deg)	Offset (mm)	Pitch (mm)
1	459.50	0.7	1.230	0.7059
2*	459.60	1.0	1.614	0.7054
3*	459.50	0.0	1.075	0.7000
4*	459.50	0.0	1.660	0.7005
5	459.45	1.6	1.096	0.7038
6	459.30	1.0	1.120	0.7020
7*	458.90	0.5	0.630	0.7019
8	459.68	0.0	1.350	0.7038
9	459.95	0.5	0.366	0.7017
10	459.28	0.8	2.245	0.7007
11	459.75	0.8	1.090	0.7038
12	-	-	-	-
13*	459.50	0.0	1.750	0.7034
14	459.95	0.7	1.928	0.7043
15	459.44	0.8	0.920	0.7041
16*	459.50	0.0	1.000	0.7000
17	459.40	0.8	0.920	0.7047
18	459.00	0.6	1.190	0.7033
19	459.90	0.6	1.165	0.7071
20	459.70	0.6	1.350	0.7040
21	460.05	0.6	0.977	0.7038
22	459.20	0.3	2.190	0.7036
23	459.85	0.6	1.587	0.7060
24*	459.60	-0.5	2.095	0.7041

Table B.5: Results from the PSF alignment. Sectors with an asterisk had problems and are less reliable.

B.3 Calibration of TEC using PSF

B.3.1 General considerations

Once we fix the PSF geometry parameters we have an external point which can be used to absolutely calibrate TEC. The starting point is that in the drift volume the drift velocity is :

$$V_d = \frac{Drift\ Distance}{Drift\ Time}$$

The drift time is information that we get directly from the hardware (the FADC's measure the drift time from every pulse). The drift distance is the quantity that must be measured using PSF. There are some internal TEC parameters that inevitably have to be used since PSF only fixes one point on the track. The question that must be answered is how unbiased from those TEC parameters can the PSF calibration be and what is the best way to do the calibration. To study those questions we developed a Monte Carlo to simulate the TEC tracks and the PSF detector. In parallel we reconstructed TEC tracks with different drift velocities to determine the impact on the track parameters that are used in the calibration. These track parameters are (see Figure B.19) :

1. *The distance of closest approach of the track to some reference point, DCA*
2. *The angle of the track with the X axis at the vertex, Φ_{vtx}, or alternatively the curvature of the track $1/R$*
3. *The vertex*

In what follows we describe how the drift distance is obtained using the PSF and the above tracks parameters. From the drift distance and the drift time the drift velocity can be calculated. The analytical expressions for the drift distance are used in the Monte Carlo to test the feasibility and accuracy of various calibration scenarios. Also the results from the reconstruction studies are described. Eventually proposed procedure of calibration will be described.

B.3.2 Calculation of the Drift Distance

STEP 1 (The Lorentz correction)

Figure B.16 shows one TEC outer sector, with a straight track starting from the origin of coordinates and intersecting PSF at a distance X_{PSF} from the anode

plane. In this first step we do not consider the curvature of the track neither the fact that the true vertex is not really the (0,0) point. We only correct for the Lorentz angle(marked as Φ_L on Figure B.16) Without magnetic field the electrons would drift perpendicular to the anode plane. Since though we have a magnetic field, the electrons 'feel' a magnetic force as well perpendicular to the electric force that pulls them towards the anode. The overall motion is not perpendicular to the anode plane but at an angle as shown. We want to express the drift distance of wire 'i' as a function of the PSF coordinate X_{PSF} , the distance of the wire from (0,0) which is r_i (radius of the wire), the radius of the ribbon R_{PSF} and the Lorentz angle Φ_L. Using Euclidean geometry we find :

$$d_1 = \frac{X_{PSF}}{R_{PSF}} \times (r_i - d_i \times \sin(\Phi_L)$$

But also we have :

$$d_1 = d_i \times \cos(\Phi_L)$$

From those two we can solve for d_i and we find:

$$d_i = \frac{X_{PSF} \times r_i}{\cos(\Phi_L) \times (R_{PSF} + X_{PSF} \times \tan(\Phi_L)}$$

This is for the second half of an outer TEC sector. For the first half the Lorentz correction is in the opposite direction and we get:

$$d_i = \frac{X_{PSF} \times r_i}{\cos(\Phi_L) \times (R_{PSF} - X_{PSF} \times \tan(\Phi_L)}$$

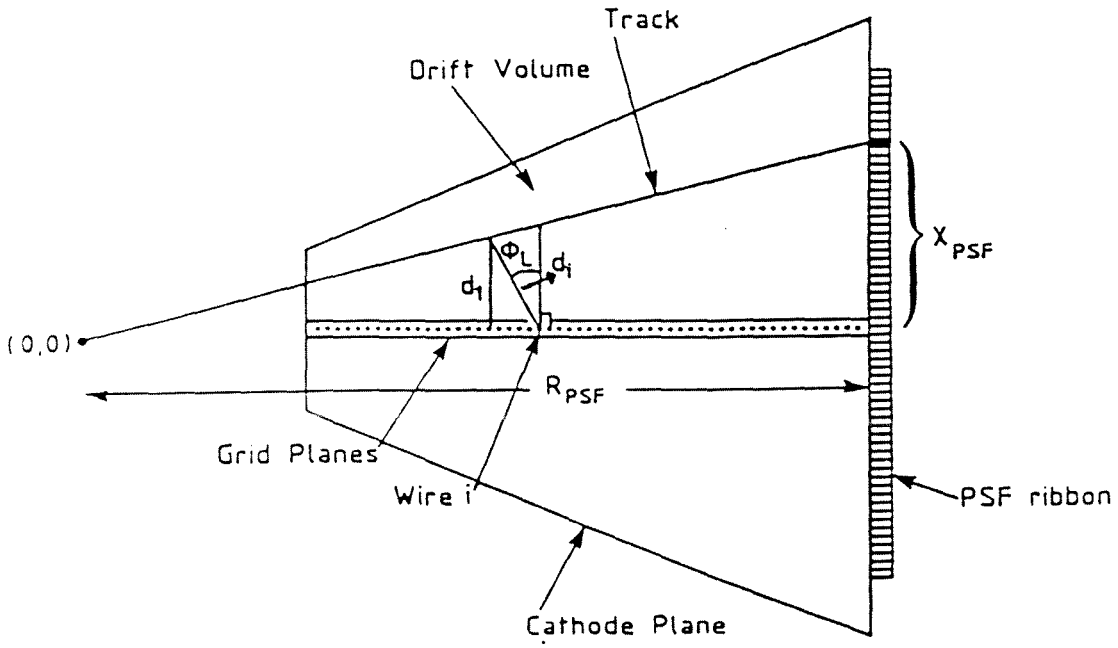

Figure B.16: The Lorentz correction on the drift distance.

STEP 2 (The Lorentz and the Vertex correction)

One step further is to consider a straight track again but now remove the vertex from (0,0) to its real coordinates (X_{vtx}, Y_{vtx}). Figure B.17 shows such a case for the second half again of a TEC outer sector. We can then write:

$$\begin{aligned} X'_{PSF} &= X_{PSF} - Y_{vtx} \quad (definition) \\ R'_{PSF} &= R_{PSF} - X_{vtx} \quad (definition) \\ r'_i &= r_i - X_{vtx} \quad (definition) \\ d_i &= d_3 + d_4 \quad (Total\ Drift\ Distance) \end{aligned}$$

But :

$$d_4 = \frac{Y_{vtx}}{\cos(\Phi_L)} \quad and \quad d_3 = \frac{d_1}{\cos(\Phi_L)}$$

With :

$$d_1 = X'_{PSF} \times \frac{r'_i \overbrace{-}^{Must\ be\ +\ for\ first\ half} d_i \times \cos(\Phi_L)}{R'_{PSF}}$$

We now substitute d_1 in the expression for d_3 and subsequently we substitute d_3,d_4 in the expression for d_i which is the drift distance. So we get:

$$d_i = \frac{Y_{vtx} \times R'_{PSF} + X'_{PSF} \times r'_i}{\cos(\Phi_L) \times (R'_{PSF} + X'_{PSF} \times \tan(\Phi_L)} \quad (Second\ Half)$$

$$d_i = \frac{Y_{vtx} \times R'_{PSF} + X'_{PSF} \times r'_i}{\cos(\Phi_L) \times (R'_{PSF} - X'_{PSF} \times \tan(\Phi_L)} \quad (First\ Half)$$

The vertex can be obtained in three different ways:

(a) From the beam orbit monitors. (measurement independent of TEC)

(b) Calculating the fill vertex using all the tracks in one fill. (measurement dependent on TEC)

(c) Using the reference point and the distance of closest approach to the track,DCA. (measurement dependent on TEC)

For case (c) the vertex is just:

$$X_{vtx} = X_{ref} - DCA \times \sin(\Phi_{vtx})$$
$$Y_{vtx} = Y_{ref} + DCA \times \cos(\Phi_{vtx})$$

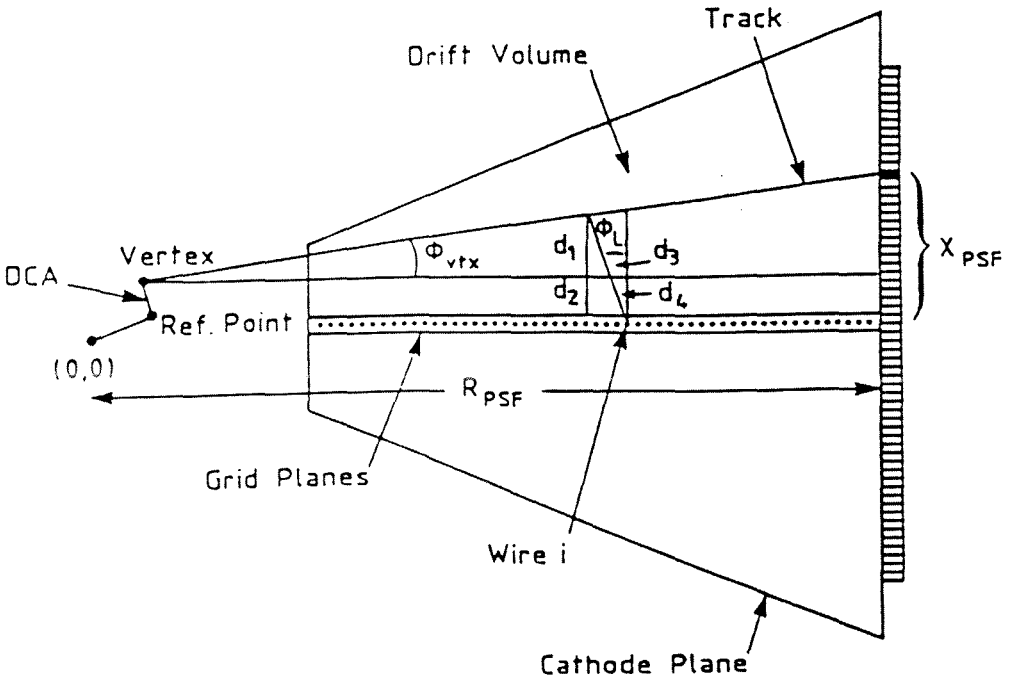

Figure B.17: The Lorentz and the vertex correction on the drift distance.

STEP 3 (The curvature correction)

So far we assumed a straight track. On average there should be the same number of positive and negative tracks per fiber and we could expect that the curvature of the tracks cancels out. But as we will see in the next section this is not true. There is a limited acceptance of positive and negative tracks depending on their momenta and also on the PSF position. This is a purely geometrical effect that was discovered with the Monte Carlo. So we cannot avoid applying the curvature correction. In applying the curvature correction the effort is to minimize the information taken from TEC and maximize the use of the PSF information. A track is a circle that joins the vertex with the PSF. With these constraints we only need one additional to fully specify the problem (Figure B.18). Either the Φ_{vtx} or the radius 'R' can completely constant the track. In this step we focus just on the curvature of the track. Therefore assume that the track starts from (0,0) and also let the Lorentz correction be zero. From Figure B.18 we get:

$$d_i = d_1 + d_2$$

and

$$(x - x_o)^2 + (y - y_o)^2 = R^2 \ (definition\ of\ circle)$$

The center of the circle is just :

$$x_o = R \times \cos(90° - \Phi_{vtx}) = R \times \sin(\Phi_{vtx}) \ (A)$$
$$y_o = -R \times \sin(90° - \Phi_{vtx}) = -R \times \cos(\Phi_{vtx}) \ (B)$$

We can find d_1 (Figure B.18):

$$d_1 = \sqrt{R^2 - (r_i - x_o)^2} + y_o - d_2$$

And so :

$$d_i = \sqrt{R^2 - (r_i - x_o)^2} + y_o \ (C)$$

This formula gives the drift distance corrected for the track curvature, only it does not involve at all the PSF. Since, as mentioned above, the problem is fully constrained with just the PSF information and the Φ_{vtx},DCA, we can transform the radius to an expression involving the Φ_{vtx} and the PSF only. From Figure B.19 we get :

$$OP = \sqrt{R_{PSF}^2 + X_{PSF}^2}$$

Also :

$$OP = 2 \times R \times \cos(\omega)$$

And :

$$\omega = (90° - \Phi_{vtx}) + \arctan(\frac{X_{PSF}}{R_{PSF}})$$

So solving for R we get :

$$R = \frac{\sqrt{R_{PSF}^2 + X_{PSF}^2}}{2 \times \sin(\pm \Phi_{vtx} \mp \arctan(\frac{X_{PSF}}{R_{PSF}})}$$

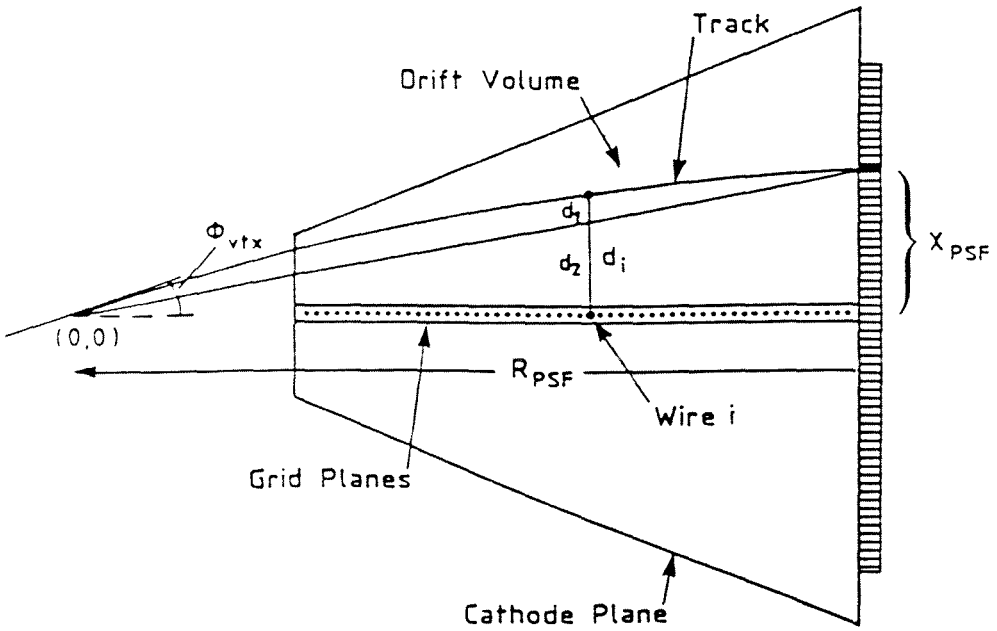

Figure B.18: The Curvature correction on the drift distance.

Where $(+,-),(-,+)$ *correspond to positive/negative tracks respectively.* Now we can substitute the expression for R in (A),(B),(C) above and solve for the drift distance as a function of the PSF radius 'R_{PSF}',the radius of the wire 'i' r_i that we are concerned with, the angle of the track with the X axis at the vertex 'Φ_{vtx}' and the distance X_{PSF} of the fiber hit from the anode plane. The curvature correction is very important and not negligible inside the 0.5 T magnetic field at $L3$. Even a high P_t cut would leave a data sample with almost straight tracks. The curvature correction (the extra distance needed along the drift direction to account for the curvature of the track) as a function of wire number for different momenta ranges is shown in Figure B.20

STEP 4. Total correct drift distance

In the last three steps the various corrections, in calculating the drift distance, were derived. The corrections were treated separately in order to point out the source of every correction and to make the procedure more transparent. However combining the correction together in one analytical expression involves more algebra and here the final analytical expression is displayed for completeness. To summarize corrections were made for:

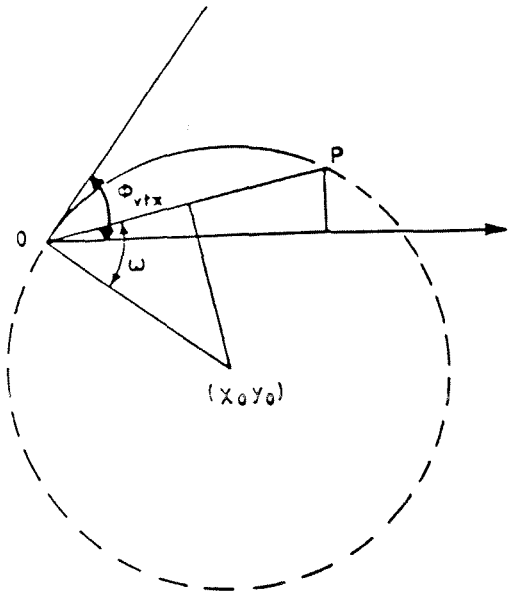

Figure B.19: Transforming the radius of a circle as a function of the Φ_{vtx} and the PSF.

1. *The Lorentz angle.*
2. *The Vertex position.*
3. *The nonzero track Curvature.*
4. *The Slant of the PSF ribbon with the anode plane.*

Figures B.19 and B.21 were used to derive the following expressions. Figure B.21 shows how we can transform the global vertex coordinates to the local coordinate system of a sector, were the X axis is the anode plane and the Y axis perpendicular

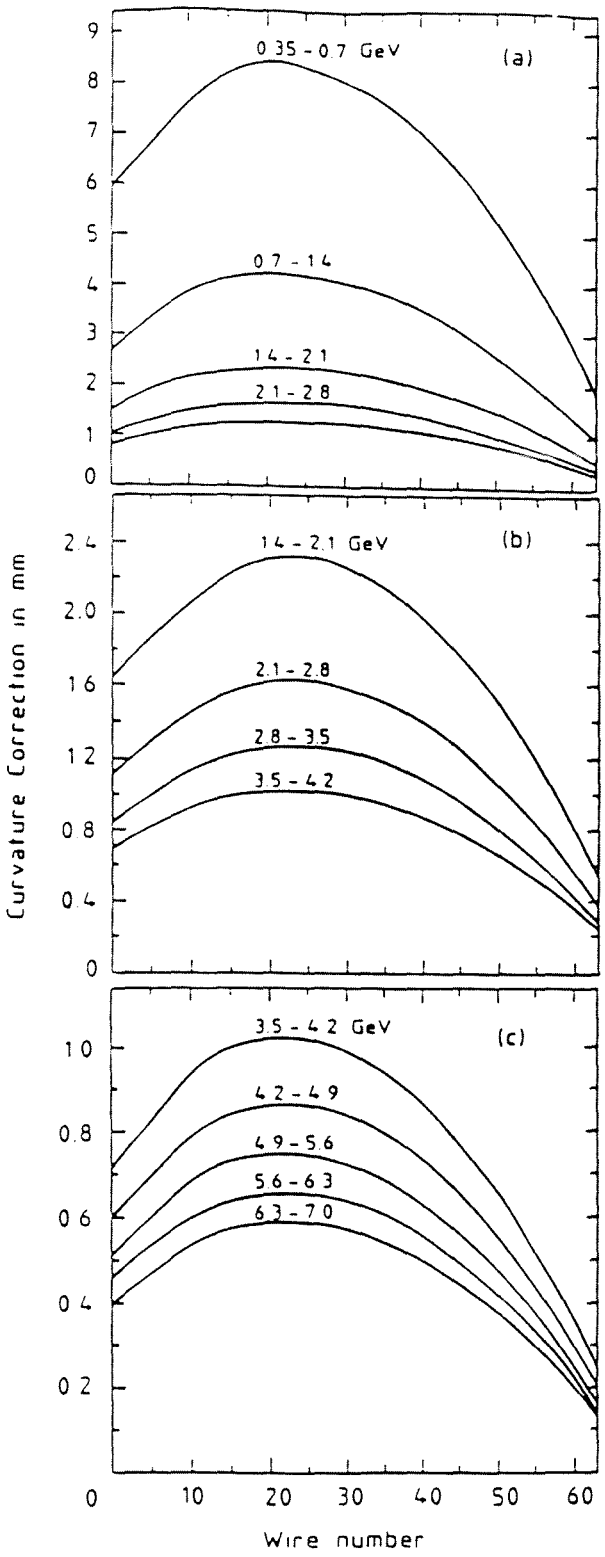

Figure B.20: Curvature correction as a function of wire number for various momentum ranges.

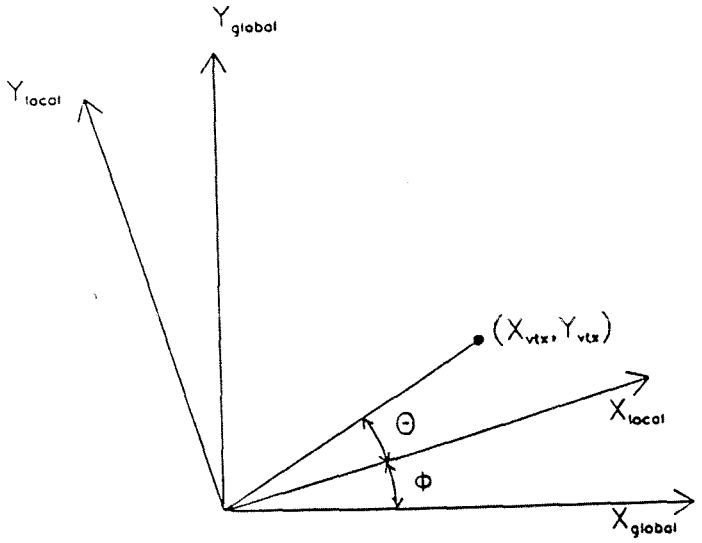

Figure B.21: Transformation of the vertex coordinates to the sector local coordinate system.

to that :

$$\begin{aligned}
\Phi &= n_{sector\ number} \times \Phi_{sector} + \frac{\Phi_{sector}}{2} \\
\theta &= \arctan\left(\frac{Y_{vtx}}{X_{vtx}}\right) - \Phi \\
r &= \sqrt{X_{vtx}^2 + Y_{vtx}^2} \\
X_{vtx\ local} &= r \times \cos(\theta) \\
Y_{vtx\ local} &= r \times \sin(\theta)
\end{aligned}$$

Now that the vertex is specified in the local (sector) coordinate system we proceed by moving the local origin from (0,0) to $X_{vtx\ local}$, $Y_{vtx\ local}$:

$$R'_{PSF} = (R_{PSF} - X_{PSF} \times \overbrace{\sin(\beta)}^{\beta \text{ is the slant}}) - X_{vtx\ local}\ (Radius\ of\ PSF)$$

$$X'_{PSF} = X_{PSF} - Y_{vtx\ local}\ (Distance\ of\ fiber\ from\ anode\ plane)$$

$$r'_i = r_i - X_{vtx\ local} \overbrace{\pm}^{+/-\ for\ Second/First\ half} \tan(\Phi_L \times Y_{vtx\ local})\ (Position\ of\ wire)$$

Also define :

$$A = \frac{\sqrt{R'^2_{PSF} + X'^2_{PSF}}}{2 \times \sin(\Phi_{vtx} - \arctan(\frac{X'_{PSF}}{R'_{PSF}}))}$$

$$B = \times \sin(\Phi_{vtx})$$

$$C = A \times \cos(\Phi_{vtx})$$

$$D = (r'_i - B)$$

$$E = (1 + \tan^2(\Phi_L))$$

$$F = C \overbrace{\mp}^{-/+\ for\ Second/First\ half} r'_i \times \tan(\Phi_L) \overbrace{\pm}^{+/-\ for\ Second/First\ half} B \times \tan(\Phi_L)$$

$$G = C^2 - A^2 + D^2$$

Eventually we arrive at the expression for the total drift distance with all corrections included. This expression is true for all wires in outer TEC sectors. The anode plane of an inner TEC sector is just rotated with respect to the outer TEC sector.

$$d_{Total\ Drift\ Distance} = \frac{-F + \overbrace{\pm \times \pm}^{+/-\ for\ Pos./Neg.\ and\ Second/First\ half} \times \sqrt{F^2 - E \times G}}{E \times \cos(\Phi_L)}$$

The last formula is the full drift distance using the PSF information ,the vertex and is also using Φ_{vtx}. There is no a priori reason why Φ_{vtx} or R should be used. Algebraically these two are exactly and we should be able to transform the above equation in one that uses the PSF information, vertex and the radius R of the track. The easier way to do this is to express the center of the circle (the track) as a function of the fiber position, the vertex and the radius R of the track. Then we can find the intersection point of the track with the drift direction and from that the drift distance. The algebra is elaborate but straightforward and is not repeated here. In reality one parameter might be better to use than the other in terms of sensitivity. If we assume an uncertainty on the drift velocity that was used to reconstruct these tracks, then how does this translates into an error for Φ_{vtx} and R? We tested both and found that the radius R is less biased.

B.3.3 The Drift Distance Drift Time relation (DDT)

Once the drift distance is known we can plot it as a function of the drift time for every wire. This results to a distribution that can be fitted to a straight line whose slope is the drift velocity for that wire. In Figure B.22 we see the DDT for Sector 14 wire 57. There is a 0.1 GeV low momentum cut, but the distribution is very narrow since the curvature correction was taken into account. Figure B.23 shows sector 14 wire 20 but the drift distance was calculated assuming straight tracks. The width of the DDT depends on the low momentum cut, if there is no curvature correction. Within the drift volume the DDT relation should be linear and the

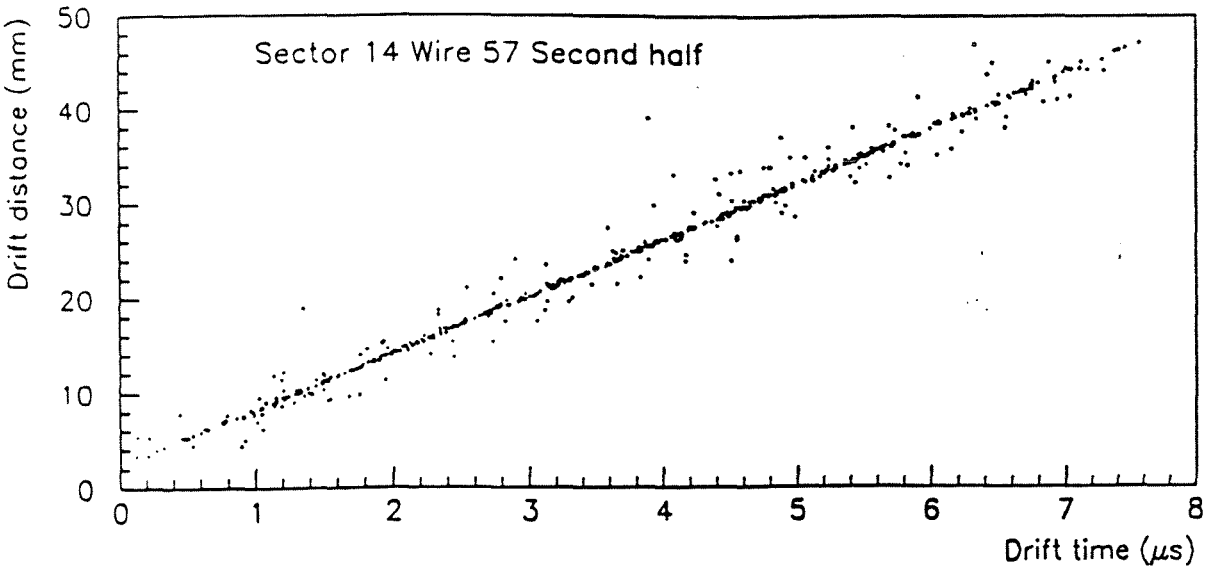

Figure B.22: Drift Distance versus Drift Time. The full drift distance with all corrections is used.

drift velocity is the slope of the fitted line. In the next section the complications of a DDT without any curvature correction. will be described. here the importance of the fitting algorithm is pointed out.

The PSF noise level is small but not negligible. Also there are cases that we get a false FADC reading. Then on the DDT distribution we get tails that must not be fitted. The drift velocity must be accurate to the 0.1% level and such tails

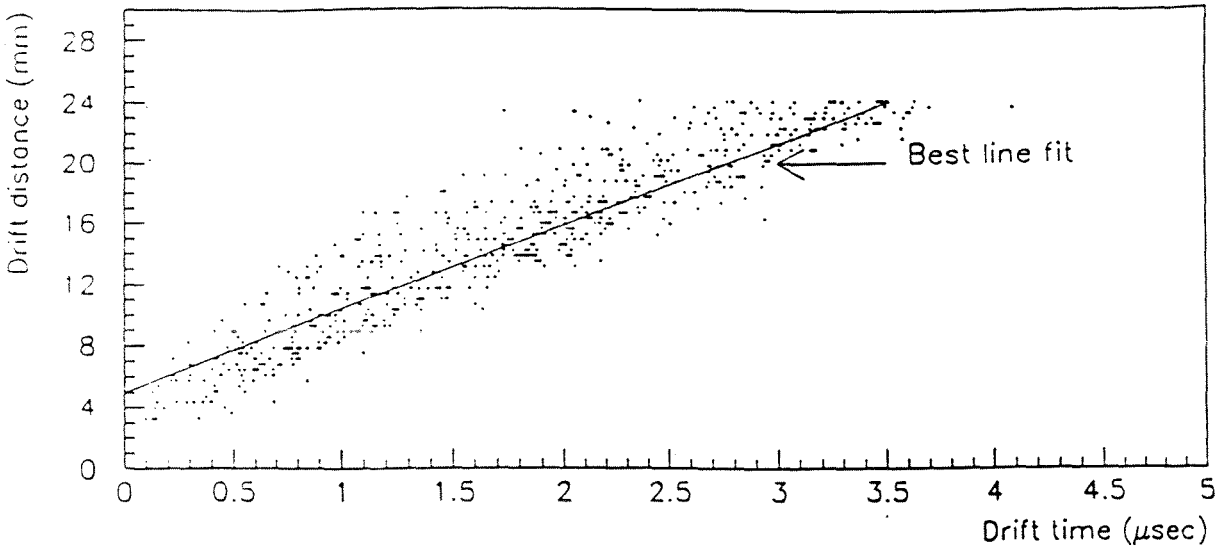

Figure B.23: Drift Distance versus Drift Time. Tracks are assumed to be straight. Notice that the distribution is no longer a straight line.

should be treated carefully or the fit could be biased. Every point on the DDT distribution is one independent measurement and the error on those points was assumed to be the average PSF resolution for the Drift Distance and zero for the drift time (because the error from the FADC's that give the time is less than 1 ns) It will be discussed why the starting value for the error on the drift distance is irrelevant. The method that was developed to fit the DDT relation comprises the following steps:

There are two different sources of noise. One is the random uncorrelated noise coming from the electronics or an occasional bad reading from the FADC's The second source of noise may come from a systematic hardware problem resulting in a separate DDT relation away from the true one (for example tube misalignment). We start with the assumption that the 'noisy' points on the DDT plot are more isolated and with a smaller probability density than the 'good' points. This assumption is of course justified from the excellent signal to noise ratio. The probability density is calculated for every point. A simple way of doing that is to divide the DDT plane in squares with a size proportional to the resolution in time

and distance. Then we count the number of points in such a square and divide with the total number of points on the whole DDT plane. In this way we get a density per square. It was shown with Monte Carlo that the method is efficient to all but the worst cases were the noise is more than the signal.

The function minimized is :

$$FUN = \sum_{i=1}^{n} \frac{(d_i - (v_d \times t_i + c))^2}{\sigma_i^2}$$

where n is the total number of points on the DDT plot and (d_i, t_i, σ_i) is the drift distance, drift time, error on the i_{th} point respectively. The error on every point on the DDT distribution is weighted according to its probability density (the probability density of the square it belongs). When the $\mathcal{X}^2$ fit is performed the 'noisy' points do not bias the fitted line because their weights have been minimized accordingly. In this first iteration no points are cut. The aim is just to get a first unbiased mean value for the slope of the DDT distribution.

The fit is iteratively repeated excluding every time points that are more than 3σ away.The iteration stops when there are no more points excluded ,or when the Confidence Level of the fit is 95% ,or when the number of iterations exceeded an upper limit. In most cases the above procedure converges.

After convergence there is one last iteration with no new points excluded this time, normalizing correctly the errors. The errors of the fitted points are reset to their nominal values and scaled according to the value of $\frac{\mathcal{X}^2}{Degrees\ of\ freedom}$ after the last fit. This is done to get meaningful error analysis. The fitting package used is MINUIT from the CERN program library. The parabolic error obtained on a fitted parameter is the value by which if we increase or decrease the parameter it would increase the function FUN that was minimized by one. In order for this error to be meaningful the function that was minimized must have been properly normalized. To properly normalize the function under minimization the default weights must be scaled by $\frac{\mathcal{X}^2}{Degrees\ of\ freedom}$ (from the last iteration). Then the DDT distribution is fitted one more time and the parabolic error correspond now to the one σ statistical error on the drift velocity. As a check, on the selected points that survive the fitting iterations, one can fit analytically a straight line. The mean values as well as the errors agree with the ones obtained from MINUIT. Also for sectors with adequate statistics the data sample was split and every smaller data sample was fit to obtain drift velocities. The σ of the distribution of the drift velocities which concern the same wire from different subsamples is yet another way to estimate the error on them.

B.3.4 Monte Carlo and Reconstruction Studies

A Monte Carlo was written to simulate tracks that cross the PSF. With the Monte Carlo studies we were able to better understand many points on the whole scheme of the calibration of TEC using PSF and to discover some completely new effects. In particular:

(1)Statistical accuracy with the PSF calibration

The statistical accuracy versus number of tracks used is shown in Figure B.24. With about 1,000 tracks the error is better than 0.1%

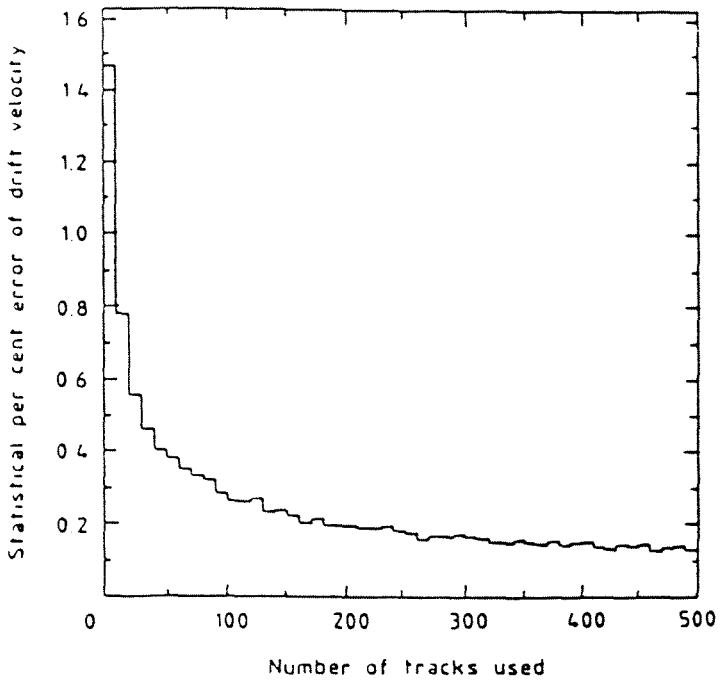

Figure B.24: Statistical accuracy on the calibration versus number of tracks.

(2) Why a calibration without the curvature correction is not feasible.

If on the average we get the same number of positive and negative tracks per fiber then, one might think, that the effect from the curvature of the tracks will cancel out. The drift distance could be considered as the intersection point of the line along the drift direction with the line joining PSF hit and the vertex (just Lorentz and vertex correction). The benefit of such an approach is that no TEC

dependent parameters are involved and such a calibration would be completely unbiased. However there are two main problems in such an approach:

1. *The number of positive tracks per fiber is not the same as the number of negative tracks. There is a limited acceptance for positive and negative tracks which is a function of the position along the PSF ribbon and of the track momenta.*

2. *The DDT distribution gets very wide and any linear fit fails.*

Low momenta tracks that end up at the PSF close to the edge or the middle of the ribbon, have to cross the cathode plane or the detection gap. The detection efficiency is much lower. The hardware is much less efficient and the reconstruction algorithm as well. In a simplified model we can assume that no tracks are reconstructed if they cross the detection gap or the cathode plane. Then we can plot distance along the PSF plane versus P_t. That is for positive tracks what is the maximum distance and for negative what is the minimum distance along PSF as a function of the momentum. This is shown in Figure B.25. We can clearly see that any assumption of negative tracks canceling out the effect of positive tracks is wrong at least for low P_t.

The second problem assuming tracks being straight on the average is that the width of the DDT distribution biases any linear fit to a wrong . Exactly how the fit algorithm would behave under such conditions is not a priori known. But Monte Carlo studies showed that all drift velocity values are biased to lower values. We can see that in Figure B.23 were the DDT distribution is shown along with the fitted line. We can qualitatively understand this because the line that minimizes its distance from the fitted points does not run through the middle of the band but along the diagonal. Those two effects showed clearly that any calibration to be reliable had to take into account the curvature of the tracks.

(3) Including the curvature correction how biased are we to the track parameters?

The full analytical expression of the drift distance includes the curvature correction. This correction inevitably involves the track parameters(such as Φ_{vtx}) ,because there is no way to specify the trajectory of a track with just two constraints(that is the PSF and the vertex). A third constraint is needed and this can be Φ_{vtx} or the radius R of the track. Given now that these parameters come out from the track fitting algorithm how much are they biased from a wrong starting drift velocity?

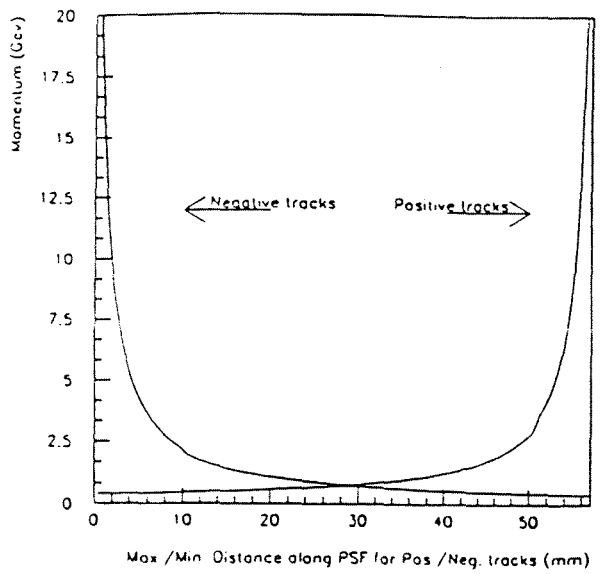

Figure B.25: Momentum versus distance along the PSF. The acceptance of PSF for positive and negative tracks is shown.

Consequently how does this error on Φ_{vtx} or R translate to the drift distance and to the drift velocity calculation using the PSF? To answer this question tracks were reconstructed with a global offset on the nominal drift velocity. Then the new tracks are compared with the original ones. In Figure B.26 the percent change on Φ_{vtx} is shown for a 0.3% increase on the drift velocity. The value of Φ_{vtx} was then smeared in the Monte Carlo. The calculated drift distances and drift velocities show a clear dependence on Φ_{vtx}. The initial 0.3% on the starting drift velocity propagated through to a 0.15% on the drift velocity calculated using PSF and Φ_{vtx}. The result was verified with real data in the beginning of 1991 physics run period. The default drift velocity was 0.8If the calibration is done with PSF and Φ_{vtx} the results are clearly biased. If however the radius R of the track is used instead of Φ_{vtx} such a bias is eliminated. Figure B.27 shows the drift velocities for outer sector 22 first half, versus wire number. The solid line is the drift velocity value after the internal calibration with Bhabhas. The line indicates were the nominal value is (this value was increased by 0.8%. Drift velocities calculated using Φ_{vtx} are biased as can be seen. Concluding PSF calibration does not seem to be biased

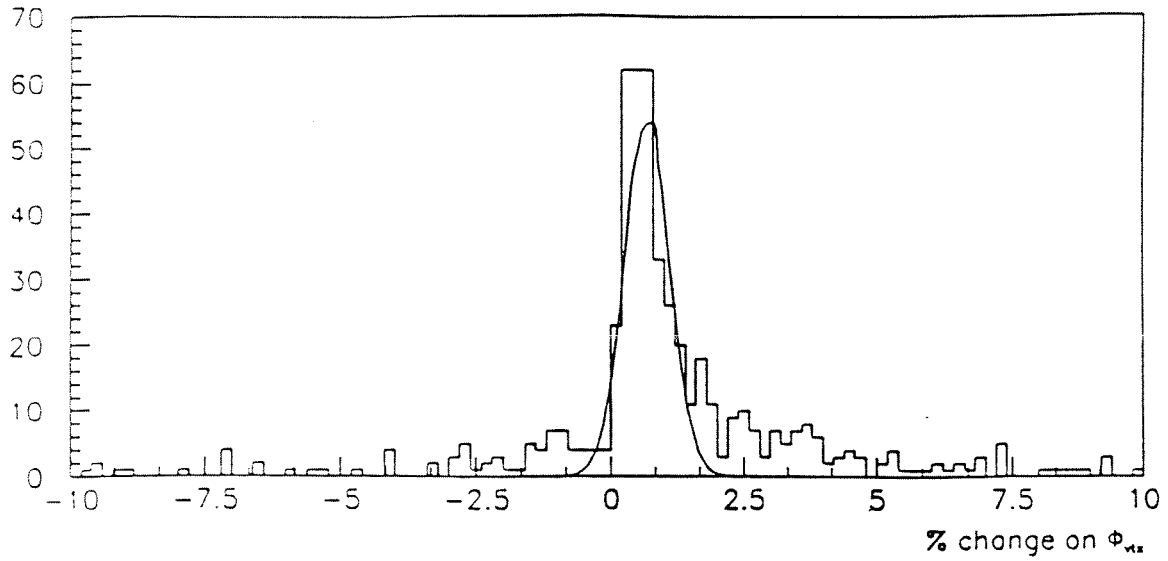

Figure B.26: Percent change on Φ_{vtx}. Tracks were reconstructed with 0.3% overestimated drift velocity. The distribution has a mean of 0.6% which shows a very strong dependence of Φ_{vtx} on the drift velocity.

from wrongly reconstructed TEC tracks if the correct parameter (radius R) is used in conjunction with the PSF.

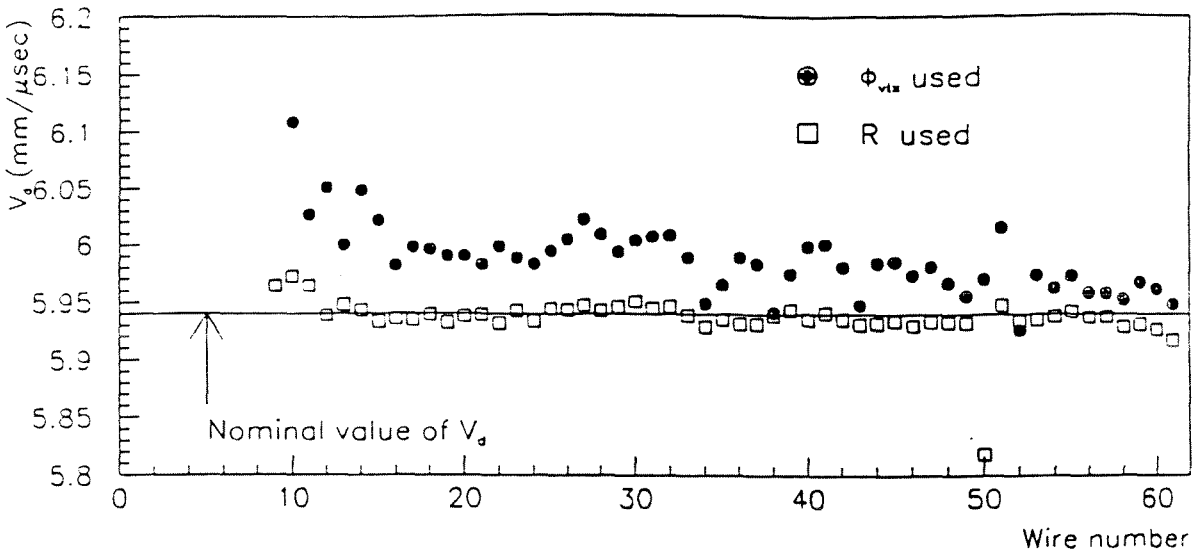

Figure B.27: Drift velocity versus wire number. The PSF calibration using the radius of the track rather than the Φ_{vtx} is sufficiently insensitive.

B.3.5 Conclusions

With PSF we can do the drift velocity calibration of TEC globally and on a wire by wire bases. If PSF is fixed then it is an external to TEC point and can provide the absolute calibration. As mentioned on Section 3.4 (last paragraph) a global change on the drift velocity translates linearly in a shift of the intersection point of the track with the PSF ribbon. In fact this means that we can detect such changes by varying the pitch until the tracks match the PSF hits. If we know the true pitch then we simply have :

$$X_{track\ at\ the\ PSF} - X_{track\ at\ the\ PSF_{true}} = \frac{\delta v}{v} \times X_{track\ at\ the\ PSF_{true}}$$

But :

$$X_{track\ at\ the\ PSF_{true}} = (fiber\ number) \times pitch_{true}$$

$$X_{track\ at\ the\ PSF} - X_{track\ at\ the\ PSF_{true}} = (fiber\ number) \times (pitch - pitch_{true})$$

Combining the three above equations we get:

$$\frac{\delta v}{v} = \frac{pitch - pitch_{true}}{pitch_{true}}$$

We need about 7,000 hadronic events to acquire 0.1% statistical accuracy on the global drift velocity. With LEP luminosity this is a few days run. In that sense it is very important that using PSF we can monitor the tracking detector on L3 on a regular basis and with minimum computing power. For 48 half sectors only one hour (real Apollo cpu time) is needed to find the global drift velocity.

From the DDT relations we can also get the single wire drift velocities. Figure B.28 shows outer sector 14 first half. Figure B.29 shows outer sector 17 first half. Notice the peak around wire 24 which is due to grid plane problem (the grid plane if not properly grounded does not protect the low amplification region from the detection gap where the avalanche is created). With PSF such hardware

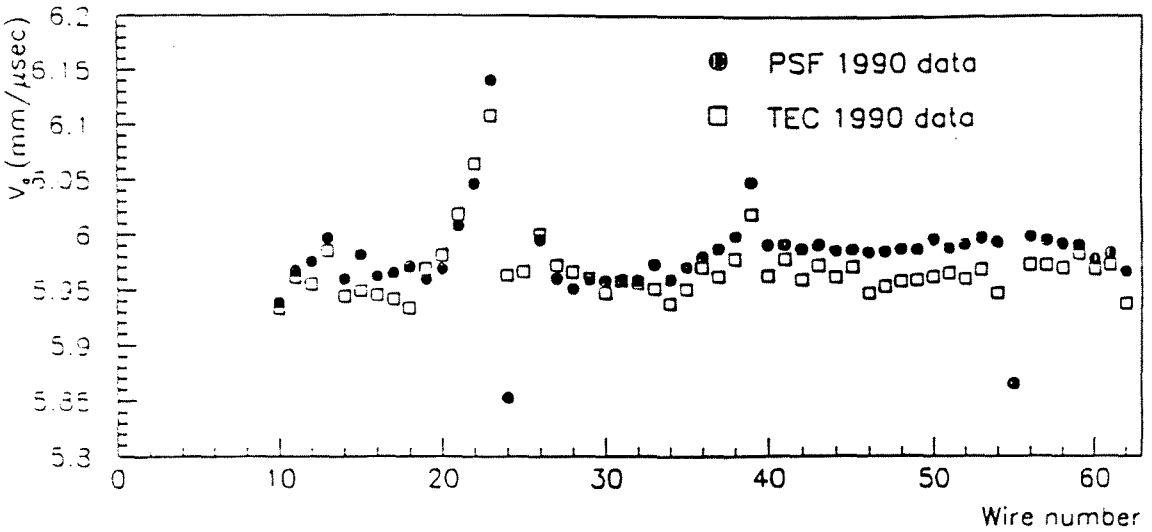

Figure B.28: Drift velocity versus wire number for Sector 14 first half. Comparison is done with the calibration constants from the TEC internal calibration.

problems can be detected. About 20.000 hadronic events are needed to acquire 0.1% statistical accuracy on the single wire calibration.

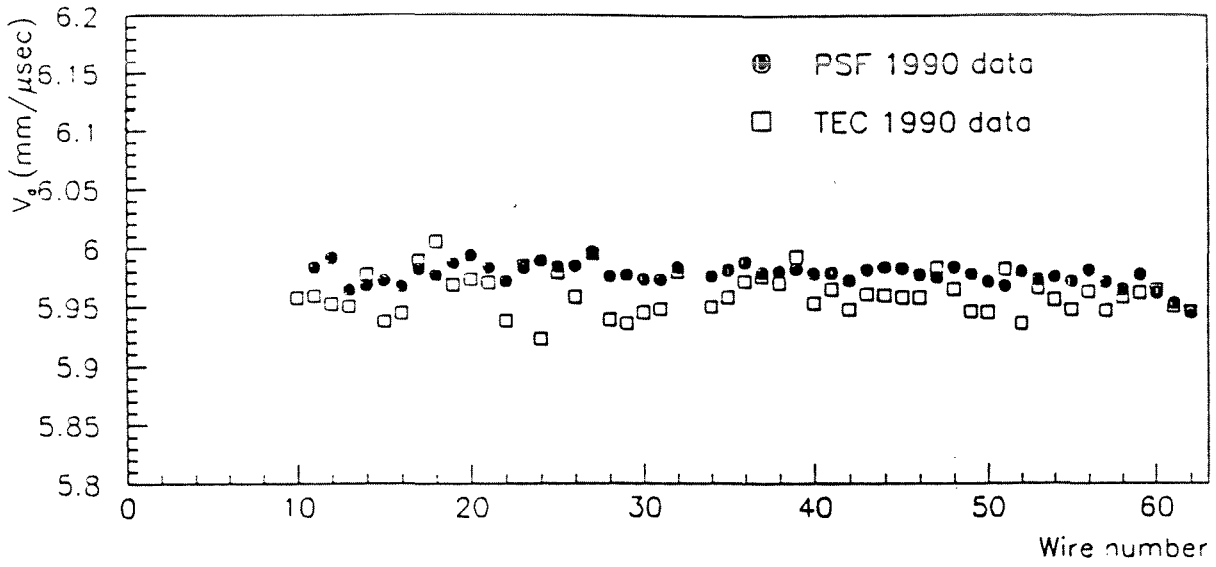

Figure B.29: Drift velocity versus wire number for Sector 17 first half.

Bibliography

[1] H. Goldstein,Classical Mechanics, Addison-Wesley Press, Cambridge, Mass. (1951).

[2] S. L. Glashow, Nucl. Phys. **22** (1961) 579;
S. Weinberg, Phys. Rev. Lett. **19** (1967) 1264;
A. Salam, "Elementary Particle Theory", Ed. N. Svartholm, Stockholm, "Almquist and Wiksell" (1968), 367.

[3] F. Halzen & A. MARTIN, Quarks & Leptons, John Wiley & Sons (1984).

[4] I.J.R. Aitchison & A.J.G. Hey, Gauge Theories in Particle Physics, Adam Hilger (1989).

[5] J.J. Sakurai, Advanced Quantum Mechanics, Addison-Wesley Press, (1987).

[6] D.H. Perkins, Introduction to High Energy Physics, Addison-Wesley Press(Third edition).

[7] F.A. Berends &R. Gastmans, Nucl. Phys. **61B** (1973) 414-428.

[8] F.A. Berends and R. Kleiss, Nucl. Phys. **186B** (1981) 22.

[9] A. Litke, Harvard Univ., Ph.D Thesis (1970) unpublished.

[10] F.E. Low, Phys. Rev. Lett. **14** (1965) 238 ;
R. P. Feynman, Phys Rev. Lett. **74** (1948) 939 ;
F. M. Renard, Phys Lett. **116B** (1982) 264.

[11] S. Drell, Ann. Phys. (N.Y.) **4** (1958) 75.

[12] A. Pilaftsis Institut für Physik Johannes Gutenberg-Universität, Mainz, FRG, Private communication.

[13] ALEPH Collab., D. Decamp et al., (1991) CERN-PPE/91-149

[14] L3 Collab., B. Adeva et al., Phys. Lett. **250B** (1990) 199

[15] OPAL Collab., M. Z. Akrawy et al., Phys. Lett. **257B** (1990) 531.

[16] ALEPH Collab., D. Decamp et al., Phys. Lett. **236B** (1990) 501.

[17] L3 Collab., B. Adeva et al., Phys. Lett. **247B** (1990) 177

[18] OPAL Collab., M. Z. Akrawy et al., Phys. Lett. **244B** (1990) 135.

[19] See "Rare Decays", I.J. van der Bij and E.W.N. Glover (Conveners), in Z Physics at LEP 1, CERN Yellow Book, 1989, edt by Altarelli, R. Kleiss and C. Verzegnassi.

[20] F. M. Renard, Phys. Lett. **116B** (1982) 269 ;
M. Bardadin-Otwinowska, CERN-PPE/92-6 (1992)

[21] M. Baillargeon, F. Boudjema,"New Physics Through Final State Photons", to be published, CERN-Yellow-Book "Photon Radiation from Quarks"

[22] C. N. Yang, Phys. Rev. **77**, (1950) 242.

[23] M. Jacob,T. T. Wu, Phys. Lett. **232B** (1989) 529.

[24] G. B. West, Mod. Phys. Lett. **5A** No. 27 (1990) 2281.

[25] S. Ghosh, D. Chatterjee, Mod. Phys. Lett. **5A** No. 19 (1990) 1493.

[26] L3 Collaboration, B. Adeva et al., Nucl. Instr. and Meth. **A289** (1990) 35.

[27] H. Akbari et al., Nucl. Instr. and Meth. **302A** (1991) 415-426;
G. Alverson et al., *L3* Note 1105. February 19, (1992);
J. Bao, Johns Hopkins University, Ph.D. Thesis (1992).

[28] L3 Collaboration, B. Adeva et al., Z. Phys. **51C**, (1991) 179.

[29] L3 Collaboration, B. Adriani et al., CERN-PPE/92-87 (1992)

[30] DELPHI Collab., P. Abreu et al., CERN-PPE/91-109 (1991)

Vita

Constantinos E. Spartiotis was born in Athens, Greece on 1964. He received his Bachelors degree from The University of Athens, Department of Physics and Astronomy in 1987. In the same year, he was accepted for graduate studies at The Johns Hopkins University Department of Physics and Astronomy. He fulfilled the requirements for a Ph.D candidacy two years later and he received a Masters of Arts in 1989. During the two years, his responsibilities included a teaching assistant position in the general physics lab. From 1989 to 1992 he worked on his Ph.D thesis at the Large Electron Positron collider at CERN working with the $L3$ collaboration. During his stay at CERN, he contributed to the implementation, monitoring and offline analysis of a Plastic Scintillating Fiber system for the calibration of the central tracking detector of the $L3$ experiment. The subject of his thesis is " A Test of QED in Electron-Positron Annihilation at Energies around the Z Mass". Among the many challenges of this analysis was to design a scheme to monitor the performance of the central tracking detector offline, on a minute by minute basis and combinations of different detector data to increase the acceptance and cover 97% of the full solid angle; the best for this type of analysis among the four LEP experiments. The results of this analysis were presented on behalf of the $L3$ collaboration at the 1992 DPF conference at Fermilab. He received his Ph.D in November 1992.